Origami as a platform for tuning drag force

Rishabh Nain

INSTITUT POLYTECHNIQUE DE PARIS

NNT : 2024IPPAX081

Thèse de doctorat

Origami as a platform for tuning drag force

Thèse de doctorat de l'Institut Polytechnique de Paris
préparée à l'École polytechnique

École doctorale n°626 École doctorale de l'Institut Polytechnique de Paris (EDIPP)
Spécialité de doctorat : Mécanique des fluides et des solides, acoustique

Thèse présentée et soutenue à Palaiseau, le 8 November 2024, par

RISHABH NAIN

Composition du Jury :

Olivier Doaré Professeur, ENSTA Paris (Unit of Mechanical Engineering)	Président
Francisco Huera-Huarte Professeur, Universitat Rovira i Virgili (Fluid-sturucture interactions lab)	Rapporteur
Frédéric Léchenault Chargé de recherche, ENS Paris (Laboratoire de Physique)	Rapporteur
Martin Brandenbourger Chargé de recherche, Aix Marseille University (IRPHÉ)	Examinateur
Benoît Roman Directeur de recherche, PMMH-ESPCI Paris	Examinateur
Sophie Ramananarivo Assistant professor, École polytechnique (LadHyX)	Directeur de thèse
Arthur Lebée Maître de conférences , École des Ponts ParisTech (Navier laboratory)	Invité

Résumé

La force de traînée augmente généralement avec la vitesse d'écoulement, sauf dans certains cas tels que les crises de traînée ou les changements de forme brusques, comme l'élagage des arbres par le vent. Bien que l'élagage réduise efficacement la traînée tout en préservant l'intégrité structurelle, il est irréversible. Une alternative aux changements de forme abrupts réside dans les événements de snap-through dans des structures flexibles. L'origami offre un cadre prometteur pour concevoir de telles structures capables de changer de forme, permettant de définir des trajectoires cinématiques et des propriétés mécaniques spécifiques, en particulier la bistabilité.

Cette thèse explore comment les techniques d'origami peuvent être utilisées pour moduler les forces de traînée, en s'appuyant sur des unités bistables capables de passer à un second état stable soit par une trajectoire cinématique, soit par un degré de liberté caché lié à la flexion des facettes. Ces unités peuvent soit se déformer de manière continue dans l'écoulement avec un événement de snap-through , soit conserver des formes distinctes avant et après cet événement. Les deux comportements entraînent une évolution discontinue de la traînée en fonction de la vitesse d'écoulement. En ajustant les propriétés géométriques et mécaniques, il est possible de moduler le comportement de transition et les forces de traînée. Des expériences, appuyées par des modèles aérodynamiques théoriques équilibrant les forces fluides et élastiques, ont permis de concevoir des structures passives efficaces pour contrôler la traînée dans des environnements fluides. Un exemple est une vanne passive utilisant l'origami pour réguler le flux.

Deux unités d'origami sont étudiées : la base Waterbomb et la structure Miura ori. Ces systèmes bistables interagissent de manière unique avec les forces fluides pour offrir des caractéristiques de traînée modulables, comme des réductions brusques ou un contrôle ajustable de l'écoulement. Des tests en soufflerie et des modélisations théoriques ont permis d'analyser des paramètres tels que le rayon des cellules, la rigidité des plis et la géométrie des facettes, facilitant la rétro-ingénierie de structures visant des objectifs aérodynamiques spécifiques.

La bistabilité et les transitions de snap-through de l'unité Waterbomb sont au cœur de son fonctionnement Sous l'effet de l'écoulement d'air, cette unité se déploie, s'aplatit, puis passe brusquement à une configuration profilée, entraînant une chute soudaine de la traînée. Ce comportement est régi par l'équilibre entre les forces fluides et élastiques, décrit par le nombre de Cauchy. En modifiant des propriétés telles que la rigidité, le rayon des cellules et l'angle de repos, les conditions critiques de snap-through et la réduction de la traînée ont pu être contrôlées. La combinaison de plusieurs unités a permis d'obtenir des sauts successifs de traînée, démontrant le potentiel d'une conception modulaire. Dans une configuration confinée, l'unité Waterbomb a agi comme une vanne régulant l'écoulement. La chute de pression non linéaire reflète le comportement de traînée observée en écoulement libre, avec des effets supplémentaires du confinement. La combinaison d'unités en série ou en parallèle a permis un contrôle complexe de l'écoulement, avec des applications potentielles comme des soupapes de décharge de pression ou des limiteurs de débit. Cette polyvalence souligne son intérêt pour des systèmes de contrôle fluidique.

L'unité Miura ori, quant à elle, présente une trajectoire bistable différente, exploitant la

flexion des facettes comme degré de liberté caché. Contrairement à la déformation continue de l'unité Waterbomb, elle passe directement entre deux états rigides sous l'effet du chargement fluide, entraînant une discontinuité abrupte de la traînée qui sépare deux régimes avec des coefficients de traînée constants. Des paramètres tels que l'angle du sommet, la longueur des facettes et l'angle de montage permettent de contrôler sa rigidité et sa réponse aérodynamique. Les expériences ont montré comment les variations géométriques influencent la traînée, la combinaison de plusieurs unités a permis d'obtenir des comportements aérodynamiques modulaires.

Cette thèse met en avant l'origami comme une plateforme innovante pour façonner les interactions fluide-structure. En exploitant la bistabilité, les unités d'origami produisent des comportements traînée-vitesse non linéaires avec des transitions abruptes. Les applications envisagées vont de l'atténuation des charges aérodynamiques à la détection de seuils de vitesse ou à la régulation du débit. La combinaison de plusieurs unités permet de programmer les réponses de traînée, ouvrant de nouvelles perspectives pour des systèmes adaptatifs complexes. Les structures déformables en origami représentent un changement de paradigme dans la conception aérodynamique, offrant des solutions autorégulées sans capteurs ou actionneurs externes, et ouvrent de nouvelles possibilités pour le contrôle passif dans les environnements fluides.

Summary

The drag force typically rises with flow speed, except in cases like drag crises or abrupt shape changes, such as wind-induced tree pruning. While pruning effectively reduces drag and preserves structural integrity, it is irreversible. An alternative for abrupt shape changes is snap-through events in flexible structures. Origami offers a promising framework for crafting such shape-morphing structures, enabling desired kinematic pathways and mechanical properties, especially bistability.

This thesis investigates how origami techniques can tune drag forces, using bistable units capable of transitioning to a second stable state through either a kinematic path or a hidden degree of freedom arising from facet bending. These units either deform continuously in flow with a snap-through event or retain distinct pre- and post-snapping shapes, both showing discontinuous drag changes with flow speed. Adjusting geometric and mechanical properties allows fine-tuning of snapping behavior and drag forces. Experiments, supported by theoretical aeroelastic models balancing fluid and elastic forces, enabled the development of efficient passive drag-control structures, such as an origami-inspired valve for flow regulation.

Two origami units are studied: the Waterbomb base and the Miura ori structure. These bistable systems interact uniquely with fluid forces, offering tunable drag features like sharp reductions or adjustable flow control. Wind tunnel tests and theoretical modeling analyzed parameters such as cell radius, fold stiffness, and facet geometry, enabling reverse-engineered designs for specific aerodynamic goals.

The Waterbomb unit's bistability and snap-through transition is key to its function. In airflow, it unfolds, flattens, and snaps into a streamlined shape, triggering a sudden drag drop. This behavior is governed by fluid-elastic force balance, captured using the Cauchy number. Properties like stiffness, cell radius, and rest angle were tuned to control critical snapping conditions and drag reduction. Combining units produced multiple drag transitions, demonstrating modular design potential. In a confined setup, the Waterbomb acted as a flow-regulating valve. The non-linear pressure drops reflected the drag behavior observed in open flow, with additional effects from confinement. Arranging units in series or parallel configurations enabled complex flow regulation, such as functioning as pressure relief valves or flow limiters. This versatility highlights the potential for advanced fluidic control systems.

The Miura ori unit offers a different bistable pathway, using facet bending as a hidden degree of freedom. Unlike the Waterbomb unit's continuous deformation, it transitions directly between two rigid states under fluid loading, leading to an abrupt drag discontinuity that separates two regimes with constant drag coefficients. Parameters like vertex angle, facet length, and mounting angle controlled its stiffness and aerodynamic response. Experiments showed how geometric variations influence drag, and combining units enabled modular aerodynamic behaviors.

This thesis highlights origami as a platform for shaping fluid-structure interactions. By leveraging bistability, origami units achieve non-linear drag-speed behaviors and sharp transitions.

Applications include reducing aerodynamic loads, detecting velocity thresholds, and limiting flow rates. Combining multiple units enables programmable drag responses, advancing adaptive system design. Origami morphing structures represent a paradigm shift in aerodynamic design, offering self-regulating solutions without external sensors or actuators, and new possibilities for passive control in fluid environments.

Acknowledgement

Completing this thesis has been a challenging and transformative journey, and it would not have been possible without the support, guidance, and encouragement of many incredible individuals. I am deeply grateful to all those who have contributed to this work in various ways, making this milestone a reality.

First and foremost, I extend my heartfelt gratitude to my advisor, Dr. Sophie Ramananarivo, for their unwavering support, insightful feedback, and patience throughout this process. Your expertise, encouragement, and belief in my abilities have been instrumental in shaping this thesis. I am particularly grateful for your ability to ask the right questions and guide me toward critical insights, which greatly enriched my research. I am also indebted to the members of my thesis committee, Prof. Olivier Doaré, Prof. Francisco Huera-Huarte, Dr Frédéric Léchenault, Dr Martin Brandenbourger, Dr Benoît Roman and Dr Arthur Lebée, whose thoughtful critiques and valuable suggestions helped refine my work. Your dedication to academic excellence has been a source of inspiration.

Special thanks go to my peers and colleagues in the LadHyX, whose camaraderie and collaboration have made this journey not only intellectually stimulating but also enjoyable. The countless discussions, brainstorming sessions, and shared challenges have significantly contributed to my growth as a scholar.

To my friends outside academia, thank you for reminding me of life beyond the confines of my research. Your humour, empathy, and encouragement have been my anchors during moments of self-doubt and fatigue. I owe an immense debt of gratitude to my family for their unconditional love, sacrifices, and unwavering belief in me. To my parents, Mr. Manoj Kumar and Ms. Babita Nain, thank you for instilling in me the values of hard work and perseverance. Your constant encouragement has been my foundation. To my siblings, Ansuiya Nain and Shubham Nain, thank you for being my cheerleaders and a source of inspiration.

I wish to express my heartfelt gratitude for the financial and institutional support provided by IP Paris and the Chair "Innovative Process and Materials" Saint-Gobain, which funded my Master's program. This support made it possible for me to pursue a PhD in France, without which this research would not have been feasible. The resources and opportunities provided have been invaluable to the successful completion of this work. Finally, I extend my deepest appreciation to the countless individuals, authors, and scholars whose work has inspired and informed this thesis. While it is not possible to mention each one by name, please know that your contributions have profoundly shaped and enriched this research.

Completing this thesis has been both a humbling and rewarding experience, and I am deeply grateful to everyone who has played a part in this journey. This achievement is as much yours as it is mine.

Thank you all.

Origami as a platform for tuning drag force

Rishabh Nain

Contents

List of Figures

Chapter 1

Introduction

Contents

1.1 Why do we need to tune the drag?

When an object moves through a fluid, it encounters a drag force. The drag force opposes the motion of the object and depends on its shape, its size, its velocity and the surrounding fluid. Let us look at the different scenarios that exist in real life where drag forces and their control are necessary.

1.1.1 Drag as a foe: Applications that benefit from drag reduction

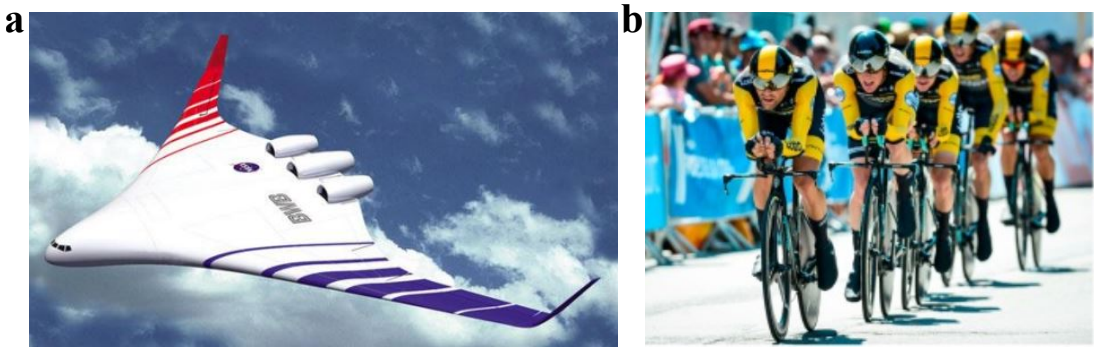

Figure 1.1: Applications of drag reduction in aerospace engineering and sports. (**a**) Blended wing-body aircraft[1]. (**b**) Drafting by cyclists[2].

Drag reduction is a crucial aspect in several fields where minimizing resistance due to fluid flow can lead to significant improvements in performance, fuel efficiency, and cost savings. Some of the typical scenarios are from aerospace and automotive engineering. An active field of research is the aircraft design to make streamlined shapes, and smooth surfaces and the use of advanced materials to reduce the pressure drag as well as the friction drag experienced by the vehicle during the flight (Fig.1.1a)[1, 3]. Minimizing drag during re-entry or in low-earth orbit for spacecraft and satellites helps conserve fuel and maintain stability[4]. Apart from the aviation industry, the motor industry also benefits from drag reduction. Reducing drag on conventional and sports cars makes them fuel efficient as well as faster[5]. This is achieved by adding devices like spoilers, wings, or diffusers to make them aerodynamically more streamlined and control the downward force on them. Ships and submarines also benefit from hull shaping, special coatings and air lubrication systems to reduce the drag on hull and propellers and noise while maintaining speed[6, 7].

Another field where drag reduction is important is sports. Much research goes into making streamlined helmets, suits, and bike designs to reduce air resistance for cyclists to improve their speed and endurance. For the team events cyclists shelter themselves in the wake of their teammates to reduce their own drag. This technique called drafting (Fig.1.1b) is the most used strategy to save energy [2, 8]. Similarly, drag-reduction strategies are employed in other sports such as swimming and sailing. Studies of the impact of aerodynamic forces in sports equipment like balls, shuttles and javelins also provide a competitive edge to athletes [9, 10].
Even though it may seem like drag forces are always bad and we need to reduce them, let us see some devices which benefit from increased drag forces.

1.1.2 Drag as a friend: Applications that benefit from an increase in drag

While many applications focus on reducing drag to improve efficiency and performance, there are scenarios where increasing drag is beneficial. For instance, parachutes, commonly used in skydiving, space capsules, and emergency aircraft deceleration, rely on the increased drag to slow

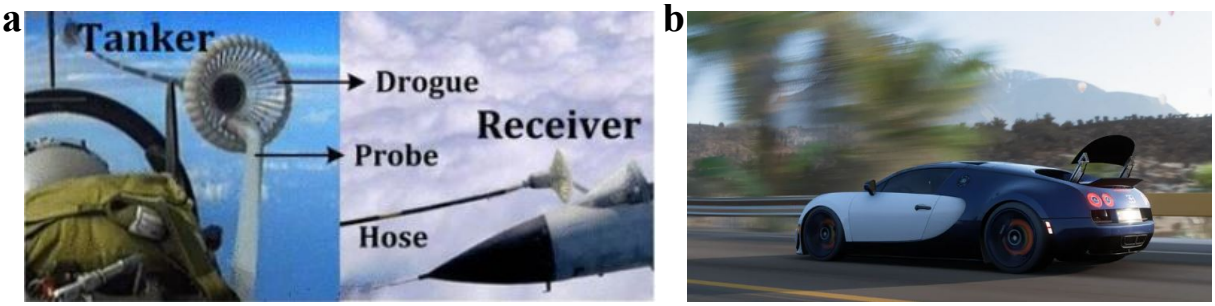

Figure 1.2: Applications of increase in drag in aerospace engineering and sports. (**a**) Air drogue used for aerial refuelling[11]. (**b**) Air brakes on the sports car.

descent and ensure safe landings[12, 13]. Apart from deformable membranes like parachutes, rigid plates or structures can also be used to increase drag for example High-performance racing cars use air brakes that deploy panels to create additional drag (Fig.1.2b), enhancing deceleration[14]. Similarly, Aircraft employ spoilers during landing to increase drag and reduce lift, aiding in slowing down the aircraft[15]. Another possibility is to use a rigid structure covered with a membrane having a high normal area as in the case of Fighter jets and space shuttles which use drag chutes and drogues for rapid deceleration upon landing and to provide stability during aerial refuelling (Fig.1.2a)[11, 16]. Some other instances include re-entry vehicles like satellites or missiles utilizing drag to slow and stabilize their descent [17]. Drogues are used in free-floating boats for control and stability in complex environments [18].

In each of these applications, increasing drag is a controlled and deliberate strategy to achieve specific outcomes, such as deceleration and stability. This overview demonstrates the various strategies employed to manage drag forces effectively. Let us look at the various strategies that have been employed to control the drag forces.

1.1.3 Drag tuning strategies

Drag force can be either beneficial or detrimental to the same system, depending on its operating conditions. For example, aircraft require reduced drag for fuel efficiency but increased drag for safe landing deceleration. Similarly, sports cars are streamlined to reduce drag but use air brakes for safety. This dual requirement highlights the necessity for systems that can dynamically manage drag forces. Aerodynamic systems that can change shape are essential for efficiency and manoeuvrability at different speeds. These shape-changing systems are broadly categorized into active and passive components. Active components, require external actuators such as motors, electric fields, and pneumatic devices to function. Passive components, on the other hand, utilize inherent pressure forces and flow speed as actuators, offering a more self-sufficient approach.

Most existing drag control strategies are active. For instance, cars employ adaptive spoilers and diffusers (Fig.1.3a) that adjust based on speed and driving conditions, significantly enhancing performance and safety[19]. Similarly, advanced aircraft wings constructed from carbon fibre composites can morph and twist using actuators (Fig.1.3b), allowing for optimal aerodynamic performance under various flight conditions [20]. Another innovative active strategy is the implementation of adaptive surface roughness and texture, which can modify drag characteristics dynamically[21, 22]. Despite their effectiveness, active systems have the drawback of relying on external actuators, which adds complexity and potential failure points. This limitation is addressed by passive systems, which operate without external energy input. A common passive strategy involves incorporating flexibility into the structure. For example, MIT in collaboration with NASA recently demonstrated a wing made from mechanical metamaterials that automatically responds to changes in aerodynamic loading by shifting its shape (Fig.1.3c) through a self-adjusting, passive reconfiguration process[23]. This technology mimics the adaptive capa-

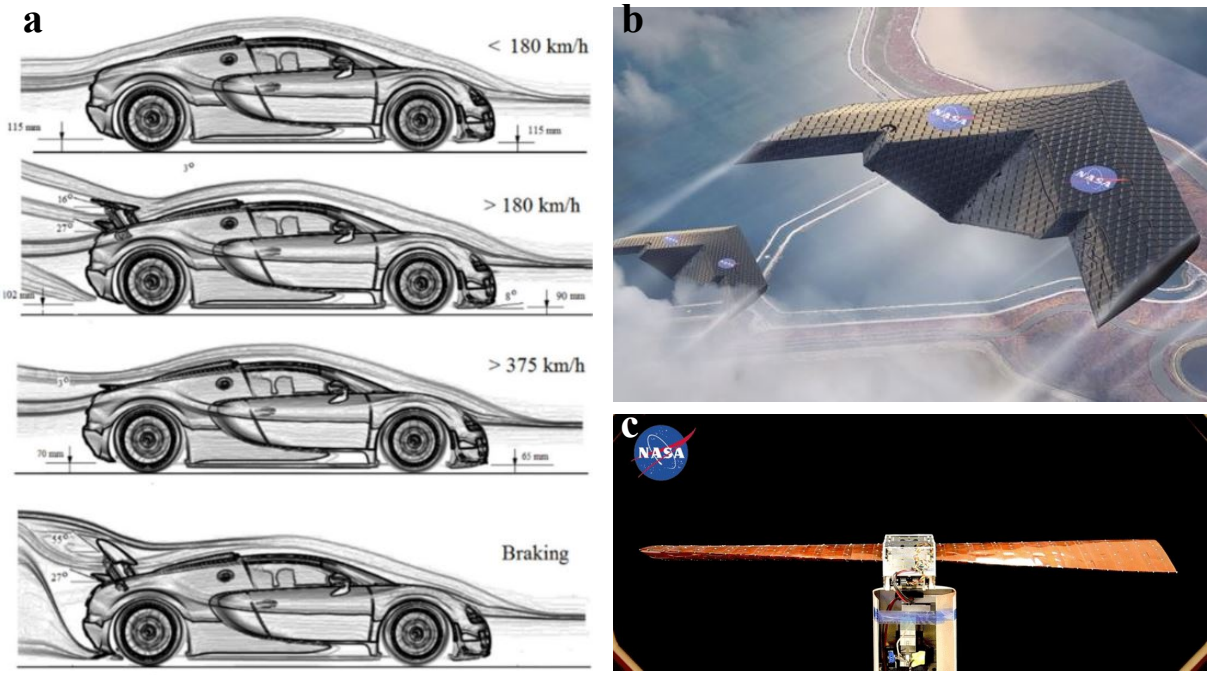

Figure 1.3: Drag control strategies employed for different applications. (**a**) Bugatti Veyron operation modes [19]. NASA/MIT (**b**) morphing wing and (**c**) deformable wing undergoing its twisting motions. Adapted from the NASA website.

bilities observed in nature, such as the way birds adjust their wing shapes during flight.

The ability to morph, or change shape, is highly desirable for several reasons, both in nature and engineering. It allows organisms and machines to respond to varying external conditions, improve interactions with other bodies, and manoeuvre effectively in different media such as water or air. This adaptability enhances performance, safety, and efficiency across a wide range of applications. In the following section, we will look into passive strategies employed by flexible structures to change shape in response to different flow conditions, highlighting their potential and advantages in various aerodynamic contexts.

1.2 Passive drag control strategy through flexibility and reconfiguration

Flexible systems can bend without breaking under external forces, including those exerted by surrounding fluids. However, industries have traditionally preferred rigid components over flexible ones, especially in areas like aeronautics, turbines, and civil engineering. In these sectors, flexible systems are often deemed unsuitable because they tend to deform and their susceptibility to instabilities and vibrations caused by fluid flow. Nonetheless, the advantages of flexibility are well-documented in both the plant and animal kingdoms.

1.2.1 Plant life: Flexibility as defense mechanism

Flexibility is crucial for species adaptation to their environment. For example, a tree must endure harsh conditions such as strong winds and storms. A rigid structure would make survival difficult. To withstand these extremes, trees have developed a passive strategy that leverages the flexibility of their leaves and sometimes branches. When exposed to wind, the leaves bend and adjust their shape to the surrounding fluid flow. This reduces the force experienced by the trees and prevents uprooting. These deformations are somewhat reversible, allowing the

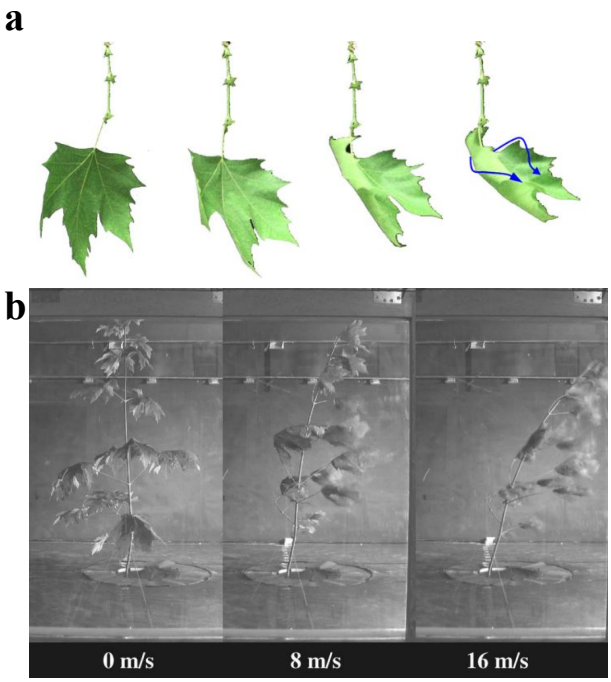

Figure 1.4: (**a**) A tree leaf bends in the wind and adapts its shape to the flow velocity[24] (**b**) Photographs of bigleaf maple tree at increasing flow speed[25].

leaves to return to a flat surface in calm conditions to capture sunlight effectively. One of the first studies to understand and characterize the shape change and consequently change in drag force was conducted by S. Vogel, who initiated a set of experimental measurements on a single leaf or a cluster of leaves attached to a branch (Fig.1.4a) [26–28]. The study compared these measurements to those of a rigid system, which experiences a quadratic drag law $F_d \sim U^2$, and found that the deformation of the plant (Fig.1.4b) is accompanied by a process of drag reduction. This phenomenon is captured through a scalar V, called the Vogel exponent, which expresses the drag evolution with a weaker power law: $F_d \sim U^{2+V}$. Numerous studies have followed, classifying plant species according to their flexibility and drag reduction capabilities [24, 25, 29]. The process by which flexible structures change their shape and adapt to external fluid loading is called reconfiguration. This strategy is particularly interesting to exploit because it is passive and governed by structural properties. Let us look at the reconfiguration of model systems.

1.2.2 Model system: First step towards understanding reconfiguration

Natural systems, like the veins in leaves or the wings of insects, exhibit complex shapes with localized stiffness. To better understand how these deformable surfaces interact with fluid flow, researchers have conducted investigations using simpler model systems with controlled geometries and stiffnesses.

Alben et al.[33, 34] studied a flexible filament in a soap film flow, using a two-dimensional fluid-elastic model to describe their experiments. They established a relationship between the shapes and drag evolution, and identified a scaling of drag with flow velocity in this two-dimensional setup. Following this, Schouveiler et al.[31]and Gosselin et al.[30] examined thin disks cut along one radius or multiple radii, respectively. As shown in Fig.1.5a and b, deformation becomes more pronounced with increasing flow speed. Their studies demonstrated that the flow-induced deformation and the resulting drag reduction are determined by a balance between structural stiffness and fluid forces.

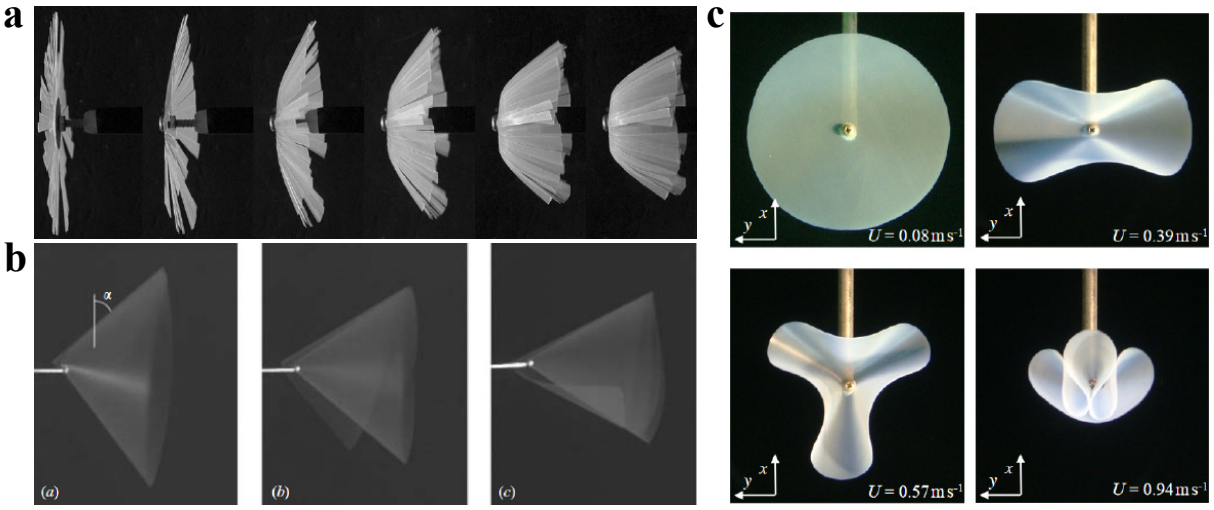

Figure 1.5: Flow-induced deformation modes of a disk with different initial conditions. (**a**) a disk cut along several radii equally spaced[30], (**b**) a disk with a single cut along the radii[31] and (**c**) disk with no cuts[32].

These investigations revealed that geometry plays a critical role. The disks with multiple cuts bend like cantilevered beams (Fig.1.5a), while a disk with a single radial cut rolls into a cone shape (Fig.1.5b). In contrast, an uncut disk deforms into draped shapes that develop more lobes as the flow speed increases (Fig.1.5c). The transition between shapes corresponds to changes in the system's energy configuration, which includes both fluid and elastic contributions[32].

These examples illustrate the variety of shapes and drag behaviours that can be achieved through simple geometrical modifications. We will now explore the elastic and fluid forces acting on the model system and discuss how to characterize these interactions.

Fluid loading on slender structures

The behaviour of fluid flow around an object can be described using the Reynolds number, $Re = UR/\mu$, where U is the flow velocity, R is a characteristic length, and μ is the kinematic viscosity. In the experiments mentioned earlier (as well as in our own experiments), Re can reach values as high as 10^5. This indicates that we are in an inertial regime where viscous forces can be neglected, except in the turbulent wake formed downstream of the object. In such a regime, the flow exerts normal dynamic pressure forces on the object, which can be divided into a drag component (in the direction of the flow) and a lift component (perpendicular to the flow).

For a solid object with a fixed shape, the drag force is given by $F_d = 1/2 C_d S \rho U^2$, where S is the reference area (often the projected frontal area), C_d is a dimensionless drag coefficient dependent on the object's shape, and ρ is the fluid density. The solid line in Fig.1.6a, representing the drag force on a rigid plate, shows a quadratic relationship with velocity, following U^2 behaviour.

This quadratic relationship between drag and velocity is well-established for rigid, bluff bodies. However, the scenario becomes more complex for flexible systems. As observed in plants, fluid loading can cause shape changes that reduce the frontal area S exposed to the flow, allowing the object to align more with the flow direction, thereby adopting a more streamlined shape with a lower drag coefficient C_d. For flexible systems that are porous or in confined flows, shape-dependent blockage can also alter the effective flow speed around the object.

Figure1.4a illustrates the change in the shape of the leaf which leads to drag reduction, while the inset in Fig.1.6b shows a similar effect for a flexible plate[30]. As the flow velocity increases, the flexible plate bends, significantly reducing its frontal area and resulting in a more

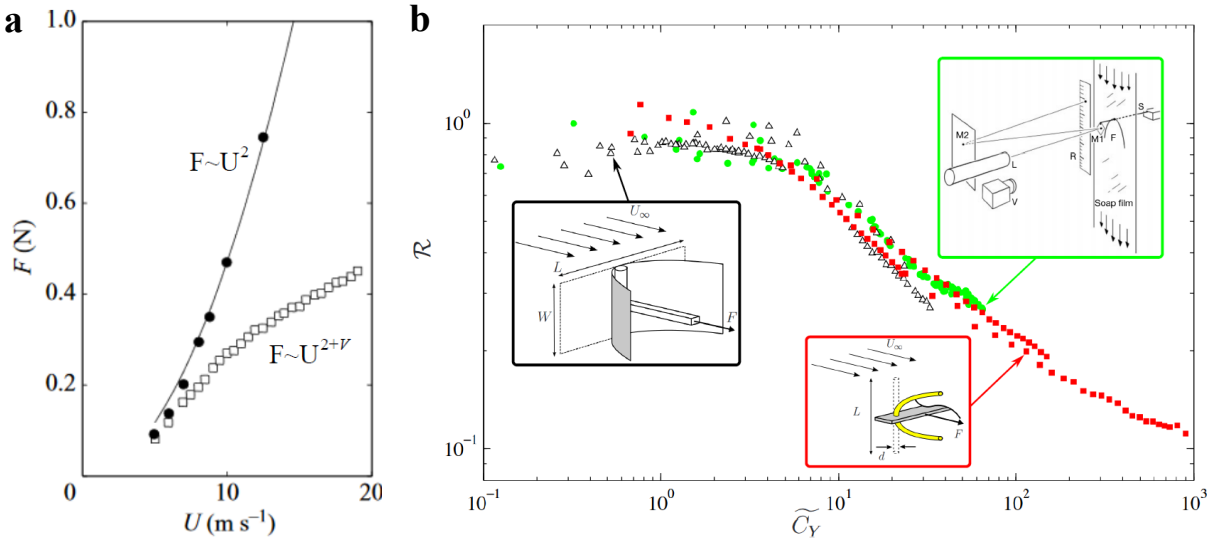

Figure 1.6: (**a**) Evolution of the drag force with U for such a flexible plate (hollow markers), compared to the drag on a rigid plate (black line) [30]. (**b**) Reconfiguration number R for three different slender flexible systems: rectangular plates of varying size and stiffness, flexible filament (both from [35]); short fibres tested in soap film flow by Alben et al.[33]. All are replotted as a function of the Cauchy number.

streamlined shape. The impact of this shape change on drag is depicted in Fig.1.6a. At low speeds, the flexible plate (represented by hollow squares) experiences similar drag to a rigid plate (represented by solid circles). However, as the fluid load increases, the reconfiguration of the flexible plate's shape leads to a significant reduction in drag compared to the rigid case. The drag force no longer follows a quadratic relationship with velocity but instead follows a power law with a lower exponent, characterized by the Vogel coefficient $V \approx -2/3$[26].

The specific power law relationship depends on the shape reconfiguration: different shapes, such as a cone-rolling up or a bending filament, will reduce drag in distinct ways, resulting in different Vogel exponents for each reconfiguration technique. Let us try to understand the reconfiguration process through the lens of another non-dimensional number which balances the fluid force and the elastic forces in the system.

Cauchy number

To balance the competition between elasticity and fluid forces, we introduce the dimensionless Cauchy number, C_y, which represents the ratio of typical fluid loading on the structure to the elastic restoring forces. For the thin strip mentioned earlier, it is defined as:

$$C_y = \frac{\text{fluid loading}}{\text{elastic restoring force}} = \frac{\rho U^2 W L^2}{EI} \tag{1.1}$$

Where ρ is the density of the fluid, U is the flow velocity, W and L are the width and length of the strip respectively and $B = EI$ is the bending stiffness of the sheet. By plotting drag measurements for deformable objects such as plates, filaments, and fibres with varying stiffness against C_y (instead of U), we can improve our understanding of these fluid elastic interactions.

Additionally, Gosselin et al.[30, 33, 35] introduced the reconfiguration number $R = F_d/F_{d,r}$, which compares the drag of flexible objects F_d to that of a rigid object with the same geometry ($F_{d,r}$). We will use this dimensionless quantity to characterize the impact of deformability on drag. As shown in Fig.1.6b, the data collapses onto a single curve, indicating that deformation is indeed governed by the interplay between elasticity and fluid forces, as captured by the Cauchy

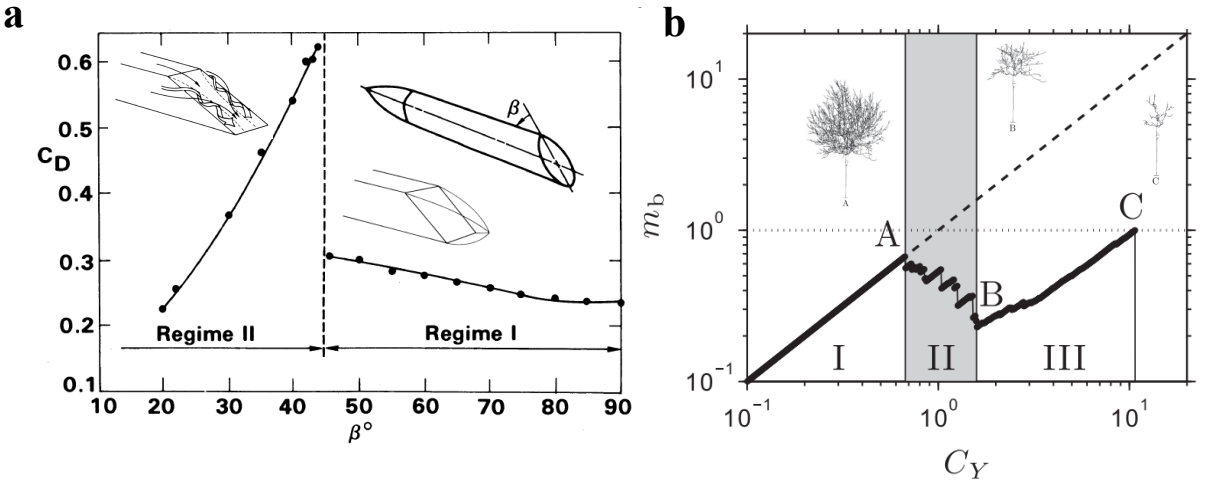

Figure 1.7: (**a**) Sharp change in drag coefficient for bluff body shape similar to hatch-back cars, on increasing the slant angle the flow separation in the near wake regime changes significantly[36]. (**b**) The sequential breakage of a walnut tree branch is illustrated by the progression of the bending moment at the tree's base, denoted as m_b[37].

number. In Fig.1.6b, the reconfiguration number also highlights a transition between two drag regimes. At low C_y, when fluid loading is small relative to structural rigidity, the plate or fibres deform minimally, and their drag forces are similar to those of a rigid object (i.e. $R \sim 1$). At high C_y, the deformable system reconfigures, reducing drag and decreasing R. In the regime of large deformation, R decreases with a constant logarithmic slope, indicating a new drag scaling with flow speed.

For the flexible plate, the response is determined by bending stiffness, as bending is the preferred mode of deformation. However, if another deformation mode is involved, the denominator of the Cauchy number will be adjusted to account for this new type of deformation. All the reconfiguration studies mentioned so far have been conducted in a stationary regime, and our work also focuses on a purely static framework.

In the section, we identified various non-dimensional numbers which are helpful to characterize the reconfiguration process. Apart from reconfiguration, slender structures can also show snap-through instability in external flow which leads to sudden shape change and it has been utilized in various studies which we will discuss in the next two sections.

1.2.3 More than reconfiguration: drag discontinuity

As previously discussed, reconfiguration reduces the load on deformable bodies compared to non-deformable ones. Despite this reduction, drag still increases with speed, although at a slower rate. However, there are instances where drag decreases sharply with increasing velocity. One such phenomenon, known as drag crisis, occurs due to a sudden change in flow regime when the boundary layer transitions from laminar to turbulent, moving its separation point downstream and narrowing the wake [38, 39]. Another example involves bluff body shapes characteristic of hatchback cars, where increasing the slant angle alters the flow pattern in the near wake region. This change causes the separation pattern to shift from quasi-axisymmetric (region 1) to a 3D separation pattern (region 2), leading to a sharp change in the drag coefficient (Fig.1.7a)[36].

A similar scenario occurs with abrupt and significant shape changes in the body, such as partial breakage in wind-induced tree pruning (Fig.1.7b). This process, observed by Lopez et al.[37, 40], effectively reduces the drag force and preserves the integrity of the remaining structure, though it is not reversible.

An attractive alternative to these irreversible changes is the occurrence of snap-through

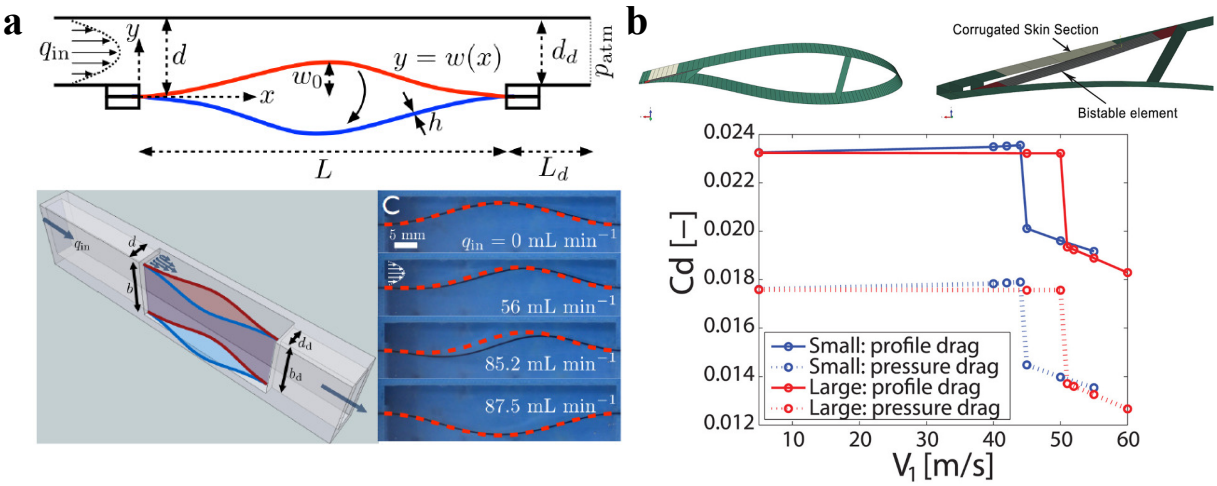

Figure 1.8: (**a**) A thin bent plate placed in an axial flow snaps to its other stable state when the fluid loading increases, resulting in a wider micro-channel section locally[41]. (**b**) Snap through at the Airfoil trailing edge with bistable elements leads to a reduction in drag coefficient[42].

events in flexible structures. The structures with several stable states during the snap-through events rapidly transition from one equilibrium state to another. Let's explore some scenarios where snap-through events can occur.

1.2.4 Snap through events for functionality

The snap-through process in flexible structures is rapid and repeatable, and results in significant shape changes. This characteristic makes it increasingly popular in engineering applications such as switchable optical properties, reusable energy-trapping materials, microfluidic pumps, and soft robotics [43–46]. Snapping instabilities are triggered by external inputs like point loads, electrostatic forces, thermal effects, or fluid flows. For instance, a post-buckled sheet can snap through and snap back in response to varying airflow speeds, allowing for the opening and closing of an air inlet for flow regulation [47, 48]. Similarly, the snapping of a slender membrane or arc has been used to adjust channel resistance for passive control of viscous flow (Fig.1.8a) [41, 49], or to harvest energy from wind-induced snapping oscillations[50, 51].

The critical flow speed required to initiate such instabilities can be tuned using the nonlinear structural mechanics of the post-buckled member. The system's passive response to flow makes it inherently autonomous, eliminating the need for complex actuation. Some studies have focused on the impact of these rapidly changing geometries on aerodynamic loading. For example, in wind turbines, bistable winglets or airfoil trailing edges autonomously transition to another stable state, reducing excessive fluid loads[42, 52] (Fig.1.8b). Although the reported drag reduction is about 15%[42], this is primarily due to a focus on lift applications, suggesting that with appropriate designs, more substantial drag reductions are possible. One of the main focuses of the thesis will be to achieve high drag reduction.

1.2.5 New lever to tune shape and forces in a fluid flow

As discussed before, deformable structures have the advantage of passively adapting their shape to external fluid loads, providing a powerful means of regulating fluid loading. This reconfiguration can notably reduce drag force, preventing damage or rupture in strong winds or currents. Additionally, such deformations can serve functional purposes, such as in flexible valves, enhancing aerodynamic performance with deformable wings, or extracting energy. However, to perform as desired, the structure must deform appropriately, necessitating an understanding of

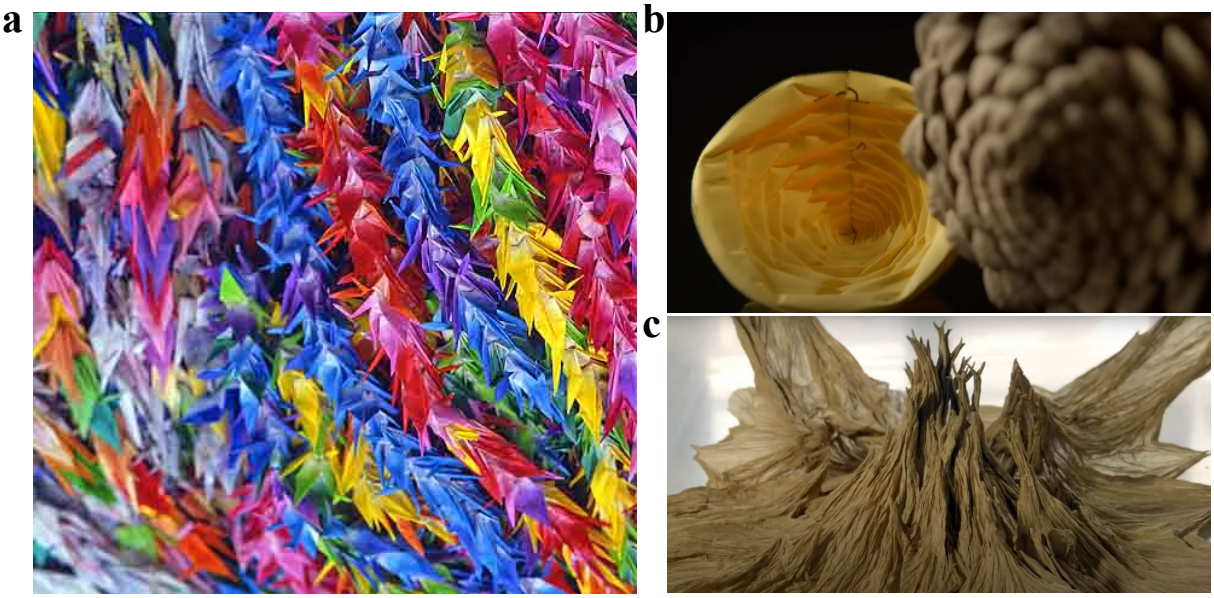

Figure 1.9: (**a**) A thousand cranes popularized by the story of Sadako Sasaki. (**b**) Instant origami obtained by crushing a paper cone with a book shows similarity to the design of pine. (**c**) A new type of artistic origami which uses crumpled paper despite flat sheets. Adapted from documentary: From Paper to Bionics: Origami's Incredible Impact on Science.

the underlying fluid-elastic mechanisms and methods to control them.

Most existing experimental and modelling studies focus on the interaction between fluids and continuously flexible slender structures, like beams or plates, which are particularly prone to deformation. Different behaviours are achieved by altering the stiffness resisting deformation or the object's geometry, such as the differing behaviours of rectangular plates and disks[30, 41].

In this PhD, we explore a new framework for designing components exposed to flows by adding folds to thin surfaces—a technique derived from origami. Initially an art form, origami has emerged as a promising engineering solution for fabricating structures with complex three-dimensional deformation modes and predictable mechanical properties. For us, it represents a new tool to tune deformation and drag forces in fluid flows. The following section presents this technique in detail.

1.3 Origami Structures: A new strategy for controlled shape morphing

1.3.1 A brief history of origami

Origami, the art of paper folding, has a rich history originating primarily from Japan, with significant influences from China and Europe[53]. Paper, invented in China around 105 AD, led to early paper folding traditions like zhe zhi. By the 6^{th} century, Buddhist monks introduced paper to Japan, where origami (from "ori," meaning folding, and "kami," meaning paper) evolved. During Japan's Heian Period (9^{th}-12^{th} centuries), origami was used in religious ceremonies and by the elite. By the 17^{th} century Edo Period, it spread among the general populace with classic models like the crane and frog gaining popularity. The 19^{th} century saw the publication of the first origami instruction book, integrating origami into education. The 20^{th} century brought global recognition, largely due to Akira Yoshizawa, who developed a notation system and popularized modern origami. The story of Sadako Sasaki, a Hiroshima bombing victim who folded 1,000 cranes, symbolized peace and hope worldwide (Fig.1.9a). Advances in the late 20^{th} and

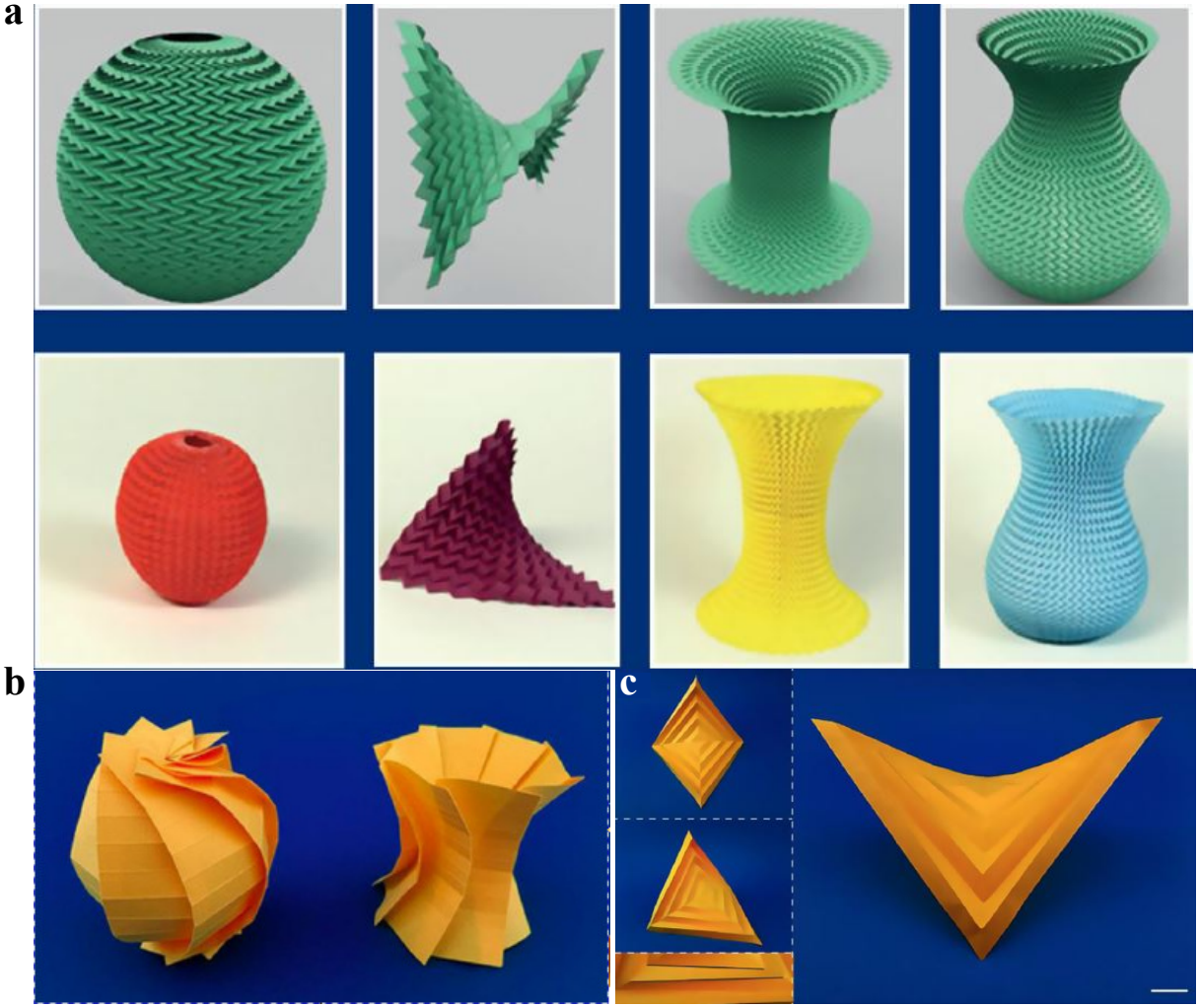

Figure 1.10: (**a**) Generalized Miura-ori tessellations approximating curved surfaces, with the top row presenting simulations and the bottom row featuring physical models[54]. (**b**) An origami sphere (with positive Gaussian curvature) and an origami hyperboloid (with negative Gaussian curvature), are both constructed using curved crease origami techniques as outlined by Mitani[55]. (**c**) Concentric pleating origami used to create Origami hyperbolic paraboloid ("hypar")[56].

21^{st} centuries led to highly complex designs (Fig.1.9b and c) and applications in technology and engineering. Origami continues to be a significant cultural symbol, blending art, mathematics, and science, with key figures like Yoshizawa, Lillian Oppenheimer, and Robert Lang pushing its boundaries. It is also becoming increasingly important in the Engineering and Mechanics field. The presence of these creases on an initially flat surface creates a set of mechanical and morphing properties that will be described in the following sections.

1.3.2 Shape morphing via origami

Three dimensional morphing

Forming intricate 3D structures from a flat sheet of paper requires introducing double curvature, similar to that found in spherical or saddle-shaped geometries. This cannot be achieved through inextensible deformations alone. Instead, the flat sheet must undergo in-plane distortions to form double-curved sections. However, a major drawback of in-plane distortions is that this

method is mainly suitable for soft elastic materials (like gel sheets) and involves intricate shape-shifting programming or external stimuli to reach the desired shapes. Additionally, in-plane distortions can disrupt any surface features printed on the 2D sheets, partially negating one of the main benefits of 2D-to-3D transformations[57].

A better alternative for rigid materials and intricate surface details can be found in origami techniques. These methods enable the creation or approximation of complex shapes through the use of precise fold patterns, to transform flat sheets into 2D or 3D geometries. Several techniques like origami tessellations, curved-crease origami, and concentric pleating are available for this purpose[57]. We will only look at tessellations which we have used during the thesis.

Tessellations simply means putting similar units next to each other. One of the most studied tessellations is Miura-ori. Schenk and Guest[58] demonstrated that a purely rigid Miura-ori has only one degree of freedom, restricting it to in-plane folding and unfolding. However, experiments with simple paper models reveal that folded sheets can also experience out-of-plane deformations. Schenk and Guest[58] identified saddle and twist deformation modes, which are possible in non-rigid Miura-ori structures where individual faces can bend. This characteristic suggests that Miura-ori and similar origami tessellations could be promising candidates for compliant shell mechanisms, as they can alter the global Gaussian curvature of the sheet through unit cell-level deformations [59, 60].

Dudte et al.[54] used constrained optimization algorithms to solve the inverse problem of fitting intrinsically curved surfaces with a generalized Miura-ori tessellation. Their work demonstrated that generalized cylinders can be approximated using tessellations that are both flat-foldable and rigid-foldable, as illustrated in Fig.1.10a. Fig1.10b and c, show different shapes developed via curved creases and concentric pleating techniques.

The three techniques mentioned above are useful to add a desired curvature or to make a desired 3D shape out of a flat 2D sheet of paper. Apart from just morphing a sheet from a 2D geometry to a 3D geometry, these techniques can be useful to morph these 3D geometries from one shape to another, i.e., the structures built using origami techniques allow possible shape change. Let us look at some of these existing shape-change strategies used for different purposes.

Large shape change

Origami structures with large shape changes offer the ability to fold into a small, compact form for easy storage and transportation and then unfold into a larger, functional structure when needed. This is particularly useful in space applications, where components such as solar panels(see Fig.1.11d) and antennas must be compact during launch and expand in space. In the biomedical field, origami principles allow to making of surgical tools which require minimum invasion and devices that can change shape within the body to perform complex tasks[63]. In robotics, these structures provide flexibility, adaptability, and multifunctionality, allowing robots to navigate and operate in diverse environments. Architectural applications benefit from origami-inspired designs through adaptable structures like folding roofs, bridges or walls for ventilation or light control (see Fig.1.11a,b and c). Overall, origami structures combine functionality with compactness and adaptability, offering innovative solutions across various fields. This will be useful to influence the forces in a flow, which is one of the main objectives of the thesis. Let us look into some interesting properties of origami structures which are used in practical applications:

Let us look into the consequence of these folds on the mechanical properties of the material.

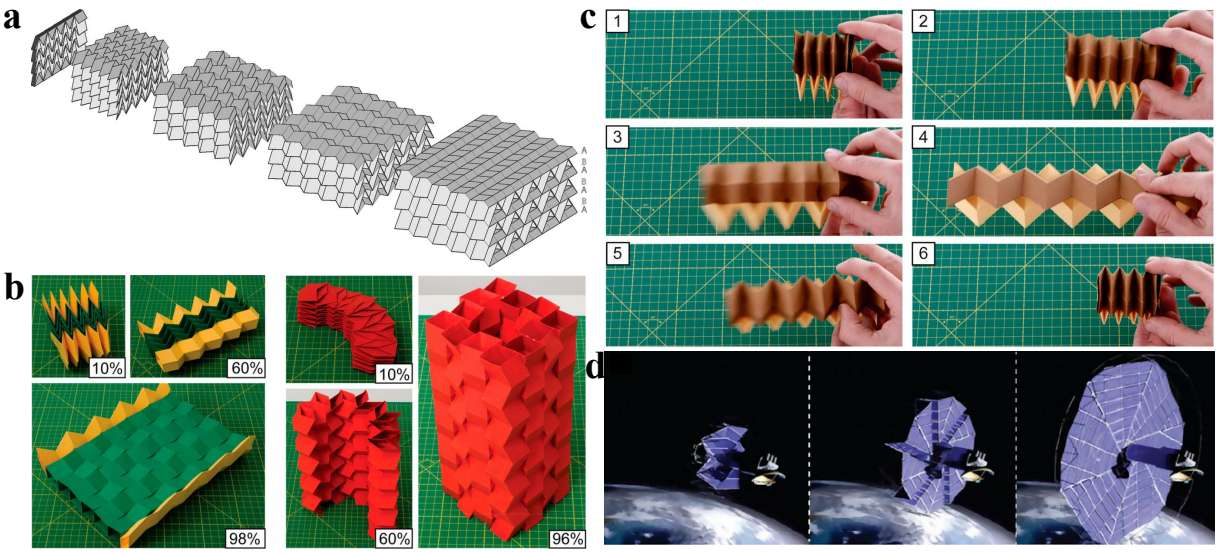

Figure 1.11: Large shape changes in origami structures. (**a**) A folded cellular metamaterial created by stacking individual Miura-ori sheets, which expands and contracts uniformly[58]. (**b**) A deployable paper structure utilizing origami zipper tubes. (**c**) The deployment and retraction sequence of a zipper-coupled tube system[61]. (**d**) An artist's rendering of an origami-based deployable solar array designed for space satellites[62].

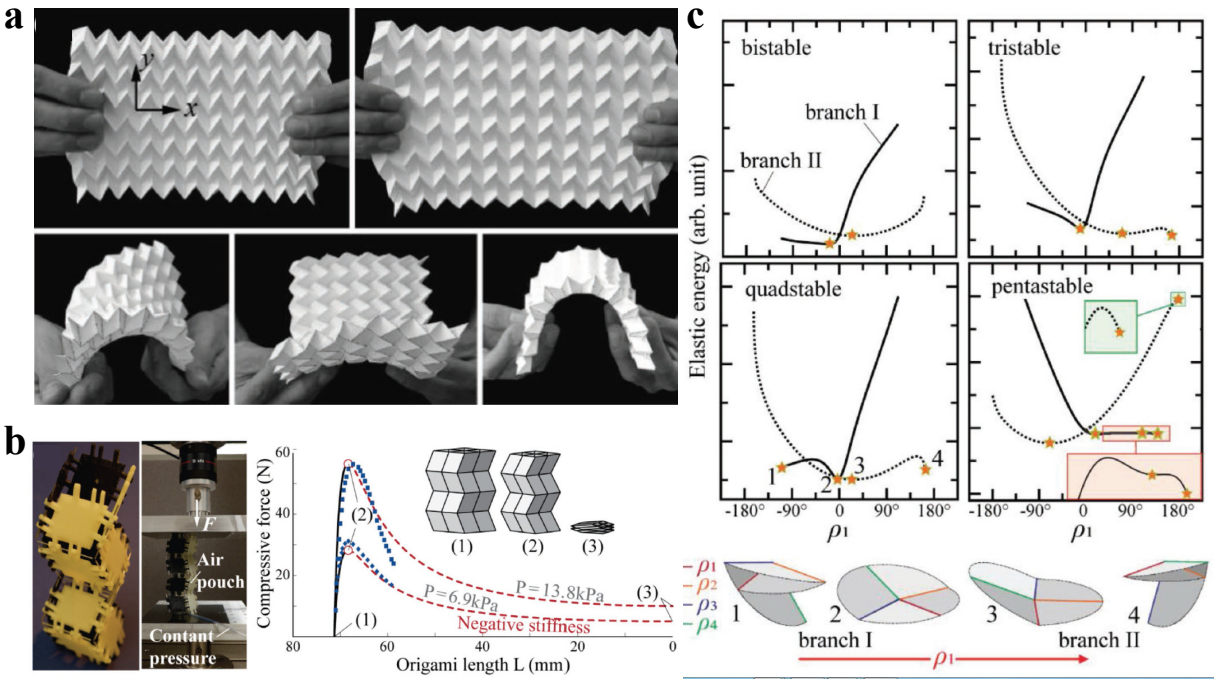

Figure 1.12: (**a**) Auxetic properties of architected origami materials are illustrated by the Miura-ori sheets, which exhibit a unique combination of negative and positive Poisson's ratios in both in-plane and out-of-plane deformations[64]. (**b**) Stacked Miura-ori structures can achieve desirable nonlinear stiffness characteristics, such as recoverable collapse through rigid folding, with the reaction force during collapse adjustable by modulating internal pressure[65]. (**c**) Rigid-foldable, generic degree-4 vertices exhibit multiple stable states, which can be customized by adjusting sector angles, crease torsional stiffness, and rest angles[66].

1.3.3 Folding induced new mechanical properties

Many studies on origami have concentrated on the kinematics of deformation and the geometric relationships imposed by the patterns. However, origami has also garnered interest in the field of mechanics. These structures uniquely derive their mechanical properties from the fold patterns rather than the material of the sheets themselves. Therefore, they are categorized as meta-sheets, a type of mechanical meta-material. Specifically, the focus is on engineering mechanical properties by adjusting the fold patterns. Here, we present examples of unusual mechanical behaviours observed in these structures[64, 67, 68].

Folding introduces fascinating mechanical properties such as auxetic behaviour. For instance, a Miura-ori sheet expands transversely when stretched (see Fig.1.12a), unlike regular materials that tend to contract[64]. Pressurizing stacked Miura-ori tubular channels creates nonlinear relationships between the enclosed volume and external deformation, enabling pressure-induced stiffness control with recoverable and programmable collapse and quasi-zero stiffness properties (Fig.1.12b)[65]. Additionally, origami structures can exhibit discrete stiffness jumps due to the self-locking properties of non-flat foldable designs[69].

Another notable feature of origami is multistability[46, 66, 70, 71], allowing foldable structures to remain stable in both compact and deployed states or even exhibit multiple stable shapes for different purposes. For example, generic degree-4 vertices can have up to five stable states by adjusting the rest angle and crease stiffness (Fig.1.12c). This characteristic is particularly useful in developing new medical stents that need to be compact during surgery and then deployed in place[63]. Multistability also enables rapid and significant shape changes in response to minor external stimuli, such as varying flow velocities, as explored in our work.

1.3.4 Hidden degree of freedom: What if facets are not rigid?

So far, we have discussed origami structures and the unique properties that arise from them. These properties can be accessed through rigid facet origami structures(rigid-foldable) or by incorporating facet bending. An origami design is rigid-foldable if the transition from the flat to the folded state occurs smoothly through bending at the creases only, thus, without bending or stretching of the faces in between the creases. In other words, a rigid origami design could be folded from rigid panels connected with hinges, which is desirable for deployable origami structures made from rigid materials, such as solar panels, medical stents, or robots. Most of the structures that will be discussed in this manuscript will be rigidly foldable. Some structures have their folding kinematics—i.e., the possible shapes they can fold into—significantly influenced by facet bending. One of the earliest examples is the new bending mode of the Miura-ori tessellation (see Fig.1.13a), which emerges when considering facet bending, a mode not possible under the rigid facet assumption[72]. Another example is the square twist origami, which has two topologically disconnected configurations (folded and unfolded states in Fig.1.13b top) and zero degrees of freedom. This means an origami structure made of rigid facets will remain in its initial state, either folded or unfolded, without transitioning between the two. However, introducing facet bending connects these disconnected states and allows the transition[73, 75]. Additionally, changing the plane angle of the unit makes it mono- and bi-stable (Fig.1.13b bottom). Facet bending can also be used to introduce pop-through defects in the Miura-ori tessellation, allowing fine-tuning of the sheet's effective stiffness and the shape of the open and closed unit (Fig.1.13c)[74]. Thus, relaxing the rigid facet assumption in origami structures enables access to previously unreachable kinematic regions, leading to new possibilities. It also offers a way to have stiff structures, that are kind of locked in a stable state, while being able to morph. We have utilized this hidden degree of freedom to go between locked-in states in our work, which will be discussed further in Chapter 3.

In summary, origami methods have shown great promise for mechanics and engineering. The addition of folds overcomes certain limitations of regular sheets, which only deform isometrically

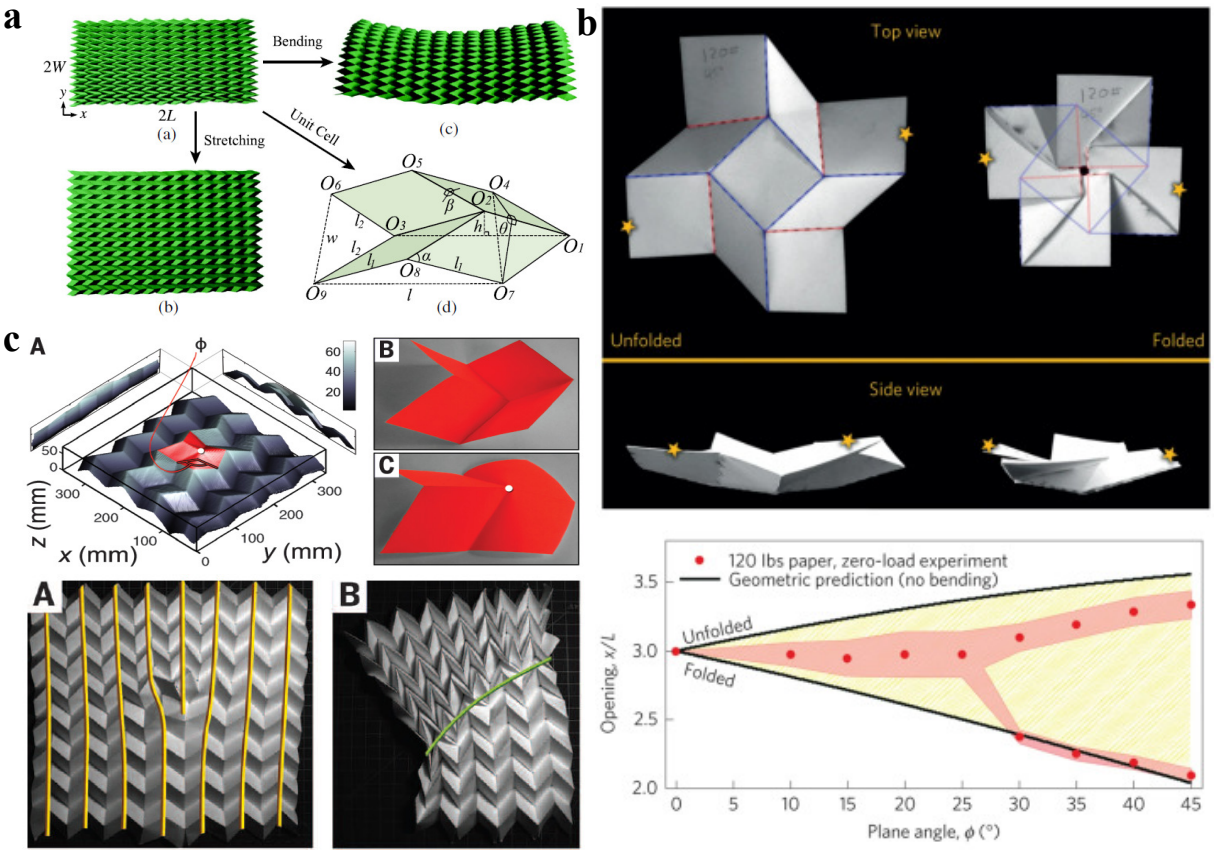

Figure 1.13: (**a**) In-plane stretching and out-of-plane bending modes of the Miura ori tessellation[72] (**b**) Top: Photographs of two topologically disconnected folded shapes of a square twist unit. Bottom: Experimental demonstration revealing the mono and bistable solutions with the plane angle (acute angle of the parallelogram)[73]. (**c**) Pop through defects in a Miura-ori pattern as a result of facet bending. These defects form complex structures and can be useful to program in-plane modulus[74].

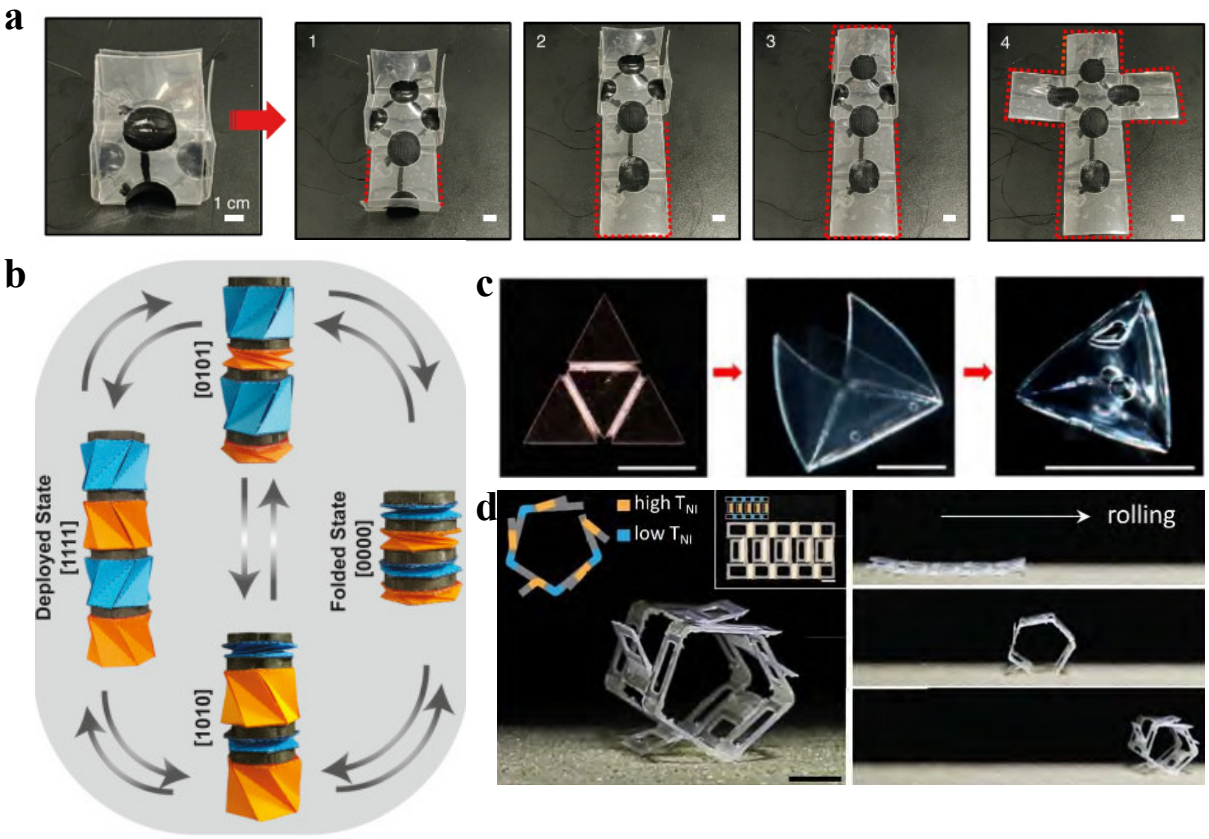

Figure 1.14: (**a**) Programmable unfolding process of the square-shaped soft robot using electric field[76]. (**b**) Sequential magnetic actuation of generalized reverse creases Kresling assemblies with multiple cells[77]. (**c**) Thermally responsive self-folding hydrogel when heated expels water to take pyramidal shape[78]. (**d**) Self-propelled liquid crystal elastomer (LCE) rolling robot beyond its activation temperature[79].

with constant Gaussian curvature, allowing the design of customized kinematics and mechanical behaviours. Notably, mechanical studies have typically investigated the response of origami sheets to only a few types of loading, usually applying in-plane uniaxial traction to characterize stress-strain relationships. Next, let us explore some existing actuation techniques for origami structures.

1.4 Origami mechanical response to stimuli

One of the ongoing challenges in the field of origami structures is to actuate them or make them responsive to changes in their environment (which is a fluid environment for us). To achieve this, it is necessary to be able to program their mechanical response to specific external stimuli. Previous investigations have mainly focused on axial tensile loading to understand the mechanical response of these structures. In the following, we will present other types of loading to which origami has been subjected.

1.4.1 Local actuation

Origami structures can be actuated using various mechanisms tailored to specific applications. The simplest method is manual manipulation, which is folding origami structures by hand, familiar to everyone who has folded origami. Other techniques involve polymers and hydrogels that respond to electricity and heat. Electroactive Polymers (EAPs) can change shape in response

to an electric field, enabling precise control over the creases (Fig.1.14a)[76]. Magnetic actuation, achieved by embedding magnetic materials within the structure, allows remote control via magnetic fields, useful in confined or hazardous environments (Fig.1.14b)[77]. Thermally responsive self-folding hydrogels fold when heated by releasing water (Fig.1.14c)[78]. Liquid crystal elastomers (LCEs) actuate when heated beyond their activation temperature, exemplified by self-propelled LCE robots (Fig.1.14d[79]). Other methods are to use Shape Memory Alloys (SMAs), which return to a pre-defined shape when heated, enabling folding or unfolding with temperature changes. Various smart materials can induce folding using different stimuli, expanding the versatility of origami actuation. These methods are useful for locally actuating creases to achieve a desired shape, though sometimes global actuation is preferred for some instances.

1.4.2 Global actuation

Another way to actuate origami structure is by distributing the load on the facet as opposed to actuating the creases, called global actuation. One of the most commonly used global actuation mechanisms for origami is pneumatic actuation. Pneumatic actuation of origami structures leverages air pressure to induce folding and unfolding, making use of the inherent flexibility and lightweight nature of origami designs. This method works by inflating or deflating air chambers embedded within the structure, causing it to change shape. It is particularly advantageous due to its simplicity, efficiency, and significant movement capability. Applications include soft robotics, where pneumatic actuators enable gentle, adaptable interactions with the environment (Fig.1.15a)[80]; deployable structures in architecture, such as emergency shelters (Fig.1.15b)[70] and space antennas. Pneumatic systems are lightweight and compact, offer a high force-to-weight ratio, and are relatively simple to design and control. However, they do require a constant supply of compressed air, precise control of air pressure, and durable materials to withstand repeated cycles. Despite these challenges, pneumatic actuation provides a versatile and effective means of controlling origami structures, valuable across various fields.

A recent advancement in origami actuation is dynamic actuation. Some mechanisms or structures are kinematically constrained, but dynamic excitation causes the facets' inertia to deform the structure. If deformed sufficiently, some creases may snap through an unstable equilibrium point, changing their fold direction and transforming the overall mechanism. A study on the rectangular Miura ori unit cell, whose base is clamped to a rigid mount has shown various possible dynamic transformations of the unit. A Y strip made up of multiple Miura units combined can attain various possible configurations and the structure can be dynamically actuated to go from one shape to the other as shown in Fig.1.15c and d. This transformation can be actuated with a single electric motor[81] or spring-loaded cell[82] and is faster than the previous actuation techniques. The important point to note is that this method requires low stiffness and the transformation mostly occurs due to the hidden degree of freedom discussed in the previous section.

The above pneumatic actuation mechanism shows the rich range of responses of origami sheets to fluid loading. However, fluid is mainly used as a way to transmit uniform pressure forces, and little use has been made of its motion in these studies so far. In the following, we will discuss a few studies that have subjected origami designs to flows. Note, however, that most of these studies focus exclusively on rigid structures that are fixed in a given configuration and thus have no fluid-elastic coupling.

1.4.3 Origami in flow: Aerogami

Origami structures have been little studied in the field of fluid-structure interaction. J. Zhang et al.[83], measured the drag force and visualize wake patterns for a fixed configuration of a

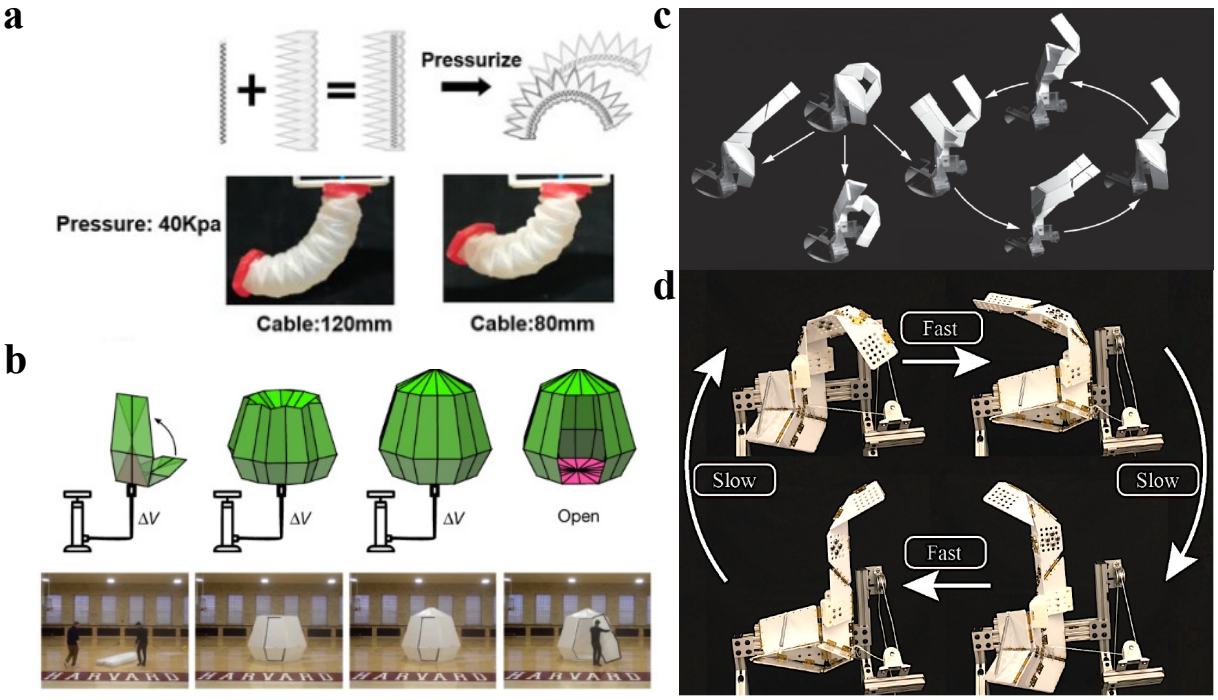

Figure 1.15: (**a**) Soft gripper consisting of origami actuator and fibre. When pneumatically actuated with the same pressure it takes a different shape depending on cable length[80]. (**b**) Pneumatic deployment of meter-scale inflatable shelter (schematic and experimental realization)[70]. (**c**) Dynamic transformation of a branching origami mechanism with five Miura vertices. A sample of the different transformation paths that the mechanism can take[81]. (**d**) Dynamic transformation of origami string with the help of bistable origami cell[82].

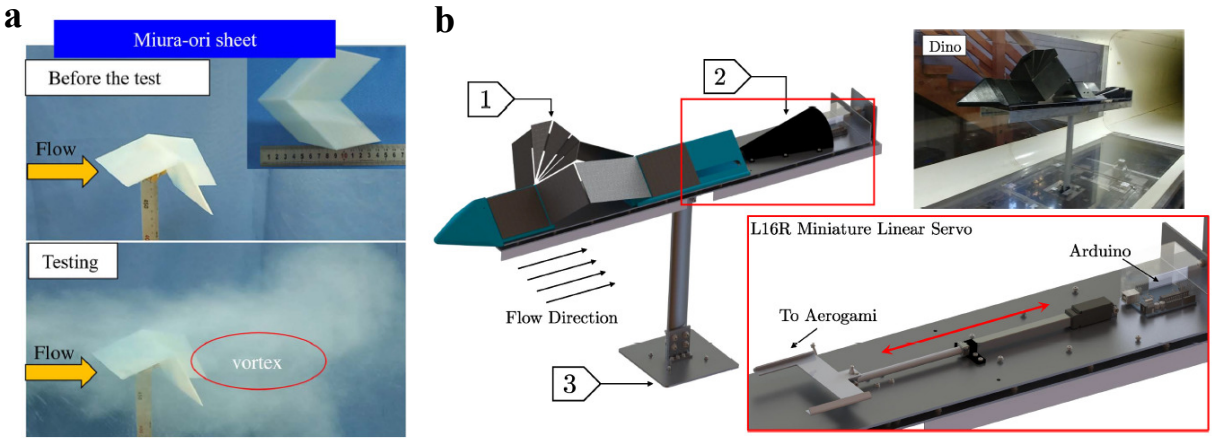

Figure 1.16: (**a**) Flow around a Miura ori cell[83]. (**b**) An origami unit can be deployed/compacted by a linear actuator connected to an Arduino and load sensor[84].

Miura-ori unit (fig1.16a) to determine which configuration generates the least drag. They relate the generation of vortices induced by the folded shape to the decrease of forces. In a more active situation (controlled by an external user), the work of Cozmei et al. investigates the use of two folding patterns as surface controllers[84]. By actively changing the folding state (fig1.16b), they can modify the frontal area exposed to the fluid and, as a result, the drag force. They demonstrate that by adjusting the configuration of creases, they can achieve a targeted force for a given flow. This work suggests that changing the configuration of a folded structure alters its aerodynamic properties and that large shape shifts can lead to significant variations in fluid loads. Another study used the design of an aerodynamic origami-inspired deployable fairing for locomotives. The study depicted a reduction in the overall aerodynamic drag on the locomotive by 16% at a $22m/s$ velocity[85]. Another study uses a magic ball origami pattern-inspired robot that can change its body shape to ingest and expel water, creating a jet that propels it forward similarly to cephalopods[86]. Later a study on the same structure was conducted to measure its drag coefficient with different amounts of expansion[87]. One of the recent studies on the origami structure in the flow is done in our group on the Waterbomb unit. It was shown that the folding of the unit allows for large shape change, and this extreme reconfiguration reduces the drag evolution with speed to the point that it reaches a plateau. The drag value at the plateau can be tuned by mechanical and geometrical properties of the unit[88]. In line with the previous study in this thesis, we are interested in studying deformable origami structures (as opposed to ones with a fixed configuration) that passively adapt their shape to the fluid environment. Given the large shape changes induced by the folding kinematics, we also expect a new evolution of drag with flow speed that will depend on the pattern features.

1.5 Thesis outline

In this thesis, we seek to answer the following question: Can we use origami techniques to tune the drag forces? To this end, we have to understand how folds impact the interaction of slender structures with fluid flow. It departs from the traditional framework of fluid/structure interaction as it involves unusual modes of deformations and mechanical properties. We are going to explore origami as a platform to obtain unusual drag features, specifically tunable drag jump which is the main aim of the thesis. We studied two fundamental origami units for this purpose. We investigated those aspects with an approach combining experiments in wind tunnels and theoretical models. We studied the influence of various geometrical(length, opening angle, number of folds) and mechanical parameters(stiffness) on the drag features and using that knowledge

tried to reverse engineer the structures with complex desired features. This thesis is divided into three main projects that were undertaken during the thesis. The first and second projects were on the study of a Waterbomb unit in an open wind tunnel and under confinement. The third chapter is on the study of the snap-through transition of the Miura ori unit via facet bending. The detailed content of the chapter is as follows:

In the first chapter, we explore the Water Bomb unit, a fundamental origami structure known for its bistable states and quick snap-through transitions. The unit has been used before in our research group for its ability to have extreme shape change. In the chapter, we leverage the unit's bistability for drag applications for the first time. It demonstrates the unit's potential for significant drag reduction through abrupt shape changes, showing a marked drop in drag at a specific flow speed. By systematically varying the unit's geometrical and mechanical properties, the study fine-tunes the drag discontinuity and the critical speed at which it occurs. Experimental results are supported by a theoretical model. The model was then used for inverse design, aiming to determine the origami parameters that achieve the desired drag collapse. A few examples using the inverse design algorithm are shown as a proof of concept demonstrating the possibility of merging multiple units to have multiple drag jumps.

The second chapter focuses on examining the application of Waterbomb unit as a valve, in a confined configuration. A wind tunnel with a circular cross-section larger than the Origami unit was designed for the study. The pressure drop across the confined unit was measured with increasing flow rate, the graph being similar to the drag force depicts that the unit has nonlinear resistance. The study investigates the impact of the unit's radius and stiffness. The same parameters show a slightly different effect compared to the previous chapter because of the confinement that creates a blockage effect. The model from the first chapter is adjusted to account for blockage effects and to compute the pressure loss across the origami unit. Additionally, we examined the combination of valves in series, through both experiments and models based on the unit's resistance to flow, which shows that the two units can be added as resistance in series. This model also suggests that units in parallel flow can function as a pressure relief valve, leading to a sudden and amplified change in flow speed, which can be tuned by adjusting the units' resistance.

The final chapter is about another well-known unit called Miura ori unit (or four vertex unit). In contrast to the Waterbomb unit which deforms continuously from an initial shape to a flat state pre-snapping, this unit retains its initial shape and snaps directly to the second stable state. This is a consequence of the hidden degree of freedom arising from the facet bending in the unit. Thus, the four-vertex origami structure transitions between two rigid configurations using fluid loading. Adjusting the stiffness of this hidden degree of freedom allows us to control the structure's load-bearing capacity and compliance under fluid loading. Experiments were conducted to investigate the effects of various geometrical and mounting parameters, which serve as control factors to fine-tune the flipping process. Additionally, we demonstrated experimentally the combination of multiple units in series to have multiple rigid configurations, resulting in varied aerodynamic performance under different flow conditions.

We believe that the thesis will contribute to the nascent field of origami-based fluid-structure interaction. We demonstrated various drag-tuning possibilities that can be utilized for various functionalities. Origami-based structures can act as a design platform which provides finer passive shape control in a fluid flow. Each chapter begins with a brief overview of the main content and key objectives and concludes with a summary of the main results. Let us delve into the details.

Chapter 2

Tunable drag drop via flow-induced snap-through in origami

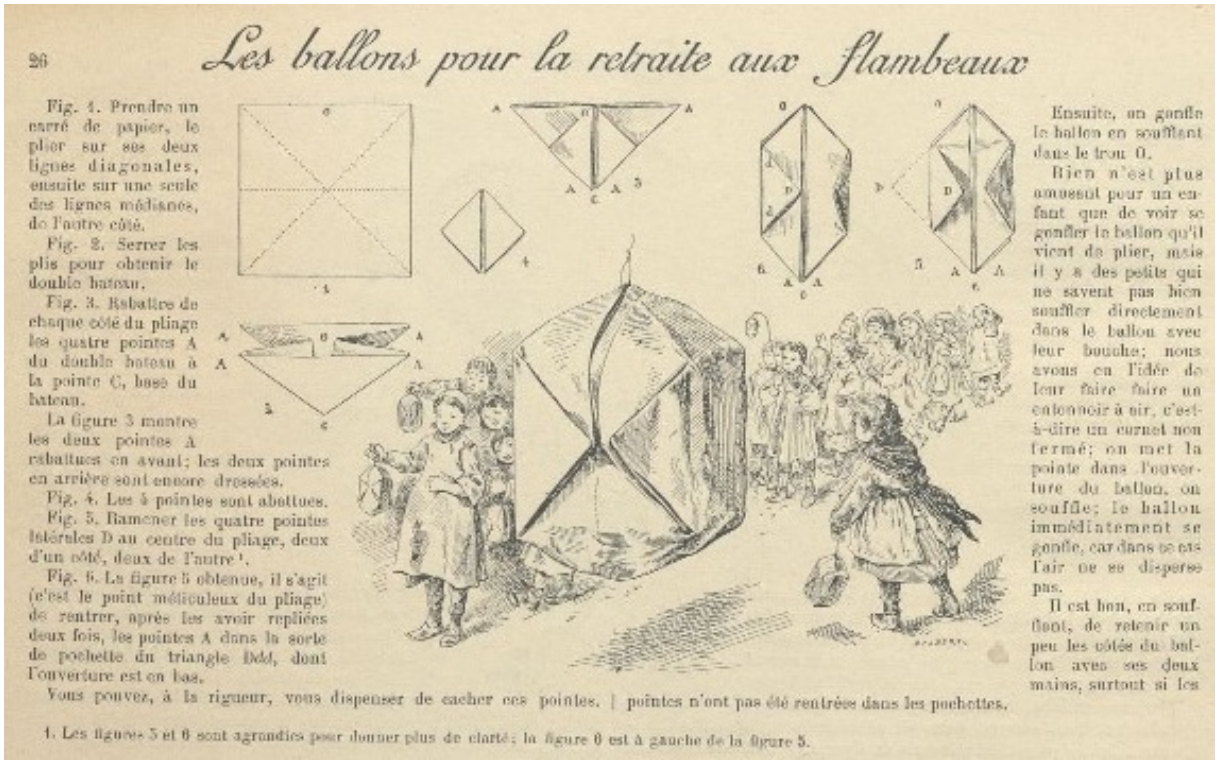
26

Les ballons pour la retraite aux flambeaux

Fig. 1. Prendre un carré de papier, le plier sur ses deux lignes diagonales, ensuite sur une seule des lignes médianes, de l'autre côté.

Fig. 2. Serrer les plis pour obtenir le double bateau.

Fig. 3. Rabattre de chaque côté du plinge les quatre pointes A du double bateau à la pointe C, base du bateau.

La figure 3 montre les deux pointes A rabattues en avant; les deux pointes en arrière sont encore dressées.

Fig. 4. Les 4 pointes sont abattues.

Fig. 5. Ramener les quatre pointes latérales D au centre du pliage, deux d'un côté, deux de l'autre [1].

Fig. 6. La figure 5 obtenue, il s'agit (c'est le point méticuleux du pliage) de rentrer, après les avoir repliées deux fois, les pointes A dans la sorte de pochette du triangle bdd, dont l'ouverture est en bas.

Vous pouvez, à la rigueur, vous dispenser de cacher ces pointes. | pointes n'ont pas été rentrées dans les pochettes.

Ensuite, on gonfle le ballon en soufflant dans le trou O.

Rien n'est plus amusant pour un enfant que de voir se gonfler le ballon qu'il vient de plier, mais il y a des petits qui ne savent pas bien souffler directement dans le ballon avec leur bouche; nous avons eu l'idée de leur faire faire un entonnoir à air, c'est-à-dire un carnet non fermé; on met la pointe dans l'ouverture du ballon, on souffle; le ballon immédiatement se gonfle, car dans ce cas l'air ne se disperse pas.

Il est bon, en soufflant, de retenir un peu les côtés du ballon avec ses deux mains, surtout si les

1. Les figures 5 et 6 sont agrandies pour donner plus de clarté; la figure 6 est à gauche de la figure 5.

Fun fact: One of the earliest designs of the Waterbomb unit in France is observed in 'Travaux Recreatifs Pour les enfants de 4 a 10 Ans' by Marie Koenig, which was published by Librairie Hachette et Cie in Paris in 1898. The book describes the folding pattern to make the Waterbomb structure which is shown to be utilized as a torch by the public.

The content of this chapter is the subject of a paper submitted to the Journal of Fluid Mechanics with some additional information.
This chapter is dedicated to the study of one of the fundamental origami units[89, 90] called the Water bomb unit in the flow. This umbrella-like unit has two stable states and features a rapid snap-through response as it transitions from one to the other. Origami structures have already raised interest for drag control, due to their large morphing capabilities [83, 84, 88, 91]. In particular, a previous study in the group on the Waterbomb base showed that its extreme reconfiguration tends to reduce drag to the point that it no longer increases with flow speed in the regime of large deformation [88]. Here, we make use of its bistable nature, which has not been utilized before for drag applications. Firstly, we demonstrate the potential for drag collapse with this unit due to its large shape change. We show that it produces a discontinuous evolution of drag with flow speed, marked by a sudden and significant drop as the structure snaps through. Then we systematically vary the geometrical and mechanical properties of the unit and show that it allows us to tune the drag discontinuity and the critical speed and loading at which it occurs. Experiments are captured by a simplified theoretical model that is further used for inverse design, which is finding the structural origami parameters that produce a targeted drag collapse.

Contents

2.1 Waterbomb unit

In this section, we give a brief overview of the Waterbomb unit cell highlighting its folding kinematics while giving details on the fabrication process of the unit. The kinematics will later be incorporated to make a fluid elastic model to depict the behaviour of the unit in airflow.

2.1.1 A unimodal and bistable origami mechanism

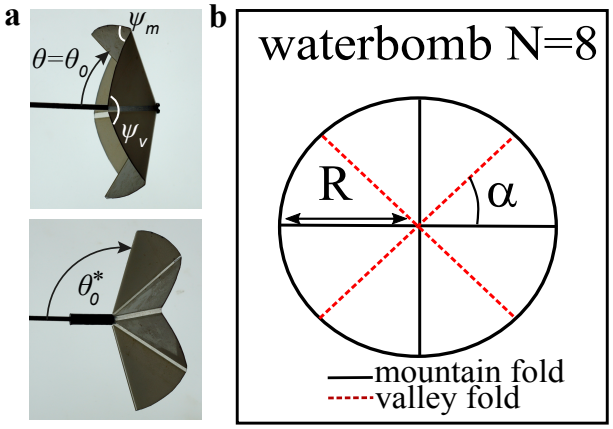

Figure 2.1: (**a**) Waterbomb unit with radius R, composed of eight alternating valley and mountain folds with respective angles ψ_v and ψ_m, and with unimodal kinematics (for symmetric folding) described by the angle θ. In the absence of loading, the unit sits in one of two stable equilibria with angle θ_0 and θ_0^*. (**b**) The Waterbomb unit was laid flat to demonstrate the sector angle between mountain and valley folds.

The Waterbomb base consists of a disk of radius R, featuring N creases with alternating mountain and valley folds distributed evenly with sector angle α around a central vertex (Fig.2.1b). The present study assumes the unit to be rigid-foldable. Namely, facets are considered rigid, with all movement occurring at the joints, thus simplifying the kinematic analysis. Additionally, we assume symmetry of motion, based on experimental observation, meaning that all the mountain folds deflect by the same amount, and the same holds for the valley folds. As a result, the mechanism reduces to one degree-of-freedom system [89, 92], where the shape of the entire structure can be determined from a single variable, chosen as the angle θ between a valley fold and the central axis passing through vertex (see Fig.2.1a).

Importantly, this unimodal origami mechanism has two stable equilibrium states and can transition between them through snapping. When at rest, the folded unit sits in one of these stable positions with its vertex pointing in one direction (see Fig.2.1a top). Upon applying an external force, the structure flattens out towards a plane that represents an unstable equilibrium. When displaced beyond this plane, it snaps through and moves to a second stable position with the vertex pointing in the opposite direction (see Fig.2.1a bottom). These two stable positions are characterized by angles θ_0 and θ_0^*, and although they may look similar in Fig.2.1left, they are not mirror images of each other. The relationship between the angles of mountain and valley folds, Ψ_m and Ψ_v (measured in terms of the deviation of straightness, see Fig.2.1a), and θ also differs on both sides of the unstable equilibrium [89] as we will see in the next section.

2.1.2 Folding kinematics

The folding kinematics(how the unit folds) of the Waterbomb base have been described extensively in previous work [88, 89, 93], and we only recapitulate here the main elements. The derivation given here is for a traditional Waterbomb unit, but it can easily be modified for any

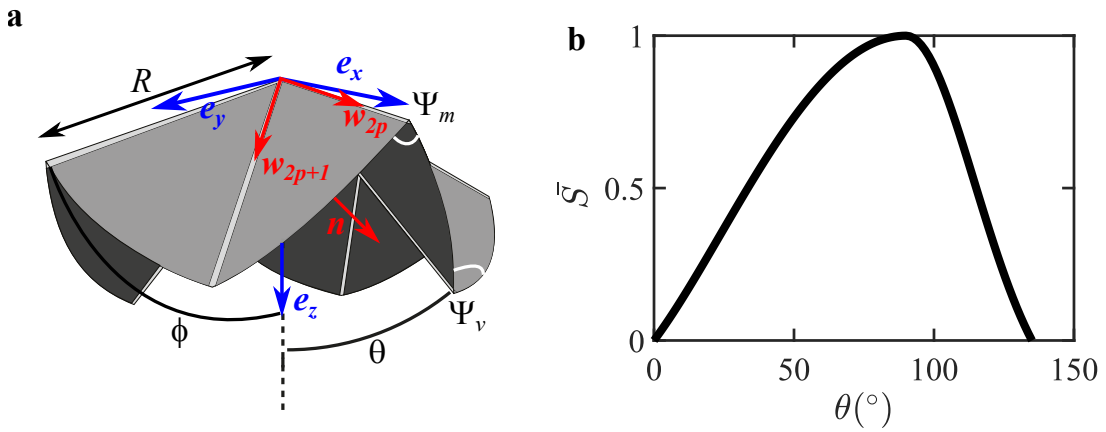

Figure 2.2: (**a**) Waterbomb base, featuring the various relevant angles, and the unit vectors $\boldsymbol{w_{2p}}$ and $\boldsymbol{w_{2p+1}}$ aligned along the mountain and valley creases. (**b**) Variation of the dimensionless projected area $\overline{S} = S/\pi R^2$ with the opening angle θ.

number of folds. The traditional version comprises a disk with a radius R, featuring $N = 8$ folds that radiate from the centre and are separated by equal sector angles $\alpha = 2\pi/N$. As discussed in the previous section we assume that the facet do not deform and folding is symmetric.

In line with [88, 93], the folding kinematics is derived by using the unit vectors $\boldsymbol{w_{2p}}$ and $\boldsymbol{w_{2p+1}}$, which are aligned respectively with the mountain and valley creases, with $p = 0, ..., 3$ and $\boldsymbol{w_0} = \boldsymbol{w_8}$. The components of these vectors in the Cartesian system coordinate, shown in Fig.2.2a, are:

$$\begin{aligned} \boldsymbol{w_{2p}} &= (\sin\phi\cos 2p\alpha, \sin\phi\sin 2p\alpha, \cos\phi) \\ \boldsymbol{w_{2p+1}} &= (\sin\theta\cos(2p+1)\alpha, \sin\theta\sin(2p+1)\alpha, \cos\theta) \end{aligned} \tag{2.1}$$

with ϕ the angle between valley folds and the central z-axis (see Fig.2.2a). The rigid facet assumption, expressed as $\boldsymbol{w_{2p}}.\boldsymbol{w_{2p+1}} = \cos\alpha$, establishes a relationship between θ and ϕ :

$$\cos\phi\cos\theta - \cos\alpha(1 - \sin(\phi)\sin(\theta)) = 0 \tag{2.2}$$

Equation 2.2 can be rewritten as :

$$\phi(\theta) = \begin{cases} \arccos\left(\dfrac{\cos\alpha\cos\theta}{1+\sin\alpha\sin\theta}\right) & \text{for } 0 \le \theta \le \pi/2 \\ \arccos\left(\dfrac{\cos\alpha\cos\theta}{1-\sin\alpha\sin\theta}\right) & \text{for } \pi/2 < \theta \le \pi - \alpha \end{cases} \tag{2.3}$$

The first relation describes the opening kinematics and the second one describes the closing past the flat configuration $\theta = \pi/2$. The angles of the mountain and valley folds denoted as ψ_m and ψ_v respectively, can be expressed in terms of θ and ϕ [93]:

$$\begin{aligned} \cos\psi_v &= \cos 2\theta \\ \cos\psi_m &= \cos 2\phi \end{aligned} \tag{2.4}$$

Their expression as a function of θ thus differs on each side of the flat configuration. By taking the projection of the area of the unit in the xy-plane we obtain the projected area S, which will later be used to describe the origami kinematics, rather than θ, since it is easily accessible experimentally. The non-dimensional expression (normalizing by the area of the flat state πR^2) for the projected area S is given by:

$$\overline{S} = \frac{S}{\pi R^2} = \boldsymbol{n}.\boldsymbol{e_z} = \sin\theta\sin\phi \tag{2.5}$$

Where $\boldsymbol{n}$ is the unit vector normal to the facet defined by vectors $\boldsymbol{w_{2p}}$ and $\boldsymbol{w_{2p+1}}$:

$$\boldsymbol{n} = \frac{\boldsymbol{w_{2p}} \times \boldsymbol{w_{2p+1}}}{||\boldsymbol{w_{2p}} \times \boldsymbol{w_{2p+1}}||} \tag{2.6}$$

The evolution of the dimensionless projected area $\overline{S}$ of the unit with the opening angle θ as the unit opens up and closes is shown in Fig.2.2b. We see that $\overline{S}$ is 0 for $\theta = 0$ and 135° denoting fully closed states before and after snapping for the unit with 8 folds. Also, it reaches 1 for $\theta = 90°$ when it is a flat disk. In a later section, we will see this plot for different numbers of folds.

2.1.3 Elastic potential energy and bistability

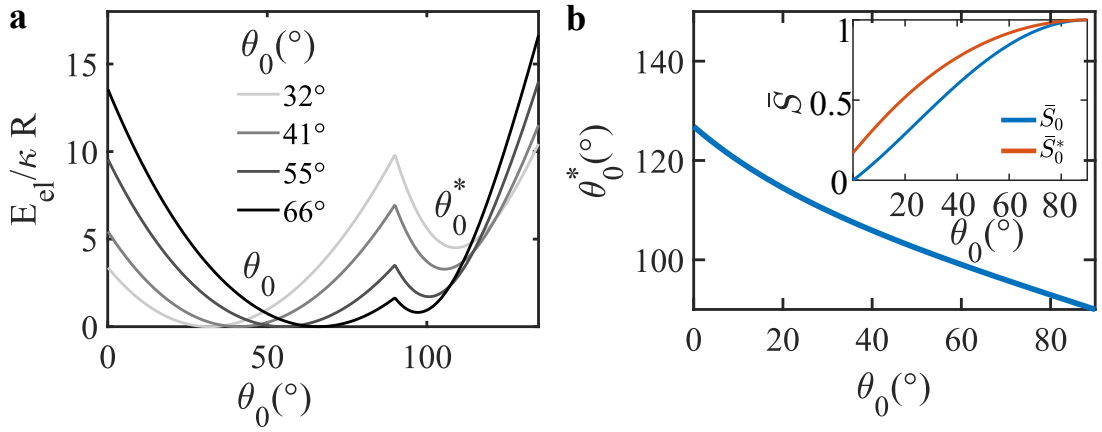

Figure 2.3: (**a**) Elastic potential energy landscape for the Waterbomb base, displaying two stable states with angles θ_0 and θ_0^*, separated by an unstable planar state, for varying θ_0. (**b**) Evolution of θ_0^* with θ_0. Corresponding dimensionless projected areas $\overline{S_0}$ and $\overline{S_0^*}$ are shown in the inset.

The mechanical behaviour of the origami unit is modelled by treating its folds as elastic hinges with rigidity κ and length R. The elastic potential energy comprises contributions from the $N/2$ mountain folds and the $N/2$ valley folds:

$$E_{el} = \frac{N\kappa R}{4}[(\psi_m - \psi_m^0)^2 + (\psi_v - \psi_v^0)^2] \tag{2.7}$$

Here, ψ_m^0 and ψ_v^0 denote the rest angles of the mountain and valley folds. Using the angle expressions from Eq.2.3 and Eq.2.4, E_{el} can be expressed as a function solely of θ and θ_0. Fig.2.3a shows the evolution of the normalized elastic potential energy $E_{el}/\kappa R$ as a function of θ for various rest angles θ_0. The energy landscape features two wells corresponding to two stable states, which are separated by an unstable flat state at $\theta = \pi/2$. Smaller values of θ_0 (corresponding to compact states, light grey curve) have a higher energy barrier to overcome to transition to the second stable state. The second equilibrium configuration is also correspondingly more compact (higher θ_0^*), resulting in a more pronounced shape change upon snapping. The relationship between θ_0^* and θ_0 can be numerically determined through energy minimization for a given θ_0, as illustrated in Fig.2.3b. The inset of Fig.2.3b also shows the evolution of the dimensionless projected area $\overline{S_0}$ and $\overline{S_0^*}$ for the two stable states, showing that the two states are not the mirror image of each other and that the second one is always slightly more open than the first one.

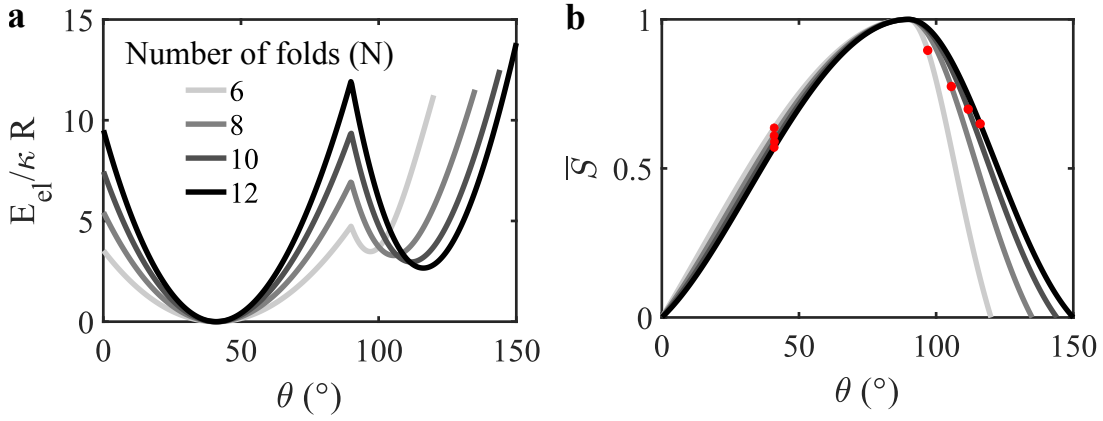

Figure 2.4: (**a**) Elastic potential energy landscape for the Waterbomb base for a varying number of folds N. (**b**) The folding kinematics of the Waterbomb unit with $\theta_0 = 41°$ and different numbers of folds. The red points correspond to the first and second stable states on the left and right sides of the flat state respectively.

2.1.4 Elastic potential energy for different number of folds

We see that increasing the number of folds increases the potential energy barrier that the unit needs to cross to go to the second stable state as depicted in Fig.2.4a. The unit with a higher number of folds also has lower elastic potential energy for the second stable state. Also, the normal area of the second stable state becomes lower with the increasing number of folds, indicating the second stable state becomes more closed on increasing the number of folds (see Fig.2.4b). Thus, changing the number of folds not only modifies the potential energy of the unit but also modifies the folding pathway. This modification seems more pronounced in the closing phase of the unit($\theta > 90°$) in comparison to the opening phase($\theta < 90°$).

2.1.5 Fabrication of the origami unit

Specimens are fabricated using a technique developed in a previous study [88] and inspired by the literature [94, 95], which is based on layer superposition. The rigid facets are laser cut from a 350μm thick sheet of Mylar (Polyethylene terephthalate, abbreviated as PET), which is then attached to a thinner sheet using double-sided tape with a 2.5 mm spacing that forms the creases. The unit is then hand folded and maintained in a desired configuration on a mount, placed in a heating chamber for an hour at 75°C, and then left to cool down at room temperature. See Fig.2.5a for the fabrication process. It thus effectively prescribes the first stable state θ_0 and the corresponding second stable state θ_0^*. One such unit with rest state 41° and its corresponding second stable state is depicted in Fig.2.5b. This annealing process relaxes any residual stresses that might have been created during folding [90] so that the first stable state is close to a zero-energy state. Here, we have utilized the thermo-formable property of the material. As shown in a previous study, the folds then operate as torsional springs, exhibiting elastic behaviour around their assigned rest angle [88]. The side view and the bending of a single fold are depicted in Fig.2.5c. By laser cutting, the radius and number of folds of the origami unit can be easily modified. The rest angle is modified by putting the unit in the desired opening angle in the mount whereas the stiffness can be adjusted by using different thicknesses of the thin sheet, ranging from $40 - 100\mu$m.

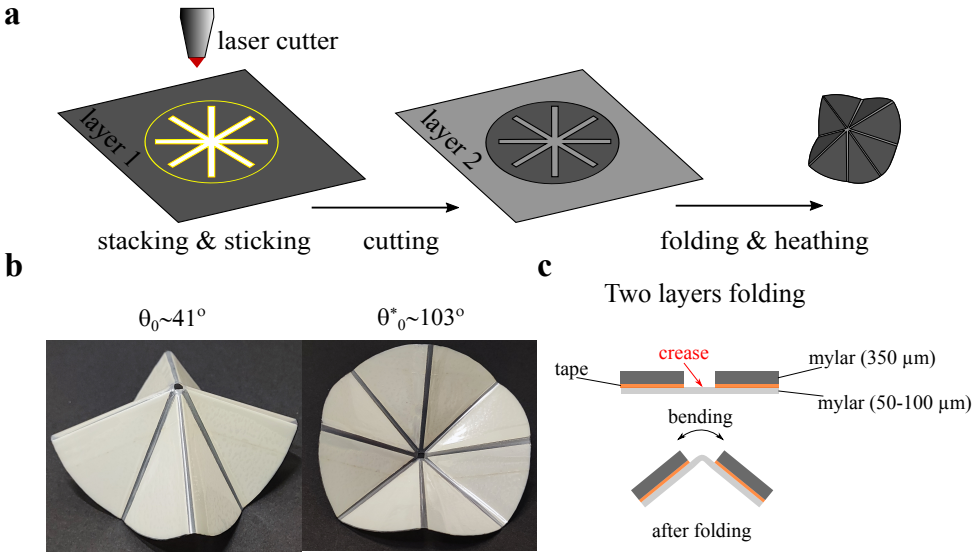

Figure 2.5: (**a**) Fabrication process using layer superposition. (**b**) Two stable states of the unit for the rest angle 41° and (**c**) side view and bending of the fold.

Sheet Thickness (μm)	48	50	75	100
Fold stiffness κ(N) $\times 10^{-3}$	8	19	53	92

Table 2.1: Stiffness measured for folds made from sheets with different thicknesses.

2.1.6 Fold stiffness measurement

To measure fold stiffness, a prototype of a single crease was designed. Two facets are laser-cut in a 350 μm thick sheet of Mylar and adhered to a thinner sheet using a double-sided tape with a 2.5 mm spacing, constituting the flexural hinge. While keeping one of the facets vertically fixed, we apply a variable point load to the geometrical centre of the free facet and extract the opening angle of the fold Ψ (see Fig.2.6a). The opening angle in the absence of load is set to $\Psi_0 \approx 113°$ for all the tests, but note that the stiffness was found independent of Ψ_0 in the previous study of [88]. The fold acts as a torsional spring between two rigid facets, exhibiting a linear relationship between the torque applied T (accounting for the weight of the hanging facet as well) and the angular deviation $\Psi - \Psi_0$ (see Fig.2.6b). The stiffness is extracted from the slope as $T = \kappa L(\Psi - \Psi_0)$, with $L = 4$ cm the crease length. Table 2.1 displays κ values for the four thin sheets. Repeatability and robustness were assessed by measuring κ for eight folds from a 50 μm sheet, resulting in an 8% variability based on standard deviation relative to the mean value.

2.2 Drag collapse through snapping

In this section, we explore the behaviour of the Waterbomb unit in the presence of fluid loading while shedding light on the influence of various geometrical and mechanical parameters on this behaviour.

2.2.1 Experimental setup and typical drag collapse

For the experimental tests Origami units are subjected to a steady air flow generated by an open jet wind tunnel with a square cross-section of width 40 cm and flow speed varied in $1 - 16$ m/s.

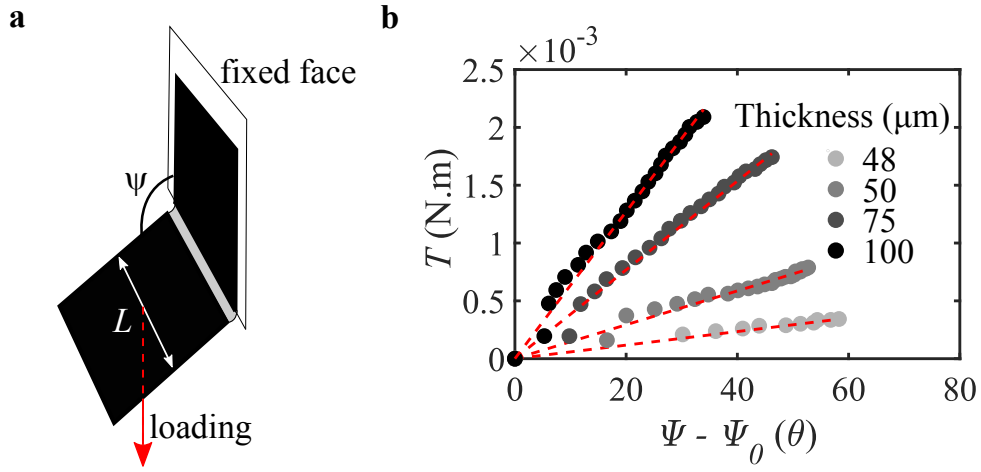

Figure 2.6: (**a**) Fold stiffness is assessed by measuring the opening angle Ψ of a single fold while applying a variable point force at the centre of the free facet. (**b**) Torque T as a function of the angular deflection relative to the rest angle $\Psi - \Psi_0$, for folds made from sheets of varying thickness.

An elbow arm is used upstream, to hold the unit at its vertex in the centre of the cross-section (see Fig.2.7a). This arm is connected to a six-component force sensor, measuring the drag component of the fluid force in the direction of the flow. For each measurement, we average the drag over 30 seconds and subtract the drag on the support system alone. The flow-induced shape changes are characterized through the projected area S of the unit in the plane perpendicular to the flow, captured by a camera placed downstream and extracted through Matlab custom image analysis. The observed kinematics align with the unimodal mechanism described earlier, which is rigidly foldable with motion restricted to the joint and exhibits rotational symmetry of motion. The entire geometry of the unit can be reconstructed from S, which will be further used as the observable to measure shape reconfiguration.

Fig.2.7b-c displays the results of a typical experiment. The unit is initially in its first stable position θ_0, with the concave side facing the flow. As the flow speed gradually increases, the cell symmetrically opens up. The expansion of the frontal area, reported in Fig.2.7c, leads to a faster increase of drag with flow speed (solid black curve in Fig.2.7b) compared to the classical U^2 law observed for a rigid cell frozen in its initial configuration (dashed grey curve in Fig.2.7b). When the cell reaches the unstable flat state, it snaps to a more compact and streamlined configuration. Note that slight cell vibrations make it challenging to precisely attain $S/\pi R^2 = 1$. The sudden reconfiguration results in a discontinuity in the drag force on the unit, and the shape change is significant enough to produce a drag-drop by up to 69% among the specimens tested in this study. As U is further increased, the unit closes up, reducing the frontal area exposed to flow. This closing regime has been extensively studied in a previous study [88]; it features an increase of drag that is slower than the quadratic U^2 law for rigid objects, owing to the reduction in frontal area combined with shape streamlining.

We thus observe a non-continuous evolution of drag with flow speed with a marked collapse. This behaviour can be described by selected observable parameters, namely the critical flow velocity of the snapping U_c, the maximum drag force reached just before snapping $F_{d,max}$, and the subsequent drag drop ΔF_d. These parameters are prominent features characterizing the discontinuity but are also relevant for practical applications, such as designing protection devices or valves. They determine a maximum load, the amount of load reduction, or the critical speed at which the structure would operate. In the following sections, we investigate how those quantities are related to the origami geometrical and mechanical properties, specifically its size R, rest configuration θ_0, number of folds N, and fold stiffness κ. Before that, let's quickly go

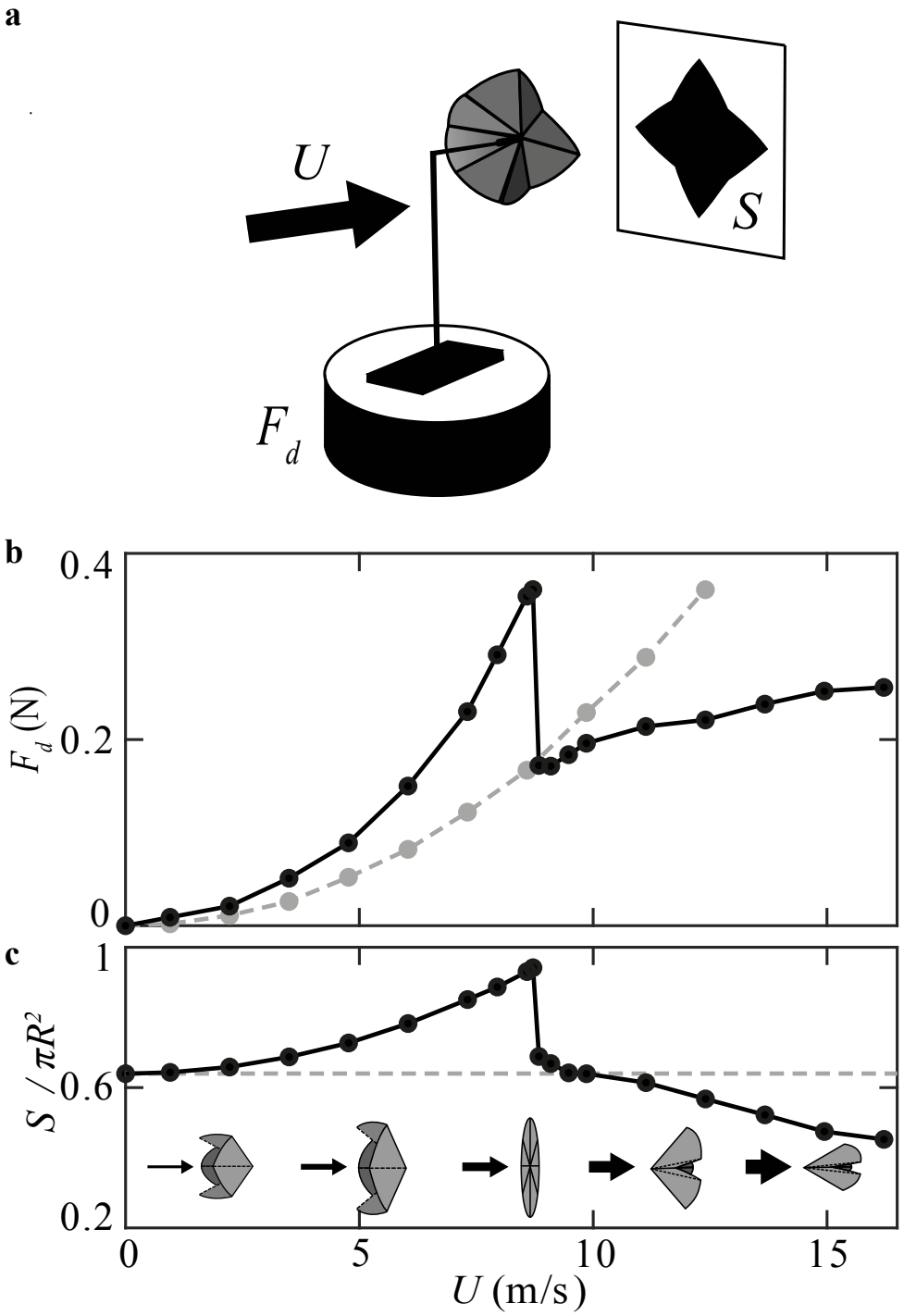

Figure 2.7: Drag collapse through flow-induced snap-through of a bistable origami unit.(**a**) Experimental setup for the drag measurement. The Waterbomb unit is mounted on the force sensor with a 3D-printed elbow joint with a concave side facing the flow. The evolution of the frontal area (S) is captured with the camera placed downstream. Evolution of (**b**) the drag force F_d on the bistable origami cell when exposed to a uniform airflow with increasing velocity U, and of (**c**) its dimensionless frontal area $S/\pi R^2$ projected in the plane perpendicular to the flow. The drag collapse observed in the snapping unit (with $R = 5$ cm, $\kappa = 19 \times 10^{-3}$ N and $\theta_0 = 41°$, black solid curves) is contrasted with the quadratic drag experienced by a rigid unit with the same geometry (same R and θ_0, grey dashed curves).

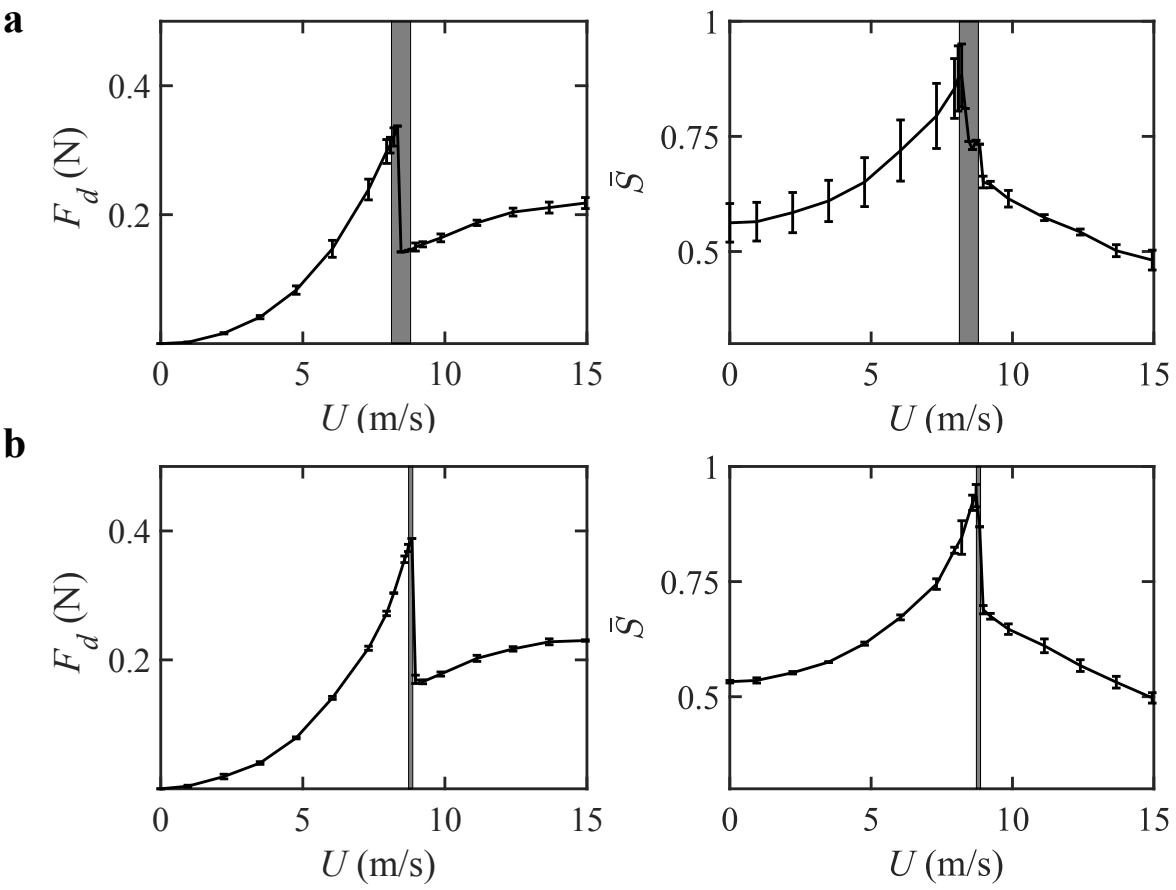

Figure 2.8: Evolution of drag force F_d and dimensionless projected area $\overline{S} = S/\pi R^2$ with flow speed U, for origami specimens with $R = 5$ cm, $\kappa = 19 \times 10^{-3}$ N and $\theta_0 = 41°$. In (**a**), experiments are replicated across five independent cells sharing the same parameters. In (**b**), the same cell is tested three times, with re-annealing between each iteration. Data points represent the mean values, and error bars indicate the standard deviation (the grey zone denotes the variation in critical speed).

through the repeatability of the experiments and the percentage error in various measurements.

2.2.2 Repeatability of the experiments

To test the reproducibility of the experiments and of the fabrication process, we repeated experiments in the wind tunnel for five distinct units fabricated with identical parameters $R = 5$ cm, $\kappa = 19 \times 10^{-3}$ N and $\theta_0 = 41°$ (which is the common configuration for all three parametric series of origami cells). Fig.2.8a presents the mean values for drag and the cell projected area, with error bars corresponding to the standard deviation. The grey region denotes the variation in the critical speed for snap-through U_c. The associated relative errors are of the order of 7%, 9.5% and 5%, respectively for F_d, $S/\pi R^2$ and U_c. The higher spread in the projected area is attributed to the use of instantaneously captured images, while the units tend to slightly flutter when approaching the unstable planar state.

To pinpoint the primary source of error, we also conducted three repetitions of the experiments using the same unit. Before each test, the unit underwent an hour of re-annealing in the oven, followed by an additional hour of cooling at room temperature to ensure a consistent initial cell configuration. The mean values and standard deviations for the measurements are depicted in Fig.2.8b. The relative error in both plots is within 2%. The reduced variability com-

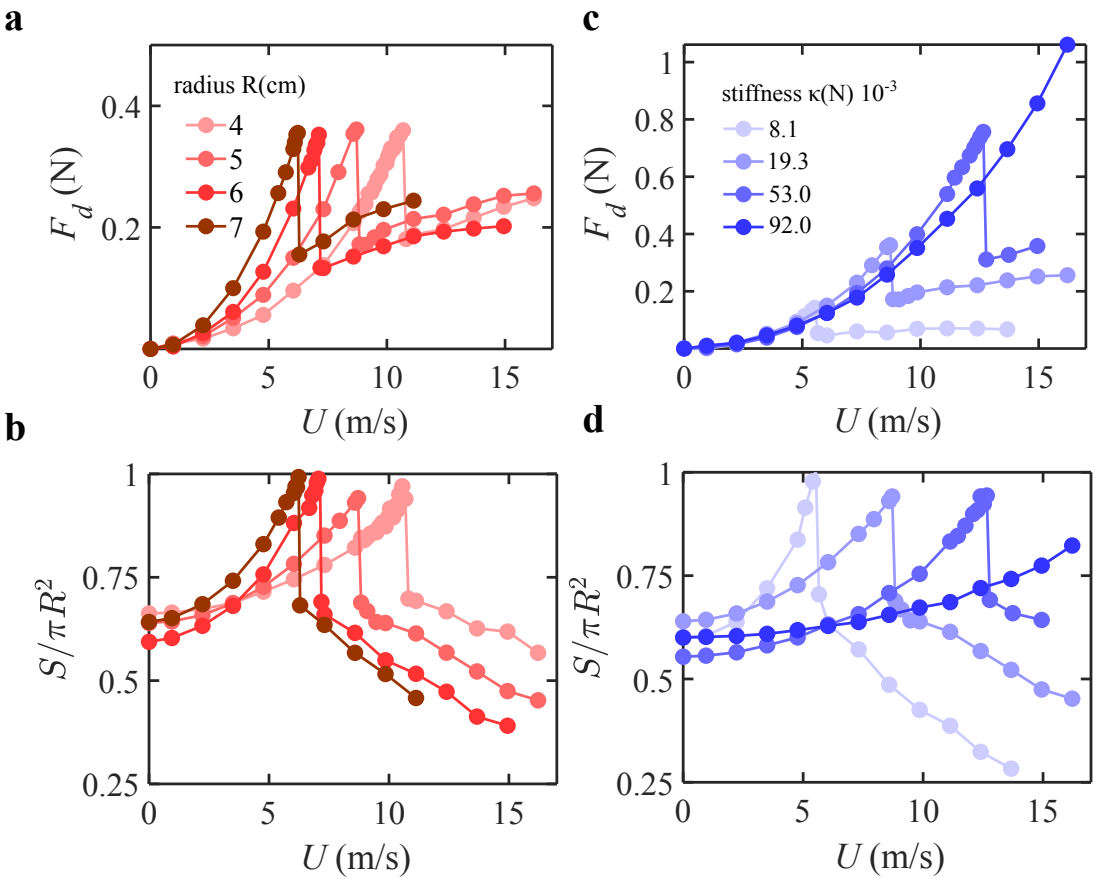

Figure 2.9: Influence of the radius and fold stiffness on drag. Evolution of (**a** and **c**) the drag force F_d and (**b** and **d**) the dimensionless frontal area $S/\pi R^2$ as a function of flow velocity U, for origami units with different (**a-b**) radii R and (**c-d**) fold stiffness κ. The unit $R = 5$ cm, $\kappa = 19 \times 10^{-3} N$, $N = 8$ and $\theta_0 = 41°$ is common to all graphs.

pared to Fig.2.8a suggests that the predominant source of variability comes from the fabrication process rather than the experimental measurement method, notably concerning the detection of the snap-through threshold.

2.2.3 Influence of size and stiffness

This section is designated to our exploration of the influence of different stiffness and radii on the drag behaviour. We first vary the radius R of the unit, while keeping the stiffness to be $\kappa = 19 \times 10^{-3}$ N, the number of folds to be $N = 8$ and the rest angle to be $\theta_0 = 41°$. Note that fabrication produces a small variability in the rest angle among specimens, which is visible in Fig.2.9b in the 6% dispersion in the dimensionless frontal area in the absence of flow ($U = 0$). As shown in Fig.2.9a-b, all units exhibit the characteristic behaviour described earlier, that is a non-continuous evolution of drag with flow speed with a sudden drop associated with the snap-through of the origami unit. However, bigger units (darker red curves) initially experience a higher fluid loading, because of the larger area exposed to the flow. As a result, they reach the flat state $S/\pi R^2 = 1$ faster and flip at a lower critical speed (see Fig.2.9b). Interestingly, in Fig.2.9a, the maximum drag $F_{d,max}$ experienced by the units before snapping is the same, and they feature similar jumps amplitude ΔF_d. Changing the radius of the unit thus primarily shifts the critical velocity U_c at which the drag collapse occurs, while preserving $F_{d,max}$ and ΔF_d.

Fig.2.9c-d shows the results for origami cells with different fold stiffness, but the same size $R = 5$ cm, number of folds $N = 8$ and rest angle $\theta_0 = 41°$ (with a similar degree of variability

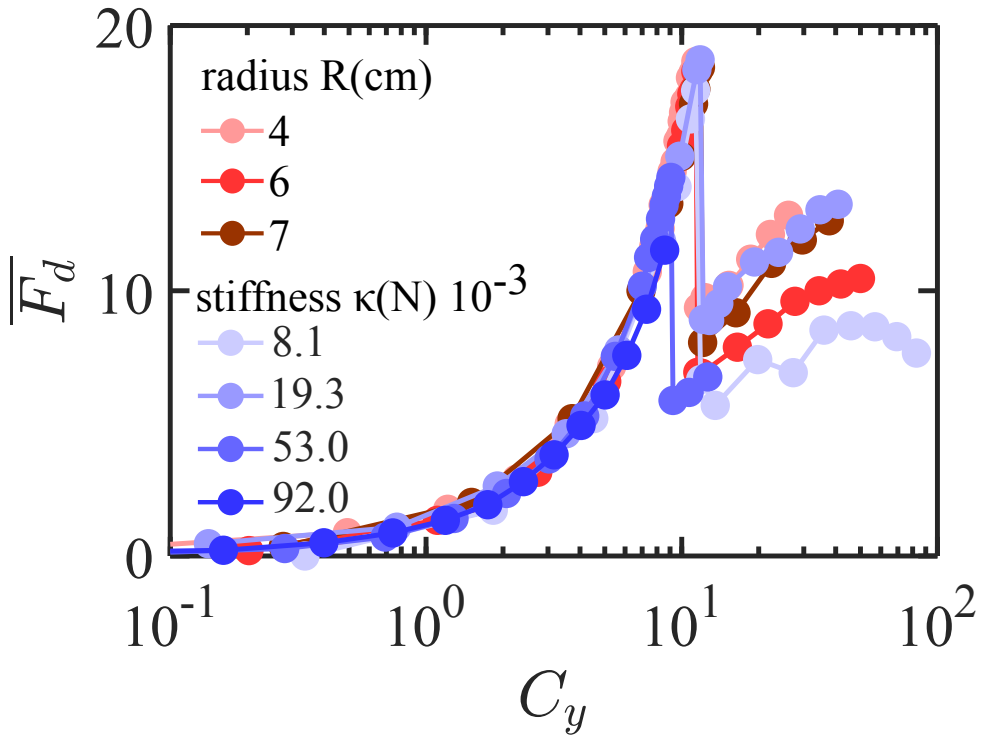

Figure 2.10: Evolution of the dimensionless drag $\overline{F_d} = F_d/\kappa$ as a function of the Cauchy number $C_y = \rho U^2 R^2/\kappa$ for origami units with different radii R and fold stiffness κ (while maintaining the same rest angle $\theta_0 = 41°$ and number of folds $N = 8$). Experimental data are presented with the same markers and colour code as in Fig.2.9.

as earlier). Stiffer units (darker blue curves) deploy slower with increasing U owing to larger resistance to deformation, and reach the flat state at larger critical velocities (see Fig.2.9d). The most rigid one does not reach this unstable point within the range of flow covered here. Snapping at larger speeds U_c results both in higher drag peak values $F_{d,max}$ and larger jumps ΔF_d (see Fig.2.9c). Stiffness thus affects all three drag features, offering an additional lever for control.

The trends observed through variations in parameters reflect the interplay between external fluid loading and elastic restoring forces of the origami unit, which governs the unit's reconfiguration process. This fluid-elastic competition can be analyzed in terms of Cauchy number C_y, as introduced in a previous study [88] and frequently used in the literature [30, 33, 96]. This dimensionless number examines the relative magnitudes of the work done by fluid forces, $\rho U^2 R^3$, and the elastic energy of folding, κR:

$$C_y = \frac{\rho U^2 R^2}{\kappa} \tag{2.8}$$

In Fig.2.10, drag measurements are re-plotted in the dimensionless form $\overline{F_d} = F_d/\kappa$ as a function of C_y, using the fold stiffness κ as a characteristic force scale, in line with [88]. Here, we only report data for units with different stiffness κ and radius R, which share the same initial rest configuration θ_0 and number of folds N. Data collapse onto a master curve, with a drag peak and subsequent jump that are solely set by the fold stiffness, and which occur at a critical Cauchy number of $C_{y,c} \approx 14$ for all units. The dimensionless quantities C_y and $\overline{F_d}$ capture the effect of origami size and stiffness in fluid-elastic mechanisms. However, it does not account for the more intricate influence of the rest angle θ_0 and number of folds N as we will discuss in the next section.

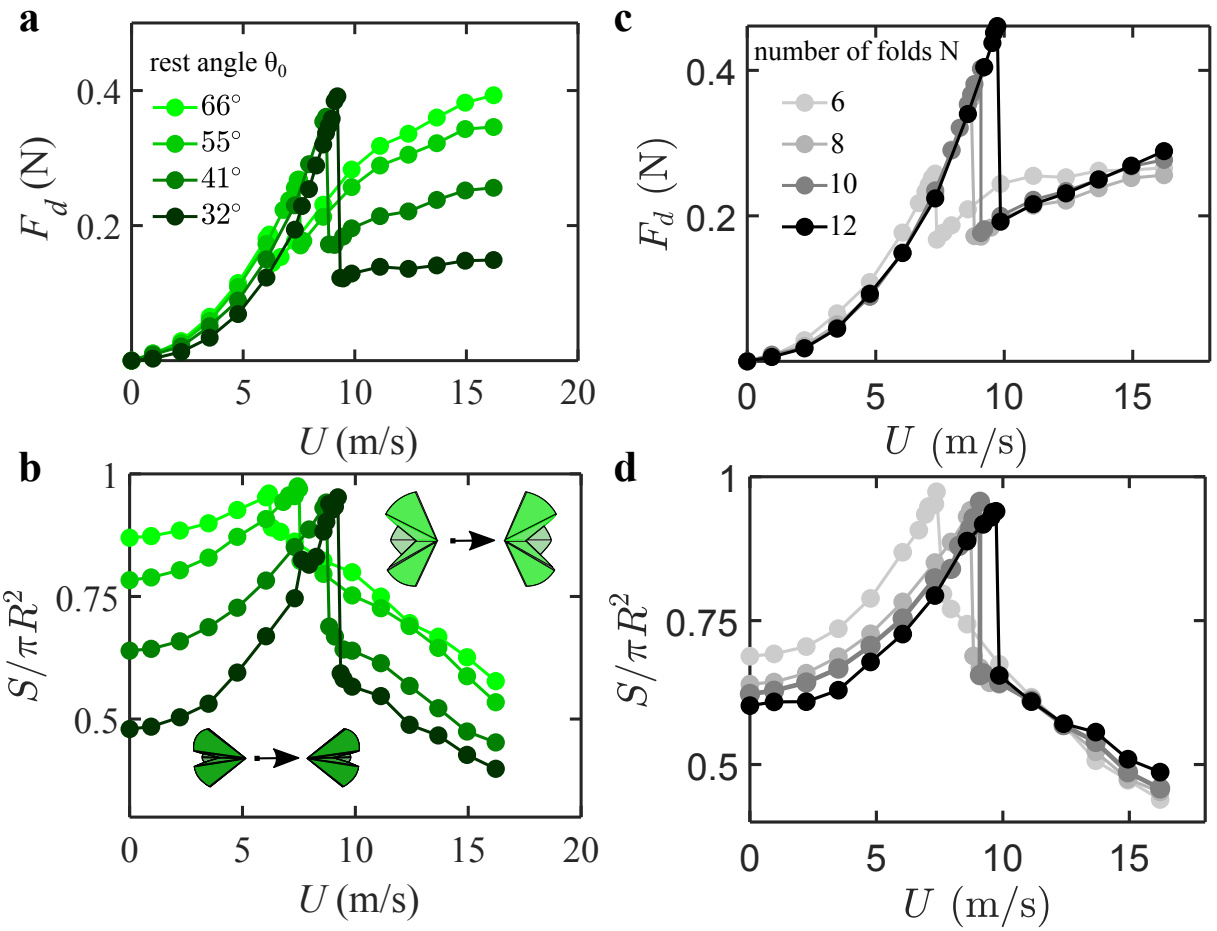

Figure 2.11: Influence of the rest angle and number of folds on drag. Evolution of (**a** and **c**) the drag force F_d and (**b** and **d**) the dimensionless frontal area $S/\pi R^2$ as a function of flow velocity U, for origami units with different (**a**-**b**) rest angle θ_0 and (**c**-**d**) number of folds N . The unit $R = 5$ cm, $\kappa = 19 \times 10^{-3} N$, $N = 8$ and $\theta_0 = 41°$ is common to all graphs.

2.2.4 Influence of the rest angle and the number of folds

Now we vary the degree of opening of the cell rest state θ_0, while keeping the size, number of folds and stiffness constant as $R = 5$ cm, $N = 8$ and $\kappa = 19 \times 10^{-3}$ N respectively. Starting from a more compact rest state (dark green curves) delays the flipping towards higher flow velocities, as depicted in Fig.2.11a. Intuitively, reaching the flat state that is further away requires greater work from fluid loading. As was the case for the κ-series of units, snapping at greater U_c results in larger maximal drag $F_{d,max}$ in Fig.2.11a. As mentioned earlier and illustrated in the schematics of Fig.2.3a, changing θ_0 also affects the degree of closure of the second stable state. Small θ_0 (dark green) results in a larger collapse in the frontal area post-snapping compared to units initially more opened (light green) in Fig.2.11b. It correspondingly leads to larger jumps in drag ΔF_d in Fig.2.11a.

Finally, we vary the number of folds N, while keeping the size, stiffness and rest angle as $R = 5$ cm, $\kappa = 19 \times 10^{-3}$ N and $\theta_0 = 41°$ respectively. Increasing the number of folds has a similar effect to changing θ_0 i.e., it changes the energy barrier and the degree of opening of the second stable state (Fig.2.3 and Fig.2.4). A consequence of this can be seen in Fig.2.11c, the unit with a higher number of folds (black curve) flips at a higher flow rate leading to a larger change in drag force in comparison to the unit with a lower number of folds (light grey curve). While modifying the potential energy curve, the number of folds also modifies the folding pathway of the unit (Fig.2.4b), unlike changing θ_0. The units with a different number of folds post-snapping

converge to a similar drag value(2.11c) and the frontal area evolution(2.11d) is also the same in contrast to the units with different rest state where there is a clear distinction between different units. As the influence of the rest state is more prominent on the jump and post-snapping behaviour, it seems to be a better drag-tuning parameter than a number of folds. By changing the four sets of parameters discussed above we can change the three drag characteristics U_c, $F_{d,max}$, and ΔF_d.

2.3 Theoretical fluid-structure model

Next, we develop a simplified theoretical model to further explore and corroborate the link between the origami unit's characteristics and drag. The Reynolds number for our experiments falls within the range $Re = UR/\nu \approx 10^3 - 10^5$, where form drag predominates over friction drag, and the latter is neglected.

2.3.1 Theoretical modelling

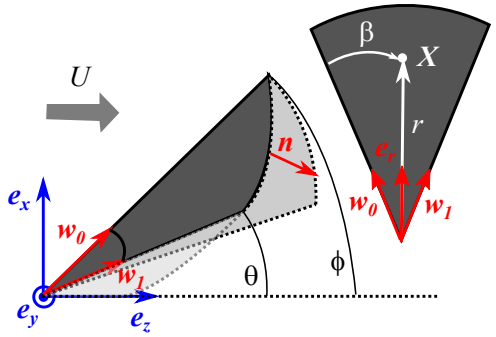

Figure 2.12: Parameterization used to compute the work of fluid forces on a facet defined by the unit vectors $\boldsymbol{w_0}$ and $\boldsymbol{w_1}$.

To model the origami unit's response to a flow, we adopt the same energy-based approach from prior work on the Waterbomb unit's closing dynamics of the Waterbomb in a flow [88]. We recapitulate here the main elements and extend it to include snapping. The unit's static equilibrium in a flow is determined by minimizing its energy $E_{el} - W$, which includes both the elastic potential energy E_{el}, and the work done by fluid forces W as the unit deforms from its initial rest state θ_0 to an angle θ:

$$E_{el} - W = \frac{N\kappa R}{4}[(\psi_m - \psi_m^0)^2 + (\psi_v - \psi_v^0)^2] - N\int_{\theta_0}^{\theta}\int_{S_f} \rho(\boldsymbol{U}.\boldsymbol{n})^2 dS_f \boldsymbol{n}.d\boldsymbol{X} \tag{2.9}$$

Where ρ denotes the density of the fluid and other quantities are introduced later. The second term sums the work done by fluid loading on each facet (with area $S_f = \pi R^2/N$), which is the same for all of the facets due to the symmetry of motion. Fluid pressure forces acting on each surface element of a facet are integrated along the local displacement $d\boldsymbol{X}$. Note that $\boldsymbol{n}$ and $\boldsymbol{X}$ are functions of the folding angle θ. Pressure is modelled using the momentum conservation arguments, following the approach in [30–32, 88]. It scales with the momentum carried by the flow in the direction perpendicular to the facet $\rho(\boldsymbol{U}.\boldsymbol{n})^2$, with $\boldsymbol{n}$ the normal unit vector as defined in Eq.2.6.

As discussed in Ref.[88], friction forces likely become significant in regimes with substantial deformation, where facets nearly align with the flow. However, this particular regime is not reached in our present study. Consistent with earlier studies on the reconfiguration of flexible

structures in a flow [30–32, 88], pressure is computed using conservation of momentum principles. While simplified, this model has demonstrated effectiveness in capturing fluid-elastic behaviours [30–32, 88]. It offers a reasonable approximation of more complex potential flow expressions [34, 88], which would be challenging to implement for three-dimensional geometries. The trajectory $\boldsymbol{X}$ of each surface element of a facet is obtained from the kinematics analysis presented earlier. We consider the facet of Fig.2.12 associated with the crease vector field $\boldsymbol{w_0}$ and $\boldsymbol{w_1}$. A point on the facet is localized through the distance $r \in [0, R]$ and polar angle $\beta \in [0, \alpha]$, as shown in Fig.2.12. Its position vector is expressed as $\boldsymbol{X} = r\boldsymbol{e_r}$ with $\boldsymbol{e_r}$ the radial unit vector. This vector lies in the $(\boldsymbol{w_0}, \boldsymbol{w_1})$ plane and can thus be expressed as a linear combination of these two vectors:

$$\boldsymbol{e_r} = \frac{\boldsymbol{w_0} + C\boldsymbol{w_1}}{||\boldsymbol{w_0} + C\boldsymbol{w_1}||} = \frac{\boldsymbol{w_0} + C\boldsymbol{w_1}}{\sqrt{1 + 2C\cos\alpha + C^2}} \text{ with } C \text{ verifying } \boldsymbol{e_r}.\boldsymbol{w_0} = \cos\beta \tag{2.10}$$

From Eq.2.10, the parameter C can be expressed as a function of α and β:

$$C = \frac{-\cos\alpha(\cos^2\beta - 1) + \cos\beta\sqrt{(\cos^2\beta - 1)(\cos^2\alpha - 1)}}{\cos^2\beta - \cos^2\alpha} \tag{2.11}$$

Deformation of the origami unit by $d\theta$ results in elementary displacements $d\boldsymbol{X}$ for points of the facet :

$$d\boldsymbol{X} = r\frac{d\boldsymbol{e_r}}{d\theta}d\theta = \frac{rd\theta}{\sqrt{1 + 2C\cos\alpha + C^2}}\left(\frac{d\phi}{d\theta}\cos\phi + C\cos\theta\cos\alpha, C\cos\theta\sin\alpha, -\frac{d\phi}{d\theta}\sin\phi - C\sin\theta\right) \tag{2.12}$$

The work done by fluid forces on all of the facets then writes:

$$W = -\frac{NR^3\rho U^2}{3}\int_{\theta_0}^{\theta}\sin^2\theta\sin^2\phi\left[A\frac{d\phi}{d\theta}\sin\theta + B\sin\phi\right]d\theta \tag{2.13}$$

With A and B given by:

$$A = \int_0^{\alpha}\frac{1}{\sqrt{1 + 2C\cos\alpha + C^2}}d\beta \quad \text{and} \quad B = \int_0^{\alpha}\frac{C}{\sqrt{1 + 2C\cos\alpha + C^2}}d\beta \tag{2.14}$$

The equilibrium angle θ of the unit in the flow is then given by the zeros of $d(E_{el} - W)/d\theta$, which yields the equation:

$$(\psi_m - \psi_m^0)\frac{d\psi_m}{d\theta} + (\psi_v - \psi_v^0)\frac{d\psi_v}{d\theta} + \frac{2}{3}C_y\sin^2\theta\sin^2\phi\left[A\frac{d\phi}{d\theta}\sin\theta + B\sin\phi\right] = 0 \tag{2.15}$$

Where $C_y = \rho U^2R^2/\kappa$ is the same Cauchy number as defined for experiments. Eq.3.5 is numerically solved using the nonlinear system solver *fsolve* of Matlab. The Cauchy number is varied linearly from 0 to 50 in 500 steps, and the solver utilizes the value of θ obtained at the previous iteration as a starting point (initializing at θ_0 for $C_y = 0$). As θ approaches the flat state beyond $\pi/2 - \epsilon$, with $\epsilon = 0.01$ radians, Eq.3.5 is then solved using the new set of equations describing the angles in the closing part of the kinematics (given in Eq.2.3) with first starting point at $\pi/2 + \epsilon$.

From the equilibrium angle θ, we obtain the dimensionless projected surface $\overline{S}$ using Eq.2.5, and the dimensionless drag force by projecting pressure fluid forces in the direction of the flow $\boldsymbol{e_z}$:

$$\overline{F_d} = F_d/\kappa = \pi C_y\sin^3\theta\sin^3\phi \tag{2.16}$$

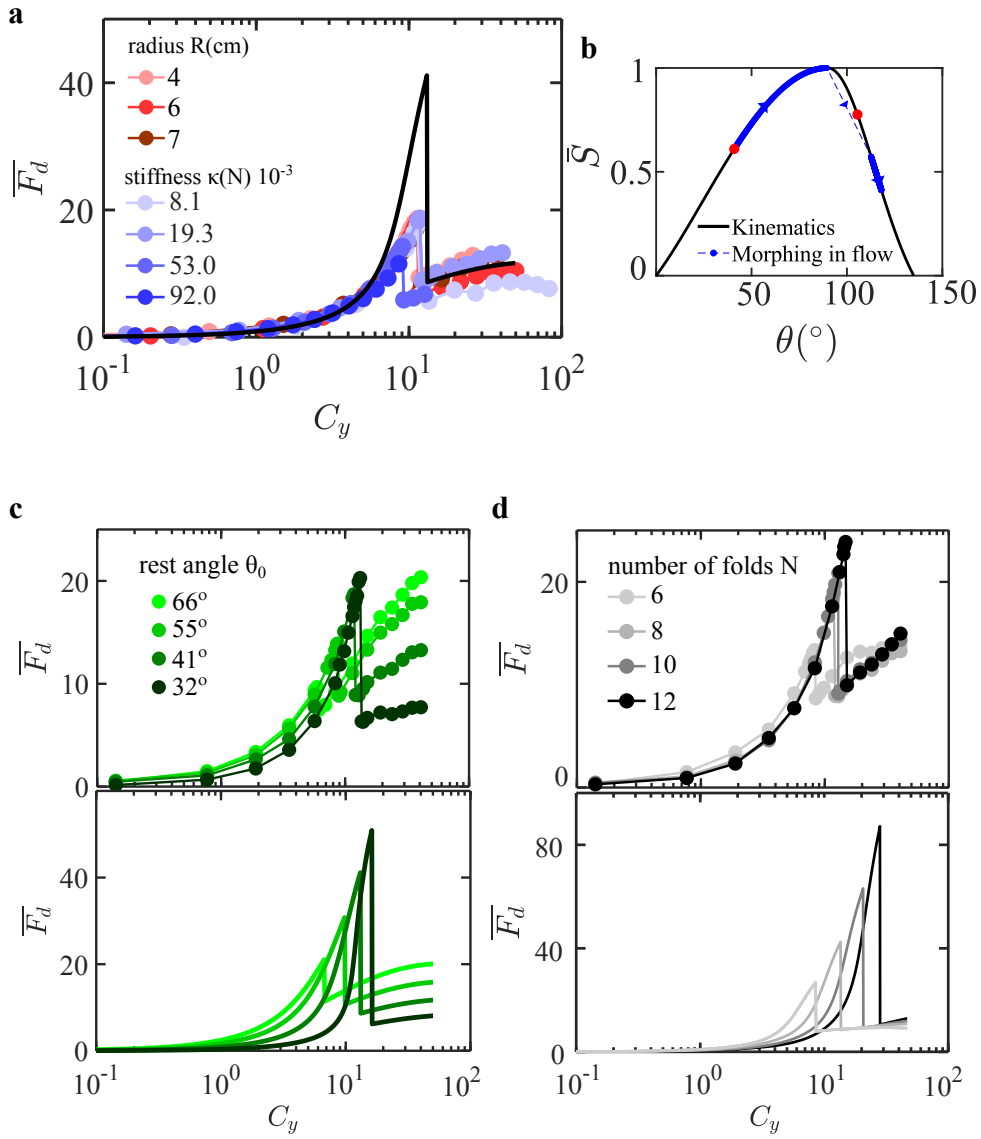

Figure 2.13: Aeroelastic mechanism. Evolution of the dimensionless drag $\overline{F_d} = F_d/\kappa$ as a function of the Cauchy number $C_y = \rho U^2 R^2/\kappa$ (**a**) for origami units with different radius and fold stiffness (while keeping the number of folds $N = 8$ and initial degree of opening θ_0),(**c**) different initial degrees of opening θ_0 (while keeping the same $R = 5$ cm, number of folds $N = 8$ and $\kappa = 19 \times 10^{-3}$ N) and (**d**) for different number of folds N while keeping other parameters fixed. Experimental data are presented with the same markers and colour code as in Fig.2.10 and Fig.2.11, and compared to theoretical predictions (solid curves). For different radii and fold stiffness the theoretical curve is overlaid on the experimental curve in black. For the other parameters, the theoretical curves are displayed in a separate graph for readability, and with the same colour gradient as in experiments. (**b**) The black curve for normalized area $\bar{S}$ depicts the theoretical folding kinematics of the unit with red dots indicating the two stable states. In the presence of the flow, the unit flips to a more closed state which leads to the drag jump (blue curve).

2.3.2 Comparison with experiments

Theoretical drag results are presented in Fig.2.13 in dimensionless form, considering a given rest angle $\theta_0 = 41°$ based on experiments (black solid line). The simplified model successfully captures experimental features, displaying a peak in drag that remains unaffected by the unit's size and fold stiffness, followed by a sudden drop at a critical Cauchy number. Although the model tends to overestimate $F_{d,max}$ and ΔF_d, the quantitative agreement is reasonable, considering that no adjustable parameters were used and the simplifications made. The blue curve in Fig.2.13b depicts the morphing of a Waterbomb base along its folding pathway (black curve) when subjected to a flow with increasing speed U. This evolution is computed using the fluid-elastic model. In the absence of flow, the unit resides in its first stable state (denoted by the red point). As U rises, it unfolds, and upon reaching the flat unstable state ($\bar{S} = 1$), it abruptly snaps towards a state that is more compact than the state $\bar{S}^0$ due to the fluid loading, this state is close to the initial normal area S_0. It is important to note that even though the units with different rest configurations follow the same folding pathway(same evolution of S with θ), they have different potential energy curves (Fig.2.3a). As depicted in the lower panel of Fig.2.13, the model also effectively captures the impact of varying the initial rest angle θ_0 and the number of facets N on drag. A more compact unit exhibits a higher drag peak and jump, along with a higher critical Cauchy number. Similarly, the unit with a higher number of folds tends to have a higher drag peak, jump and critical Cauchy number. This model will be valuable for the inverse design of origami units to achieve the desired drag, as we will discuss in the next section.

2.4 Inverse design approach

2.4.1 Inverse problem

We have characterized how the Waterbomb unit features influence its drag behaviour. We now pose the question: "Can we identify the specific geometrical and mechanical origami parameters that would lead to a targeted drag collapse in a uniform fluid flow?" More specifically, we formulate the inverse problem where the objective is to find the optimal set of parameters (R, κ, θ_0) that will result in a collapse of drag, with a predefined target peak drag force $F^t_{d,max}$ and jump ΔF^t_d value at a critical flow speed U^t_c. To address this, we use the model presented earlier and validated experimentally, which establishes a relationship between the parameters (R, κ, θ_0) and the resulting drag characteristics $(F_{d,max}, \Delta F_d, U_c)$. Even though the model can take into account the influence of the number of folds (N), we did not use it because firstly we lack a deeper understanding of it and secondly the number of folds can be integer numbers only in real life which will reduce the possibilities in the experimental realizations of the units. So, because of practical reasons, we fix $N = 8$ for inverse design.

The optimization is implemented numerically in Matlab using the *trust-region-dogleg* algorithm of fsolve solver. As seen in the inverse design flow chart (Fig.2.14), we start with an initial guess$(R^0, \kappa^0, \theta^0_0)$ and using the model discussed in the previous section to obtain a non-dimensional plot which is then converted to the dimensional plot, the values $\Delta F^0_d, F^0_{d,max}$ and U^0_c are then extracted from the graph and compared to the target drag curve. If the value matches it returns the fabrication values (R, κ, θ_0) else the initial guess is updated (using the trust-region-dogleg algorithm) till the required convergence is achieved. Thus our optimization loop solves the system of equations $F_d - F^t_{d,max} = 0$, $\Delta F_d - \Delta F^t_d = 0$ and $U_c - U^t_c = 0$ with respect to the origami unit's features (R, κ, θ_0). The algorithm finds a single solution, satisfying the constraints by a maximum residual of $O(10^{-19})$ within a hundred iterations.
To validate the inverse design approach, we test our prediction experimentally by fabricating the optimized design and measuring the evolution of its drag with flow speed. While the specific

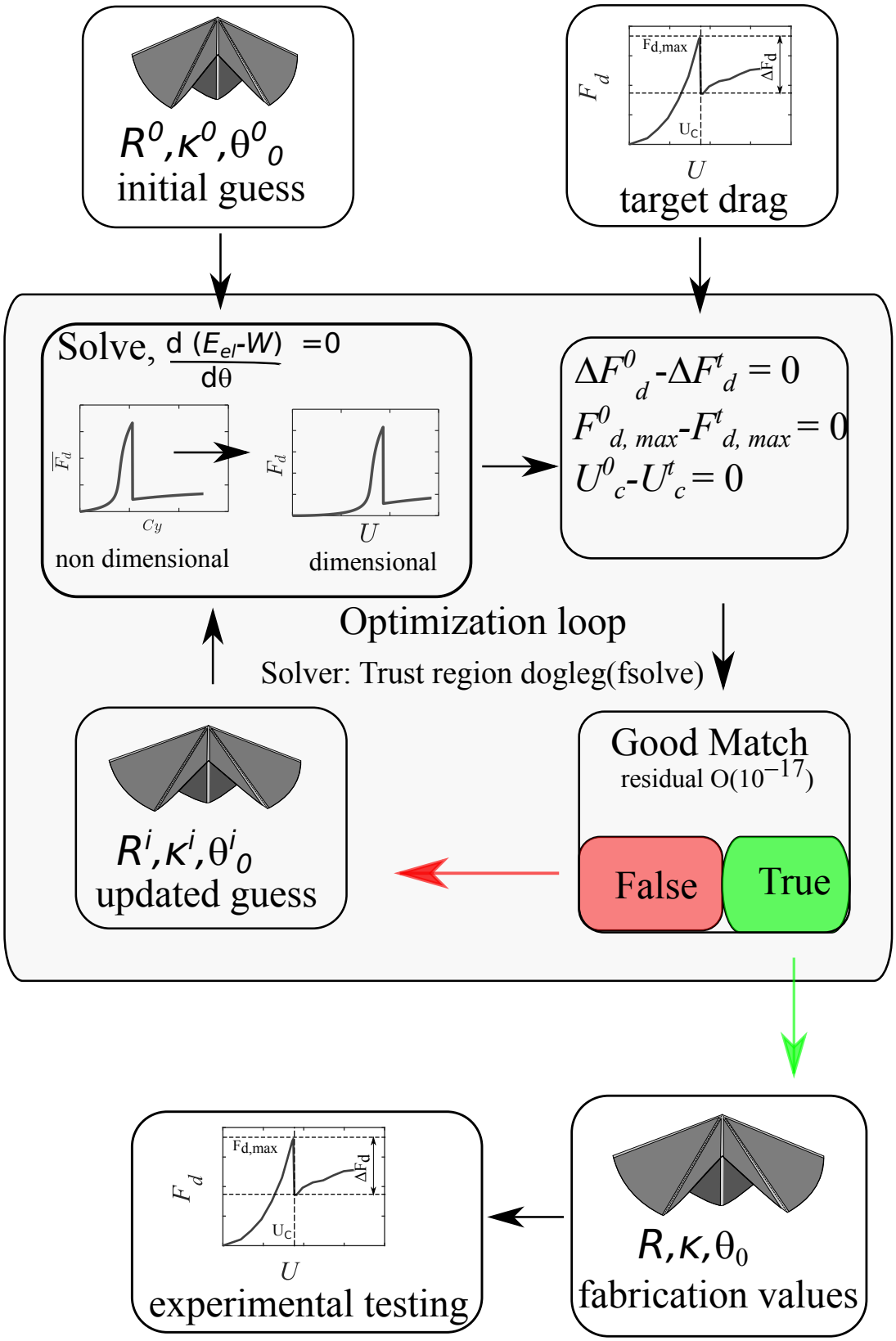

Figure 2.14: Inverse design flow chart. Various steps followed during the process of inverse design. We start with an initial guess (unit's parameters i.e,R, κ and θ_0) and desired target drag features ($F_{d,max}$, ΔF_d and U_c) as the input for the optimization algorithm, which returns us the fabrication values required to get the targeted drag curve.

radius R and rest angle θ_0 can be easily implemented through laser-cutting and an adjustable mount during thermoforming, achieving an arbitrary fold stiffness κ is more challenging. This limitation arises from the finite number of sheet thicknesses available for manufacturing the folds. Let us describe the method used to change the stiffness of the folds before presenting the results from the inverse design approach.

2.4.2 Achieving arbitrary stiffness

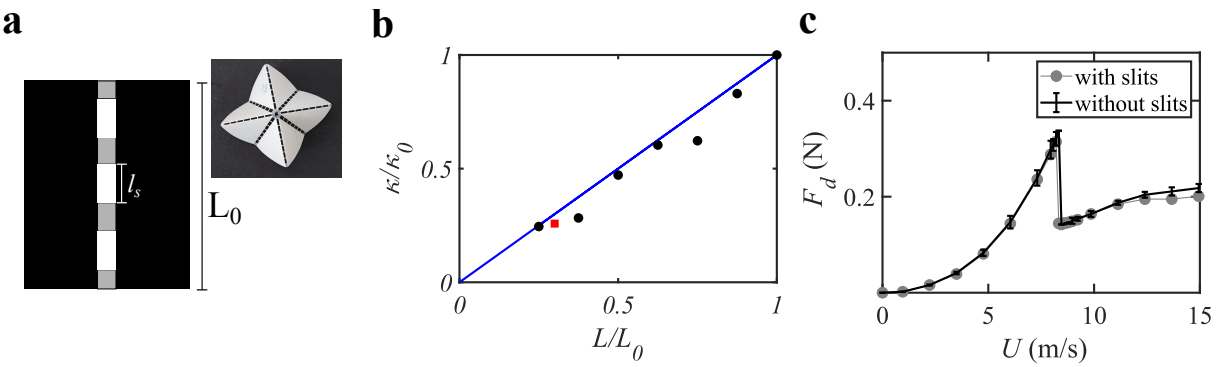

Figure 2.15: (**a**) To adjust fold stiffness, slits of varying length l_s and number n_s, spaced at 5 mm intervals, are incorporated into the crease. (**b**) Stiffness κ of a slitted fold, relative to the uncut fold stiffness κ_0, as a function of the ratio of the remaining material length $L = l_s n_s$ to the total length L_0, for a fold made from a 75 μm sheet. The red point corresponds to a stiffness that mimics an uncut fold made from a 50 μm sheet. (**c**) Evolution of the drag force as a function of the flow velocity for two origami units with the same fold stiffness: one with slitted folds (grey curve, corresponding to the red point in (b)) and the other with unslitted folds (black curve, same curve as in Fig.2.8a). For both specimens, $R = 5$ cm and $\theta_0 = 41°$.

The finite sheet thickness poses a constraint, particularly in the context of the inverse design process requiring arbitrary κ. To address this, we employ a strategy inspired by prior work [95] and introduce slits in the folds. Slits with length $l_s = 5$ mm are evenly distributed along the crease length L_0, and span its width (see Fig.2.15a). Adjusting their number n_s modulates the effective length of the fold $L = L_0 - n_s l_s$, thereby changing its stiffness and facilitating the attainment of diverse κ values. As shown in Fig.2.15b, the stiffness of a slitted fold scales linearly with its effective length, with a 7% deviation from the expected linear relationship. The crease stiffness is associated with the bending of the flexural hinge, so it scales linearly with the length in the transverse direction of bending. This is seen previously in fig.2.6 with linear evolution of torque with the fold angle.

To verify the minimal impact of slits on the interaction of the origami unit with the flow, we conducted experiments with two specimens —one with slitted folds and another with unslitted folds— both having the same stiffness. The stiffness of folds made from a 50 μm thick sheet is replicated using a 75 μm thick sheet with slits corresponding to the red point in Fig.2.15b. As shown in Fig.2.15c, these two specimens exhibit nearly identical drag curves, with only a slight deviation at higher flow velocities. This similarity indicates that the slits have minimal impact on the unit's performance in the flow.

2.4.3 You get what you want!

To demonstrate our ability to control the drag behaviour(or show that our inverse design model works), we create sets of specimens with one parameter gradually changing while keeping the other two fixed. We first vary the targeted critical flow speed for snapping, as $U_c^t = [4, 7, 10]$ m/s,

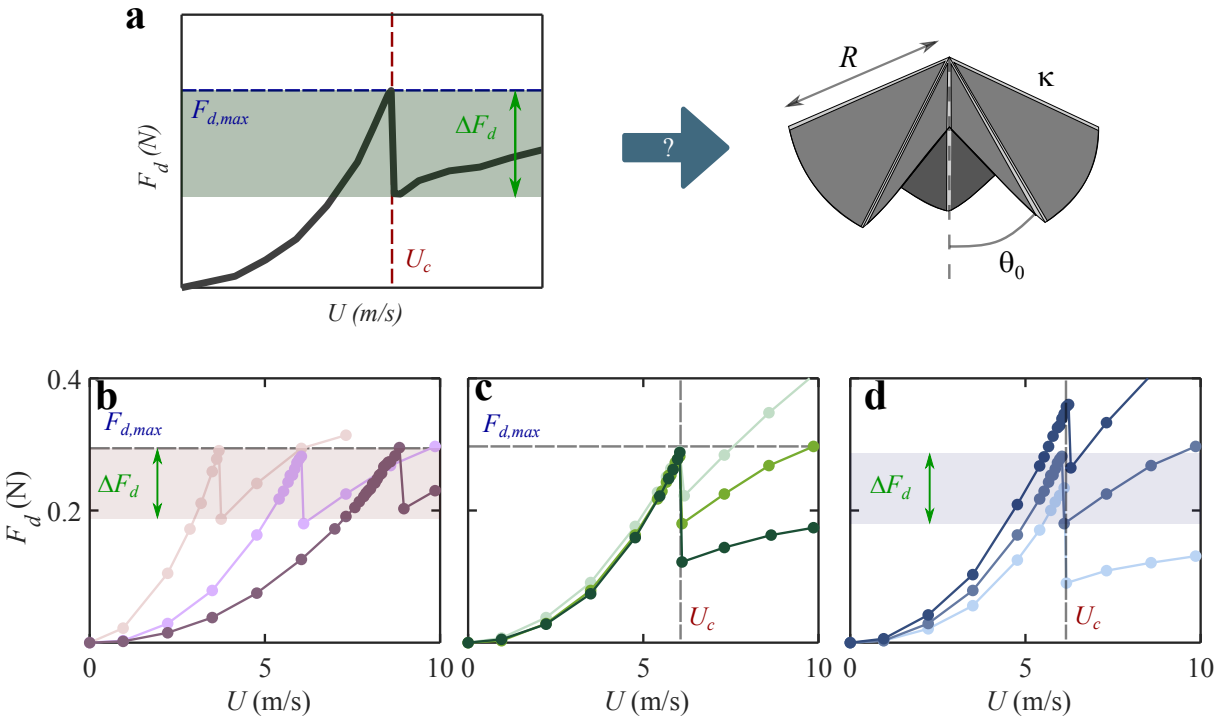

Figure 2.16: Targeting drag collapse features. (**a**) The inverse design approach consists of finding the set of origami structural parameters (R, κ, θ_0) that will lead to a collapse of drag with a targeted maximum before snapping $F_{d,max}$, jump ΔF_d, and occurring at a defined critical flow speed U_c. Evolution of drag with flow speed for physical prototypes of optimized origami designs, which are calculated to produce a selective variation of (**b**) U_c, (**c**) ΔF_d, and (**d**) $F_{d,max}$, while keeping the two remaining features identical. Respective target values of (U_c, ΔF_d, $F_{d,max}$) are indicated in the Table 2.2

.

while prescribing constant peak drag value $F^t_{d,max} = 0.8$ N and jump $\Delta F^t_d = 0.6$ N. The corresponding optimized origami parameters (R, κ, θ_0) are provided in the Table2.2. Consistent with the differences observed earlier in Fig.2.13 between experiments and theory, the experimental realizations exhibit lower values in Fig.2.16b, namely $U_c = [3.7, 6.0, 8.8]$ m/s, $F_{d,max} = 0.29$ N and $\Delta F_d = 0.10$ N. Nevertheless, we successfully achieved a gradual variation in U_c while keeping the other two parameters unchanged. Note that the optimized designs have the same rest angle and fold stiffness, but varying radii, which is consistent with the previous results shown in Fig.2.9a. We indeed demonstrated that $F_{d,max}$ and ΔF_d are size-independent and, therefore, determined by the specific combination of (κ, θ_0). In Fig.2.16c and d, we systematically vary the jump ΔF_d and peak $F_{d,max}$ respectively (target values are reported in the Table2.2). Similarly, although the physical samples have drag quantities below the target values, they still showcased the intended selective variations. Our results confirm the validity of our inverse design approach, but there are limitations to how closely we can match desired drag behaviours.

2.4.4 Discussion on the gap to the target

The differences between the experimental and theoretical curves arise primarily from the theoretical model employed in the optimization procedure. While it accurately captures the impact of origami parameters on drag, it only provides semi-quantitative agreement with the experimental data. Note that deviations between the targeted drag features and those of the resulting optimized design in Fig.2.16 align with differences reported in prior experimental-theoretical comparisons of Fig.2.13. Refining the model, notably using a more realistic representation of

Target values			Corresponding cell parameters		
$F^t_{d,max}$ (N)	U^t_c (m/s)	ΔF^t_d (N)	κ ($\times 10^{-3}$N)	R (cm)	$\theta_0(^\circ)$
0.8	4	0.6	21	4.6	47
0.8	7	0.6	21	6.5	47
0.8	10	0.6	21	11.4	47
0.8	7	0.5	27	6.5	56
0.8	7	0.7	16	6.5	33
0.65	7	0.6	11	5.9	25
0.95	7	0.6	32	7.1	56

Table 2.2: Fabrication parameters produced by the optimization algorithm, for given target drag parameters.

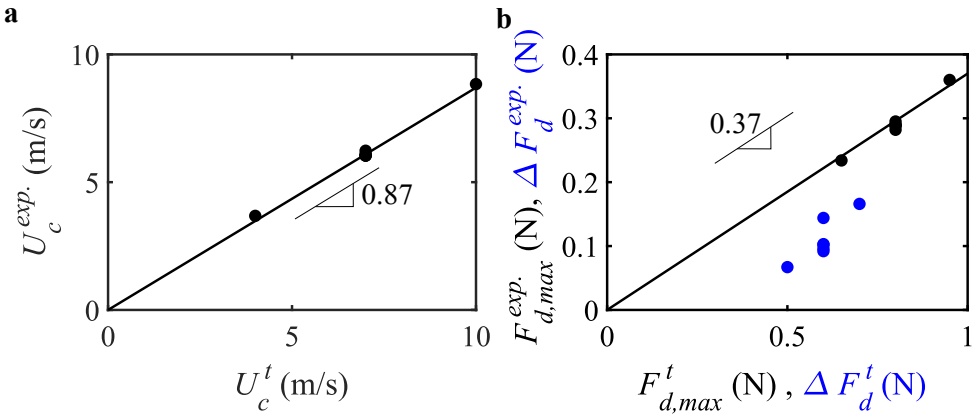

Figure 2.17: Fitting parameters. Relationship between the target values and the values obtained experimentally for (**a**) the critical speed U_c, and (**b**) the drag peak $F_{d,max}$ (in black) and jump ΔF_d (in blue).

the fluid dynamics, is thus expected to produce better quantitative results. To see if the gap between the experiments and the model observed in inverse design is coherent with the previous experiments. We have plotted the theoretical model in fig.2.13a, incorporating the linear fit between the experiments and model from fig.2.17.

Experimentally obtained values of $(F_{d,max}, \Delta F_d, U_c)$ are compared to the target values in Fig.2.17. While the experimental values of U_c are reasonably close to the target ones (see Fig.2.17a), values of $F_{d,max}$ and ΔF_d are notably lower than the target values in Fig.2.17b. However, this disparity is expected given the semi-quantitative agreement between the model and experiments in Fig.2.13, where the model tends to overestimate drag. From the linear relationships depicted in Fig.2.17, we can extract proportionality factors between target values and the ones experimentally obtained, for both flow speed and drag (using $F_{d,max}$ values). In Fig.2.18, the model prediction from Fig.2.13 is re-plotted by re-scaling drag and flow speed using these proportionality factors, showing a good alignment with the experimental data. Deviations observed in the inverse design implementation are thus consistent with the initial level of agreement between experiment and theory. Using a more refined fluid-elastic model is therefore expected to improve the closeness to the target in the inverse design process. Note that the

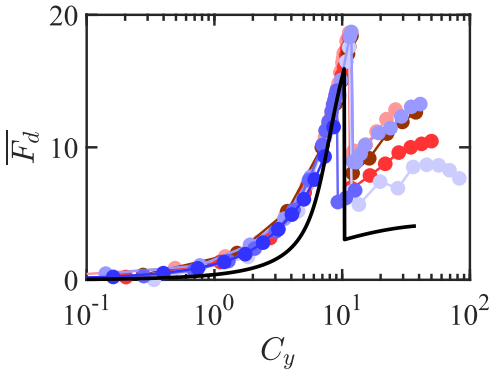

Figure 2.18: Updated model incorporating the linear scaling. Fig.2.13 is reproduced with the theoretical curve modified by re-scaling for flow velocity and drag using the proportionality factors from Fig.2.17.

theoretical ΔF_d does not align satisfactorily with experimental data in Fig.2.18, as the deviation between experimental and target drag value cannot be captured by a single proportionality factor for both $F_{d,max}$ and ΔF_d in Fig.2.17b.

2.4.5 Isolines: Shedding more light on parameters

This section is dedicated to gaining further insight into the influence of fabrication parameters on the drag features. The 3D plots with fold stiffness κ, S(or rest angle θ_0) and radius of the unit R as the respective x, y and z axes depict the isolines with two of the drag features fixed and the third one varying (Fig.2.19). These isolines lie across a line, in a plane or in 3D space depending on which parameters are kept fixed. Two of the isolines are plotted for all the different cases depicted in the figure. For the first case, where $F_{d,max}$ and ΔF_d are fixed, and U_c is allowed to evolve, the isoline obtained is parallel to the R axis (Fig.2.19a). This indicates that to change U_c while other parameters are fixed we only need to change the radius of the unit while keeping stiffness and the rest angle constant. This is the same observation we made about Fig.2.9a and Fig.2.16a. Note, that these isolines can span the whole positive real line and any line parallel to the R axis will be an isoline.

If we change ΔF_d while keeping $F_{d,max}$ and U_c constant the isoline so obtained lies within a plane parallel to the plane spanned by S and κ axes or we can say it is perpendicular to R axis (Fig.2.19b). This indicates that the units which flip at the same critical speed U_c and have

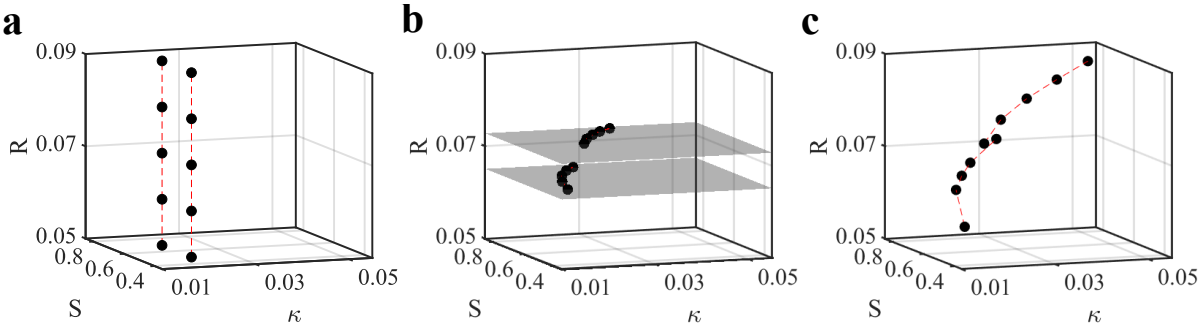

Figure 2.19: Parametric influence on drag features. (**a**) Isoline with constant $F_{d,max}$ and ΔF_d and variable U_c is parallel to the R axis. (**b**) Isoline with constant U_c and $F_{d,max}$ and variable ΔF_d lie within a plane perpendicular to the R axis. (**c**) Isoline with constant U_c and ΔF_d and variable $F_{d,max}$ span the whole 3D space.

the same maximum drag before flipping $F_{d,max}$ but different drag jump ΔF_d can be obtained by changing the stiffness and rest angle while keeping radius fixed. This is similar to the observation we made in the inverse design section Fig.2.16b (2nd,4th and 5th row of the Table2.2). It is important to realize that even though these isolines lie in a plane, any other line in the plane will not correspond to an isoline. That is to say that any random combination of κ and S for a given radius will not have the same U_c and $F_{d,max}$. Also, these isolines cannot span the whole plane as the upper limit on ΔF_d is set by $F_{d,max}$.

To change $F_{d,max}$ while keeping ΔF_d and U_c fixed, we need to vary all the three fabrication parameters as depicted in isolines in Fig.2.19c which span the whole 3D space. Similar to previous cases any random line in 3D space will not be an isoline. These isolines also cannot span the whole space as the lower limit is set by ΔF_d. In this section we saw that to change only U_c we need to vary one parameter namely radius R, to change only ΔF_d we need to change two parameters simultaneously i.e, stiffness κ and rest angle S and to change $F_{d,max}$ we need to change all three fabrication parameters simultaneously.

2.5 Conclusion

In this chapter, we leverage the Waterbomb base's bistability to sharply reduce drag force with flow velocity. A uniform airflow unfolds the origami unit, which, upon reaching a flat state, undergoes a snap-through to a more streamlined shape, causing a sudden collapse of drag. While the use of elastic deformation to mitigate drag increase with flow speed is not novel [26, 30–33, 96], here, a decrease is achieved through significant and abrupt shape changes over a small increment of fluid input load. Importantly, the snap-through is tunable based on the cell radius, fold stiffness, and rest angle, providing control over drag characteristics.

We show that the cell behaviour results from the quasi-static mechanical equilibrium between actuating fluid loading and restoring elastic forces, captured by a Cauchy number. The snap-through occurs at a fixed critical Cauchy number for a given initial degree of opening. The cell rest angle serves as an additional control, influencing both snap-through onset and drag changes. A compact cell reaches the unstable flat state at a higher C_y and transitions to a correspondingly compact state, producing a larger drop in drag. These experimental features are captured by a theoretical fluid-elastic model, portraying the cell as rigid facets with folds acting as elastic hinges, and utilizing an empirical formulation for fluid pressure forces, consistent with prior studies. The model effectively accounts for the influence of cell structural parameters on drag, demonstrating reasonable predictiveness despite a tendency to overestimate drag. However, such discrepancies are expected, considering the absence of adjustable parameters and the simplified representation of fluid dynamics, which notably does not consider the object's retroaction on the flow.

The modelling framework provides the system equations to guide inverse design, intending to identify the combination of structural parameters leading to a targeted drag collapse. Our implementation showcases an advanced level of control, allowing selective adjustment of key drag features: namely, the peak drag before snapping, the drag drop, and the critical flow speed at which it occurs. Currently, quantitative predictability is contingent on the model's accuracy. Improved closeness to the target is anticipated with more refined fluid-elastic models, positioning this work as promising proof of concept. It illustrates the potential of origami as a platform for programming drag-vs-speed behaviour.

This programmability holds value for self-protection strategies, mitigating excessive aerodynamic loads beyond a predetermined threshold. Force transitions above a tunable critical flow velocity could also serve as a velocity threshold detector. The switch-like response of the Waterbomb base also holds the potential for fluidic control in a channel, for example, acting as a relief valve. It would obstruct conduct as it deploys and discharges the fluid beyond a predetermined pressure

level, limiting pressure built up. In all these applications, morphing is driven aeroelastically, enabling the component to autonomously respond to the local environment, and eliminating the need for additional sensing and control systems. Such passive mechanisms allow for a more streamlined structural design of the aerodynamic control surface.

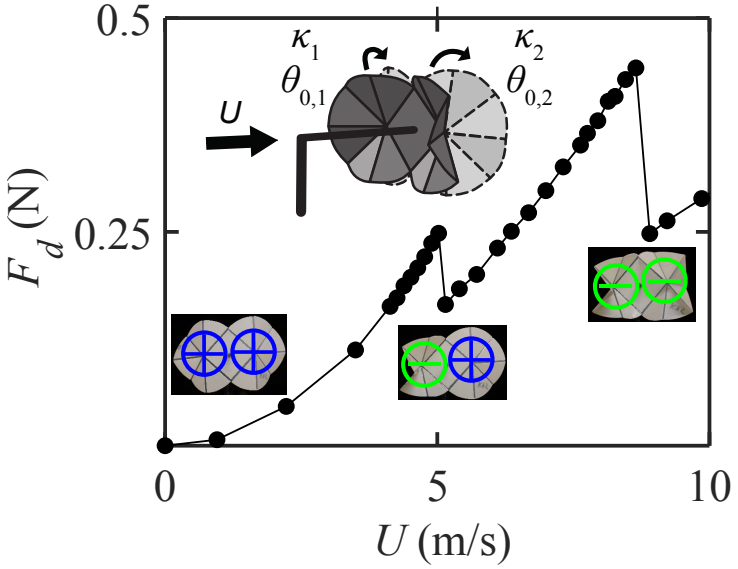

Figure 2.20: Leveraging multistability for a double drag collapse. A multistable origami structure is formed through the assembly of two Waterbomb units, with different fold stiffness $\kappa_1 = 19 \times 10^{-3}$ N and $\kappa_2 = 53 \times 10^{-3}$ N and rest angle $\theta_{0,1} = 56°$ and $\theta_{0,2} = 71°$, and the same radius $R = 5$ cm (inset). The successive snap-throughs lead to sequential drag collapses when exposed to a uniform flow with increasing speed. Different states of the multistable assembly of the Waterbomb units are indicated on the unit with a + and -. Both the units are in the first stable state(++), Unit of lower stiffness in a second stable state(-) and higher stiffness in the first stable state(+), Both the units are in their second stable state(–).

An advantage of origami is the ability to easily combine multiple bistable elements to produce multistable structures [74, 97–99]. An example is shown in Fig.2.20, featuring a chain made of two Waterbomb cells with the same size and different rest angles and fold stiffness. It produces two successive sharp transitions in the drag force. With sufficient spatial separation, each unit is expected to have its independent flow velocity threshold initiating snap-through. Other configurations might, however, lead to interactions between cells through external flow, resulting in a more complex collective response, as observed in fluidic cellular origami (albeit for internal pressurization) [97]. Alternatively, if cells share facets, they can also communicate the mechanical state of one unit to its neighbour, forming logic elements [100]. This has the potential to generate more complex snapping sequences and subsequent drag evolution with flow speed for advanced adaptive functionalities.

Chapter 3

Passive flow control in a channel

Fun fact: The idea of a control valve dates back to the bronze plug cocks utilized by the Romans in their aqueduct systems. The moving-stem (automatic) valve concept was pioneered by James Watt in the late 18^{th} century, as part of his fly-ball governor designed to regulate the speed of his steam engine. The evolution of control valves continued alongside the advancements of the steam age throughout the 19^{th} century.

In this chapter, we examined the use of a Waterbomb unit as a valve. We constructed a setup integrating the origami unit into a pipe, allowing us to regulate pressure loss across the unit with varying flow rates. The opening phase of the Waterbomb unit increases blockage in the pipe, building up pressure, followed by a sudden release via snap-through that causes discontinuity and results in a slower pressure buildup with a further increase in flow rate. Unlike the previous chapter, this study focuses on the unit's performance under confinement, which introduces a significant blockage effect. Variations in structural parameters under confinement led to differences from the previous results, which were addressed by modelling the confinement's effect as an effective speed experienced by the unit. Incorporating a non-dimensional pressure drop and a modified Cauchy number based on this effective speed allowed for a rescaling in the model. Tests on units in series were validated using a nonlinear resistance toy model, which also explored the behaviour of units in parallel. This model, which was challenging to test experimentally, suggests that parallel units could function as pressure relief valves, leading to a sudden and amplified flow speed change. The resistance of the units can be adjusted to fine-tune this effect.

Contents

3.1 Introduction

A valve is a component in a piping system that regulates, directs or controls the flow. This is done by opening, closing or partially obstructing the pipe. They can be found almost everywhere spanning from industries to the tap in our houses. The two broader categories of valves include the one that can be controlled manually or by some actuator called active valves and the second type which can be driven by flow parameters like pressure or flow speed are called passive valves. A detailed review of the microvalves can be found in the review by K. W Oh and C.H Ahn[101]. Passive valves are gaining popularity because of their ability to avoid external actuators, so they tend to make the system autonomous. This makes the design easier to implement and more adaptive. Valves are characterized by the relationship between pressure difference across it and flow rate, tuning which can be useful in various fields. In soft robotics non-linear soft valves with mechanical and fluidic hysteresis can be used to activate and reprogram up to five actuators in sequences[102]. A multimodal pneumatic soft valve capable of passive resilient reactions, triggered by faults, can be used to prevent or isolate damage in soft robots[103].

The mechanical passive valve can be made using flaps, membranes, spherical balls or mobile structures. A few examples of such passive valves are depicted in Fig.3.1. Fig.3.1a depicts such

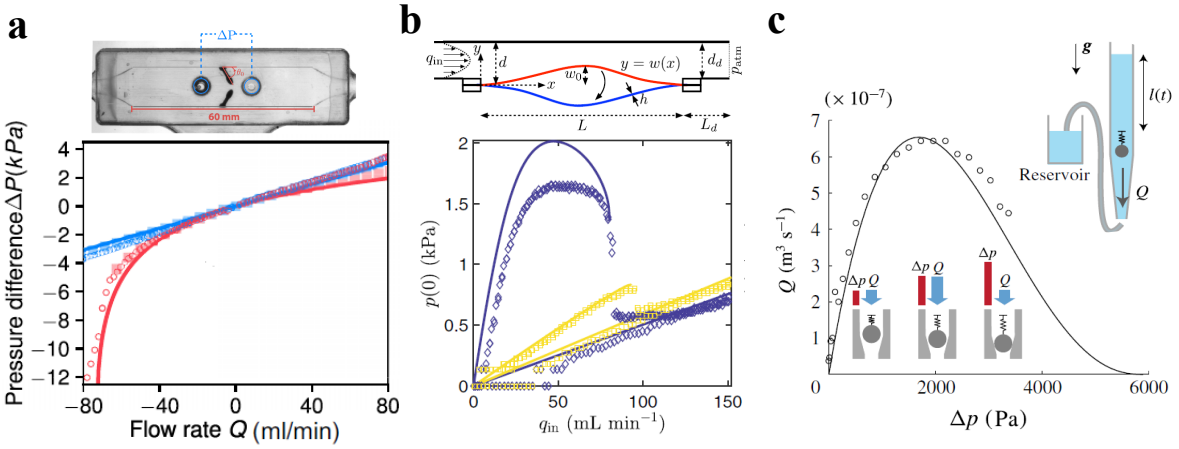

Figure 3.1: Different kind of passive valves and their flow characteristics[41, 104, 105]. (**a**) Deformable membrane as a Valve acting as a diode allowing flow in one direction. The soft valve (red) is compared with the rigid one (blue). (**b**) Arch utilizing bistability via snap-through deformation to attain non-monotonic flow regulation. The curves are for different blocking parameters (w_0/d) with yellow being a lower value and blue with a higher value. (**c**) A sphere attached to a spring for passive flow regulation.

a passive valve and its corresponding pressure curve for changing flow rate([104]). In the study, two membranes were attached to the opposite walls of the channel such that they could completely block the channel by coming in contact with each other or allow maximum flow by moving close to their respective walls. This geometry allowed them to act as semipermeable membranes, by blocking the channel in one direction and opening it up in another direction. Introducing bistability to the plate can even be used to achieve a non-monotonic pressure flow curve by changing the hydraulic conductivity of the channel as depicted in Fig.3.1b. On increasing the flow speed, the initially confined channel suddenly opens up beyond a critical speed of snapping of the strip leading to a sudden pressure drop([41]). This flexible arch when used in parallel with a rigid channel can act as a passive fluid fuse by shortcircuiting the rigid channel above a critical flow rate. Another way to regulate the flow can be to add a rigid obstruction (spherical ball) in the pipe and modify the blockage with the help of a spring as shown in Fig.3.1c([105]). In these deformable structures, the balance between the fluid forces and elastic forces governs

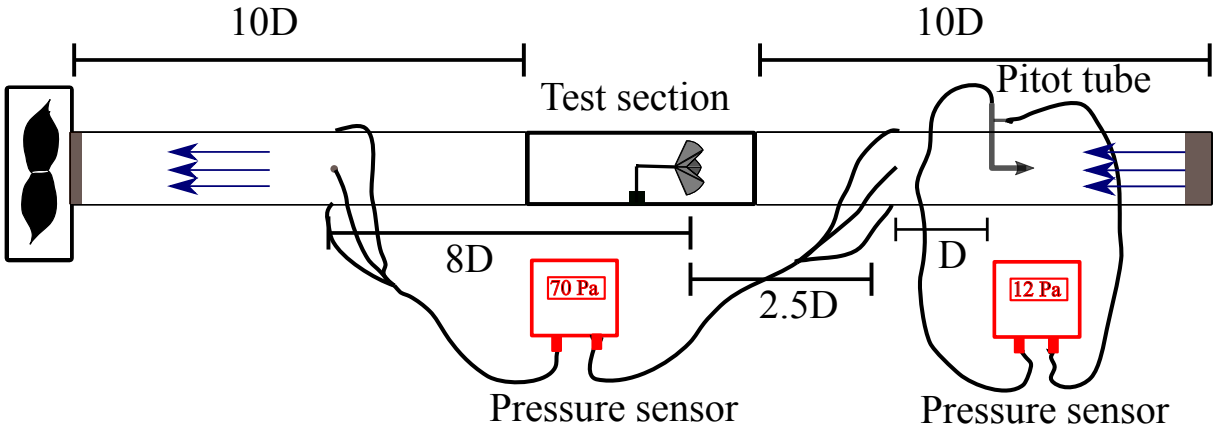

Figure 3.2: Experimental setup for the study of the Waterbomb unit indicating various components. Not to scale.

the deformation and thus the flow regulation. Most of the studies for flow regulation using deformable structures are concerned with flow control in narrow space([49, 106–108]), making electronic components ([91, 109, 110]) and pneumatic actuation([83, 111–114]). To our knowledge, origami structures have not been studied for valve applications. It is a good candidate to get non-linear pressure flow rate behaviour because of its own non-linear mechanical properties. In this chapter, we demonstrate the utility of the passive deformation of the Waterbomb unit detailed in the previous chapter in response to fluid loading as a passive flow regulator or as a pressure relief valve at moderate to high Reynolds number. The flow regime is not the same as the applications of origami discussed so far but the concept can be implemented at a low Reynolds number as well, which may show different behaviour than seen here.

3.2 Construction of tunnel

To study the effect of confinement on the Waterbomb unit, an open wind tunnel with a circular cross-section is constructed. Let us discuss various components of the tunnel and their utility.

3.2.1 Constitution of wind tunnel and characterization of the flow

The tunnel is 310 cm long and has a circular crosssection of the inner diameter of $D = 12.4$cm. It is divided into three parts, the inlet section of length $10D$, with a flow straightener at the entrance, a removable test section to mount the origami unit/obstructing object of length $5D$ followed by another $10D$ section which allows the flow to develop again. A centrifugal fan is used in the suction mode in order to generate the flow from right to left as depicted in Fig.3.2. The fan speed is regulated by changing the rotation frequency with the help of a variable frequency drive giving the inlet speed from 2 to 8m/s. As the fan operated at the same frequency may give rise to different flow speeds depending on the amount of obstruction, thus a pitot-static probe (coefficient 1.01) is placed $3.5D$ upstream of the obstruction aligned with the central axis of the pipe in order to measure the instantaneous inlet flow speed. Four point pressure taps evenly distributed along the circumference of the tube are placed 2.5D upstream and 8D downstream of the plane of the Origami unit and connected to a differential pressure sensor in order to measure the pressure difference between the two cross sections. The use of various components is elaborated below.

Pitot-static probe: The Pitot-static probe also called the pitot tube determines local velocity by assessing the pressure difference in combination with the Bernoulli equation. It is

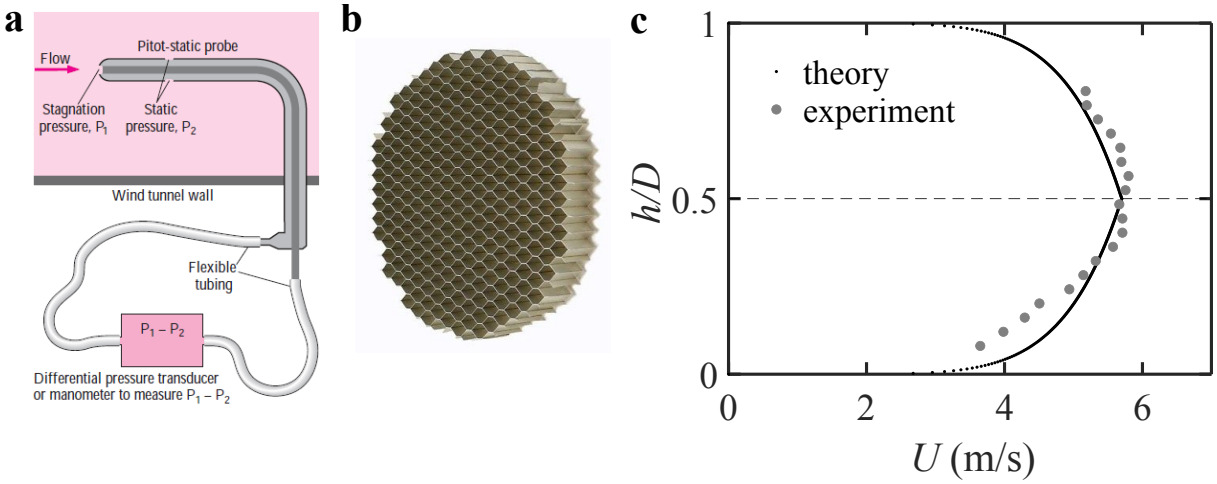

Figure 3.3: (**a**) Schematic of pitot tube used to measure the inlet velocity. (**b**) Honeycomb flow straightener used at the inlet to reduce flow profile development length. (**c**) The average flow profile across the pipe was measured via a pitot tube along the diameter compared with the theoretical flow profile for turbulent flow.

composed of a slender, double-walled tube (see Fig.3.3a) that is aligned with the airflow and connected to a differential pressure gauge. The inner tube is fully exposed to the flow at the front, enabling it to measure the stagnation pressure at that point (point 1). The outer tube is sealed at the front but has openings on its sides (point 2), which allow it to measure the static pressure. For incompressible flow with sufficiently high speeds—where frictional effects between points 1 and 2 are minimal—the Bernoulli equation is applicable and can be expressed as follows.

$$\frac{P_1}{\rho g} + \frac{V_1^2}{2g} = \frac{P_2}{\rho g} + \frac{V_2^2}{2g} \tag{3.1}$$

As $V_1 = 0$ because of stagnation conditions, the flow velocity becomes

$$V = \sqrt{\frac{2(P_1 - P_2)}{\rho}} \tag{3.2}$$

For practical purposes, the equation of the flow speed is multiplied by a pitot coefficient which depends on the geometry of the pitot tube. In our case, it was 1.01 as mentioned before.

Flow straightener: A flow straightener significantly minimizes disturbances in a flow (Fig.3.3b). As a result, these devices enable shorter upstream straight lengths and enhance measurement accuracy during flow measurement.

Centrifugal fan: Centrifugal fans harness the kinetic energy of their impellers to drive the air stream, displacing air radially and usually changing its direction by 90°. These fans operate as constant-volume devices, meaning they maintain a relatively steady volume of air at a fixed fan speed, rather than a constant mass. As static pressure increases, the volume flow rate decreases when the fan speed remains constant. This relationship, known as the fan curve, is crucial in selecting the appropriate fan for a given setup.

The area from the pipe inlet to the point where the boundary layer converges at the centerline is known as the hydrodynamic entrance region, and the distance of this area is referred to as the hydrodynamic entry length L_h. Flow within this entrance region is termed hydrodynamically developing flow, as it is the zone where the velocity profile is still forming. Beyond this region, where the velocity profile is fully developed and remains consistent, is called the hydrodynamically fully developed region. The entry length depends on the Reynolds number;

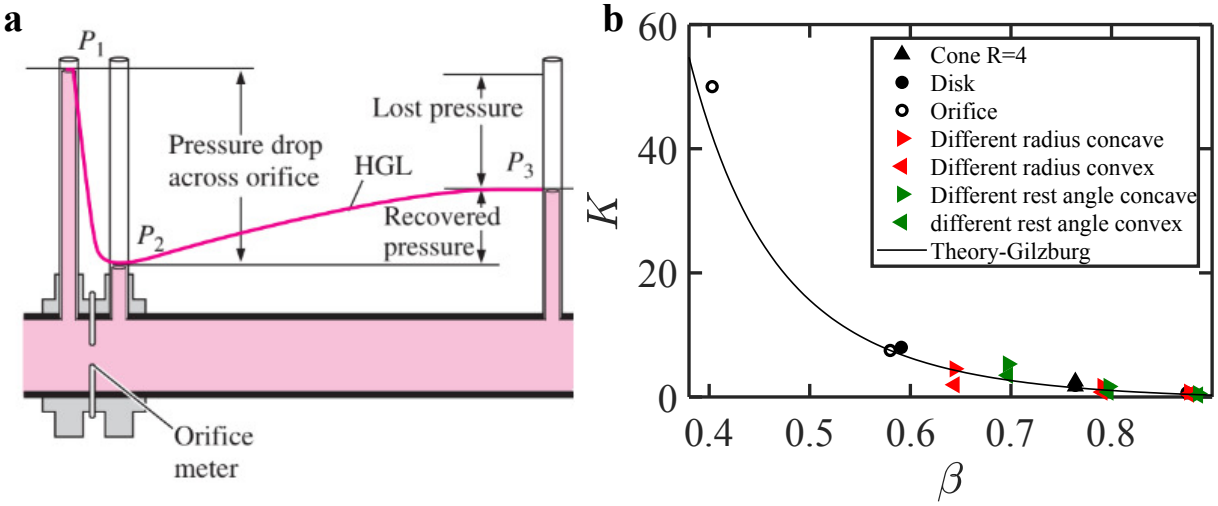

Figure 3.4: (**a**) Pressure variation along the flow section in the presence of an orifice plate. (**b**) The pressure drop coefficient for various experiments compared with the theoretical curve(black line).

however, for practical purposes in turbulent flows, it is often approximated as $10D$. Additionally, there is an exit length, which is significantly shorter than the entry length. In our setup, by introducing the flow straightener we tried to reduce the entry length to have a fully developed turbulent flow. Fig.3.3c, depicts the average velocity profile (average over 30s) measured along the diameter of the pipe by moving the pitot tube in the vertical direction. The vertical distance measured from the top (h) is non-dimensionalized using the diameter of the pipe (D). The flow profile does not fully align with the theoretical profile found using empirical 1/7 power law[115], which is $u/U_c = (2h/D)^{1/7}$. Where U_c is the maximum flow velocity (we use 5.7 m/s from the experimental data), h is the vertical location of the point of measurement of the speed and D is the pipe diameter. It was not possible to have the flow profile of the whole tube as the length of the pitot tube was less than the diameter of the pipe.

3.2.2 Pressure difference across a constriction

In the presence of a sudden change in the flow area in the tube, a considerable amount of swirl forms, which leads to a significant amount of pressure loss. Fig.3.4a, shows the variation of pressure along a flow section with an orifice plate measured with piezometer tubes. An orifice disk is a disk which can fit in the pipe normally to the flow with a hole in the centre as depicted in the 2D view in Fig.3.4a. We see that the pressure drops to the lowest value at P_2, this point is called the vena contracta. After that, the pressure again increases to reach a constant value at P_3. In the process, some pressure is permanently lost. Orifice flow meters which are used to calculate the flow velocity can measure pressure at different locations by putting pressure taps. They differ in their upstream and downstream location. Most of the conventional flow meters use downstream pressure taps closer to vena contracta in order to get maximum pressure difference, which is not possible in our case. As the Origami unit changes shape and thus the location of its vena contracta will change as well. This makes it difficult to put pressure taps very close to the origami downstream, thus to avoid any pressure change because of a shift in the location of vena contracta, pressure taps are placed where the upstream and downstream pressure are constant i.e., $2.5D$ and $8D$ upstream and downstream respectively. This is also called full-flow or pipe taps.

The general formula for the total pressure drop across an orifice plate can be expressed using

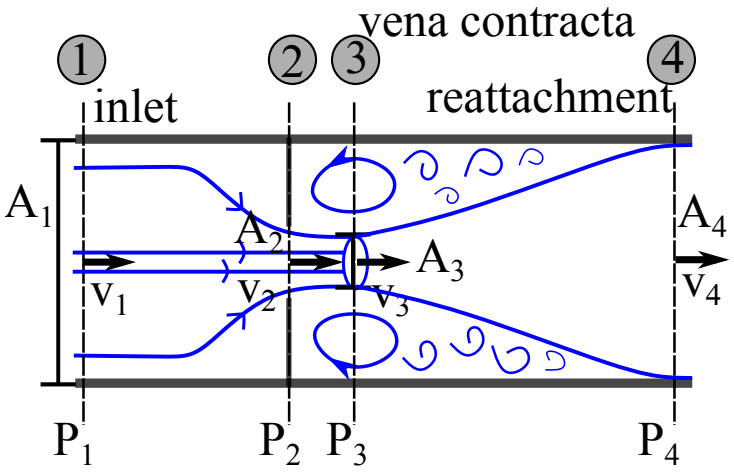

Figure 3.5: 2D schematic to show flow across the orifice device.

the expression from the previous studies for sharp edge orifice as [116, 117] :

$$P_1 - P_4 = (K_{1,4})_2(\frac{\rho v_2^2}{2}) \tag{3.3}$$

Where $(K_{1,4})_2$ is called the pressure loss coefficient from 1 to 4 calculated based on the velocity at 2 (see Fig.3.5). Where the pressure loss between the section 1 and 3 is calculated using the continuity and the energy equation and the pressure loss between sections 3 and 4 is calculated by the Carnot-Borda equation of expansion of the jet. These two loss coefficients were added to get the net loss coefficient.

It has been shown that the coefficient can be approximated by the equation given by Idel'chik and Ginzburg:

$$(K_{1,4})_2 = (1-\beta^2)^2 + \frac{1}{2}(1-\beta^2) + 1.41\sqrt{(1-\beta^2)}(1-\beta^2) \tag{3.4}$$

Which only depends on the geometrical parameter of the orifice meter. Different shapes and geometries were mounted in the wind tunnel to test if they aligned with theoretical eqn.3.4 (Fig.3.4b)[116, 118]. Firstly, we mounted orifice plates with inner diameters of 7.2cm and 5cm and a thickness of 3mm, made by laser cutting acrylic sheet. Secondly, we mounted disks of radius $R = [4, 5, 5.5]$cm. Thirdly, we mounted three rigid origami units fabricated with three different rest angles (to modify the blockage), mounted with concave as well as convex orientation facing the flow. They were fabricated with thick mylar sheets. Finally, we mounted a 3D printed conical structure, with an apex angle of 30°, and a slant height of 5cm, with 2mm thickness, both in concave and convex orientation. All the obstructions were placed coaxially to the pipe of the wind tunnel. Fig.3.4b, depicts the pressure drop coefficient for different blockages identified as blockage ratio $\beta = \sqrt{\text{Open area/Area of pipe}}$. The open area is the normal area which is not blocked by the obstruction. In the case of orifice plates, it will be the $\pi/4D^2$, with D orifice diameter, for disk it will be Area of pipe $-\pi R^2$, with R being the radius of the disk. Similarly, it can be defined for other shapes. We observe that the loss coefficient increases with the amount of blockage and tends to follow the theoretical curve. The experiments with origami and cones demonstrate that the pressure drop coefficient is higher when the concave side faces the flow which can be seen in higher values of pressure drop coefficient for triangles pointing rightwards. However, they are still close to each other, which indicates that the shape does not have a significant influence on the pressure loss coefficient.

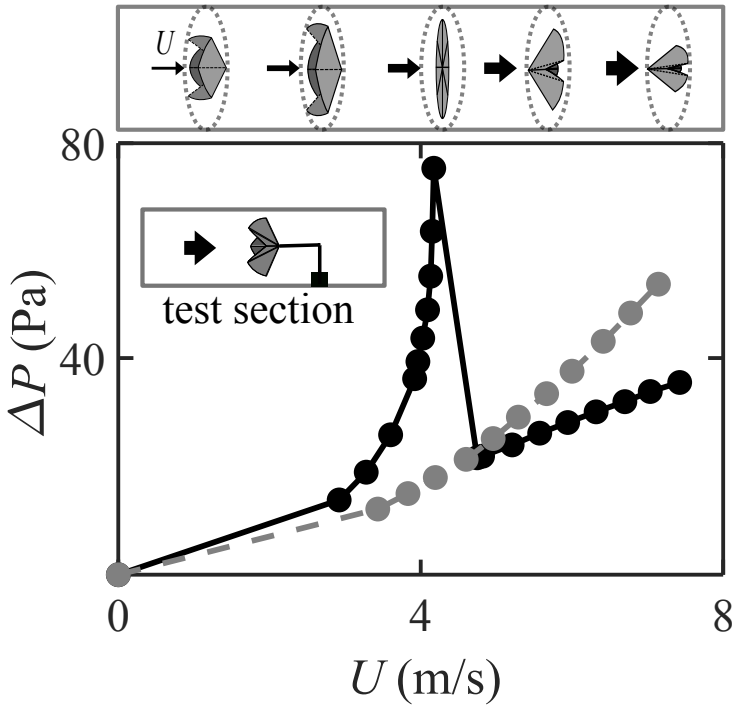

Figure 3.6: (**a**) Pressure vs velocity plot for the origami unit ($R = 5$ cm, $\kappa = 53 \times 10^{-3}$ N, $N = 8$ and $\theta_0 = 41°$) in increasing flow rate. The inset depicts the unit mounted with a concave side facing the flow in the test section.

3.3 Pressure drop across a confined Origami unit

The Waterbomb units for this study were fabricated using the layer superposition fabrication method explained in detail in the previous chapter. Let us discuss a typical experiment for the unit.

3.3.1 Experimental methods and typical curve

The Waterbomb origami unit is mounted coaxially with the pipe with a concave side facing the flow in the removable test section with the help of a 3D-printed curved structure and a metallic elbow structure. The flow speed is increased from 1m/s to 8 m/s in small steps. The differential pressure drop is measured with the help of pipe taps. Pressure values across the taps and pitot tube are averaged over 30 seconds for each speed imposed. The origamis of radius $R = [4, 4.5, 5, 5.5]$ cm, fold rigidity $\kappa = [19, 53, 92, 129] \times 10^{-3}$N with $N = 8$ folds and rest angle $\theta_0 = 41°$ were used during this study. Thus the maximum blockage percentage (origami radius/pipe radius) varies from 64% to 89% for minimum and maximum radius respectively. As the blockage is high, we expect to have a significant blockage effect. As depicted in Fig.3.6, on increasing the flow speed the concave side flow facing unit opens up leading to increased pressure difference(black curve) compared to rigid origami with the same rest angle in grey, further, it reaches a flat unstable state from which it flips towards the second stable state, which leads to discontinuity in the pressure measurement. The pressure post snapping increases at a slower speed because of the reduction in normal area with increasing speed. We did not capture the normal area because it was not possible to mount a camera upstream/downstream without disturbing the flow. Note: the sudden change in the obstruction area post-snapping leads to a sudden rise in flow speed as observed in the gap between the speed at maximum pressure and post-snapped state. This is inherent to the setup and can be understood by considering that the fan gives a higher flow rate for low obstruction at the same rotation frequency. Thus, a

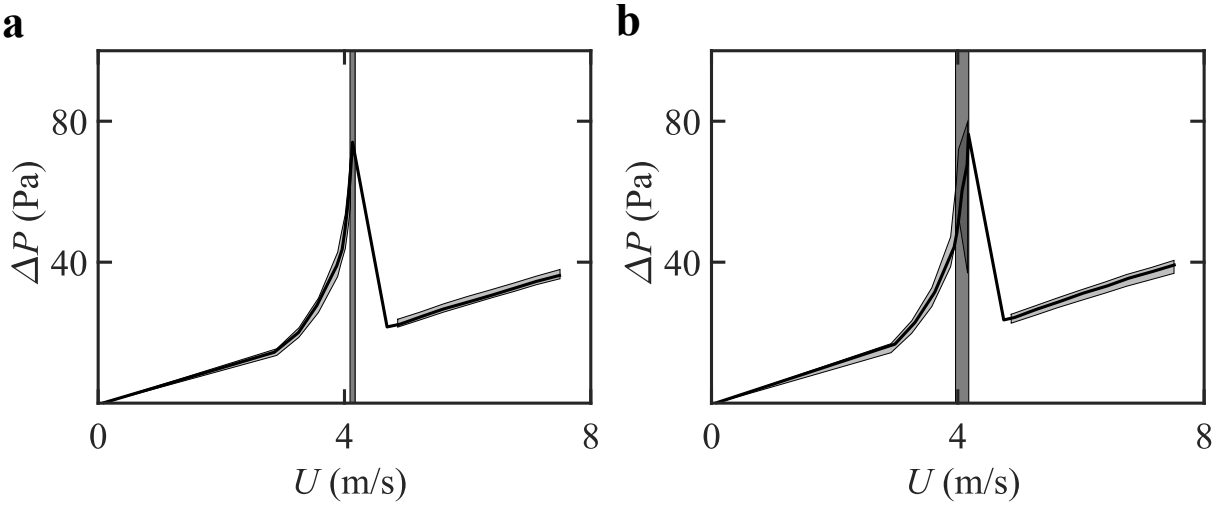

Figure 3.7: Evolution of pressure difference with flow speed U, for origami specimens with $R = 5$ cm, $\kappa = 53 \times 10^{-3}$ N and $\theta_0 = 41°$. (**a**) The same unit is tested three times, with re-annealing between each test. (**b**) Experiments for five similarly fabricated units. The grey region depicts the standard deviation at different points and the strip indicates the standard deviation on the critical speed.

fully open unit will have a lower flow rate at the same fan rotation frequency compared to a post-snapped unit at the same frequency.

3.3.2 Repeatability of the experiments

To test the repeatability of the experiments and of the fabrication process, we repeated experiments for five distinct units fabricated with identical parameters $R = 5$ cm, $\kappa = 53 \times 10^{-3}$ N, $N = 8$ and $\theta_0 = 41°$. Fig.3.7b presents the mean values for the pressure drop, with the grey region corresponding to the standard deviation. The grey strip denotes the variation in the critical speed for snap-through U_c. The associated relative errors are of the order of 2% and 3%, respectively for ΔP and U_c.

We also conducted three repetitions of the experiments using the same unit. Before each test, the unit underwent an hour of re-annealing in the oven, followed by an additional hour of cooling at room temperature to ensure a consistent initial cell configuration. The mean values and standard deviations for the measurements are depicted in Fig.3.7a. The relative error in both plots is within 4%. The low error in both graphs indicates that the measurements are reproducible.

3.3.3 Parametric variation

In this study, we will vary one of the parameters of the unit while keeping the other three parameters fixed. This study is restricted to the variation of radius and crease stiffness of the unit. The first one allows us to change the amount of maximum blockage whereas the second one allows us to retain the maximum blockage while changing the potential energy of the unit. These two were sufficient to understand the effect of blockage without adding complexity that comes with other parameters N and θ_0 (i.e., modifying potential energy curve and kinematics) so we ended up restricting the investigation to these two. The parameters have a similar influence as in the previous study on the drag, but deviations are observed due to confined geometry, which is discussed as follows:

- **Radius**: In this parametric study we changed the radius of the unit from 4cm to 5.5cm

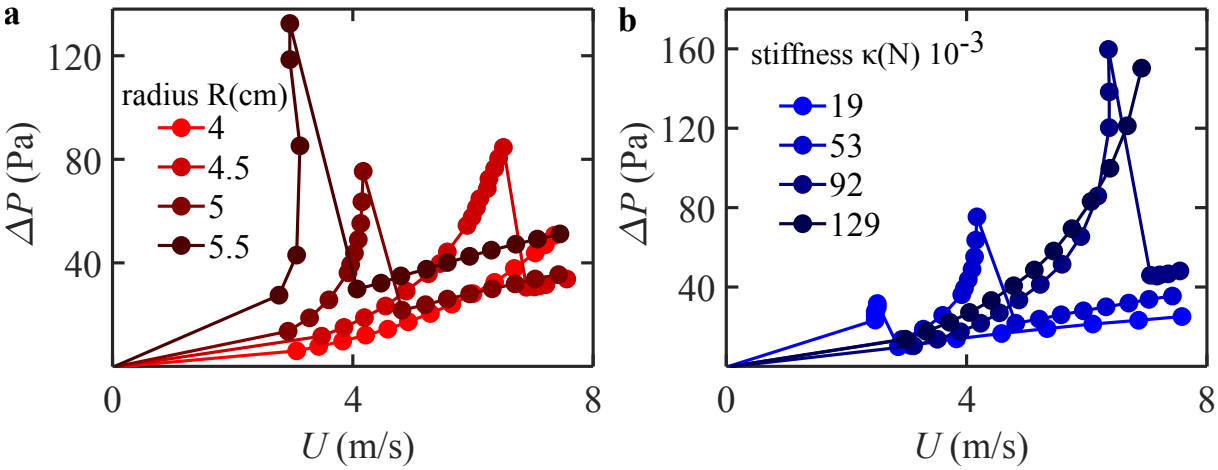

Figure 3.8: Pressure drop across the Waterbomb unit as a function of upstream flow speed for units with (**a**) increasing radius/blockage effect and (**b**) increasing fold stiffness. While changing one parameter others are kept constant to $R = 5$cm, $\kappa = 53 \times 10^{-3}$ N, $N = 8$ and $\theta_0 = 41°$.

while keeping the other parameters fixed as $\kappa = 53 \times 10^{-3}$ N, $N = 8$ and $\theta_0 = 41°$ (Fig.3.8a). We see that starting from a given rest angle the unit with a higher radius experiences higher fluid forces at a given flow rate and thus tends to flip at a lower flow speed. This trend is similar to the one observed in the drag force measurements though the maximum pressure achieved is not the same for units with different radii. This is attributed to the confinement, the inlet velocity seen by the unit changes with the amount of area blocked by the unit.

- **Stiffness**: For this study, we changed the fold stiffness of the unit while keeping $R = 5$cm, $N = 8$ and $\theta_0 = 41°$ fixed (Fig.3.8b). Increasing the stiffness requires higher fluid loading to overcome the potential energy barrier for the unit to flip. Thus the stiffer unit flips at a higher flow speed. As the maximum blockage imparted by the unit is the same thus blockage has the same effect on all the units.

The behaviour of the Waterbomb unit in the confined flow is governed by the competition between the fluid forces and the elastic forces. Thus, we define a non-dimensional Cauchy number, similar to the previous chapter but in spite of using the upstream velocity, we use the effective velocity experienced by the unit. To find this velocity we use mass conservation assuming that the blockage is due to a disk of the same radius as origami in a flat state i.e $v_l = UA_p/(A_p - S)$, where v_l is local flow speed (effective velocity) seen by the origami unit, U is upstream velocity, A_p and S are the normal area of the pipe and the origami respectively. Thus the Cauchy number is modified to take into account the effect of blockage by using the local velocity experienced by the unit. The velocity thus found was used to calculate the effective Cauchy number $C_y^* = \rho v_l^2 R^2/\kappa$. Similarly, the pressure is also non-dimensionalized using the area of the flat origami unit and the fold stiffness as $\bar{\Delta P} = P\pi R^2/\kappa$. The rescaling is contrasted in Fig.3.9 with the non dimensional Cauchy number obtained without the use of effective flow speed (or using inlet velocity measured by the pitot tube). The better collapse of curve indicates the need to introduce the effective flow speed. The rescaling works well except for the case of big origami. The units with different stiffness had similar effects of confinement as their maximum area is the same and the confinement effect for units with lower radius is taken into consideration by introducing effective velocity. We believe this leads to a good rescaling. The biggest unit is very close to the wall, which leads to additional effects that could not be accounted for by the effective velocity, like the modification of the wall boundary layer leading to vortex shedding near the wall[119].

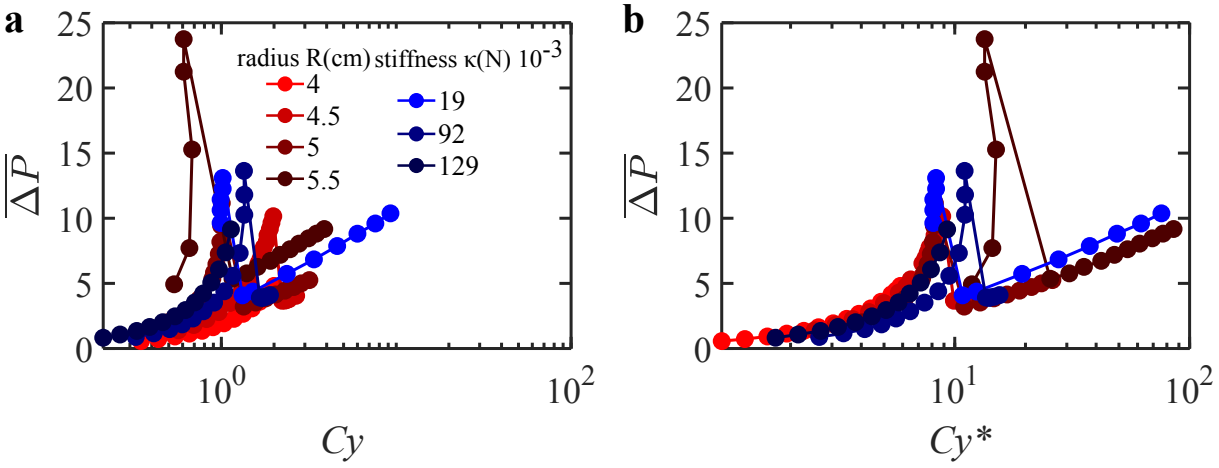

Figure 3.9: Fig.3.8 replotted using non-dimensional pressure drop with the (**a**) Cauchy number and (**b**) modified Cauchy number.

3.4 Model

In the previous chapter, we devised an aero-elastic model which gives us the equilibrium shape of the origami by the balance between the fluid forces and the elastic forces. In this chapter, we will modify it by taking into account the effect of blockage by introducing local velocity. As in the previous case where we evaluated the drag force on the unit, the pressure loss cannot be evaluated by the simplified representation of the model. Anyhow, we show that the pressure loss can be considered via eq.3.4, which solely depends on the obstruction without much influence from the shape. Thus, we will try to obtain the obstruction in the pipe from the modified model and use the equation to obtain the pressure loss.
The velocity used in the model is updated to the local velocity near the origami by using the mass conservation, this velocity is a function of the blockage. So, to find the equilibrium shape of the origami unit the equation to solve becomes:

$$(\psi_m - \psi_m^0)\frac{d\psi_m}{d\theta} + (\psi_v - \psi_v^0)\frac{d\psi_v}{d\theta} + \frac{2}{3}C_y^* \sin^2\theta \sin^2\phi \left[A\frac{d\phi}{d\theta}\sin\theta + B\sin\phi\right] = 0 \tag{3.5}$$

Where the modified Cauchy number C_y* is dependent on the degree of opening and can be obtained by mass conservation as $C_y* = C_y(\frac{A_p}{A_p - A_0})^2$. Where C_y is the Cauchy number defined with the inlet velocity U. The equation can now be solved numerically by using the modified Cauchy number and we can extract the normal area of the unit from it. Where A_p is the area of the pipe and A_o is the instantaneous area of origami. By using the eqn.3.4 and $\beta = \sqrt{(A_p - S)/A_p}$ we can estimate the corresponding pressure drop as :

$$P_1 - P_4 = (K_{1,4})_1 \frac{1}{2\beta^4}\rho v_1^2 \tag{3.6}$$

Similar to the previous chapter we vary the Cauchy number in steps of 0.01 as input and obtain the pressure drop as well as modified Cauchy number as output. The units in experiments suddenly go to higher C_y^* post snapping as compared to our model. This is discussed before while talking about the sudden change in speed post snapping. In the model this effect is not there thus post snapping the Cauchy number changes slightly, like in the previous chapter. The introduction of the blockage effect into the model restricts the model to the computation of dynamics to a maximum radius of 4.5cm for the initial opening angle of 41°. Using the model we can obtain the non-dimensional plot which scales for different stiffness values. For different radii, it seems to re scale x-axis but does not seem to work on the axis (see Fig.3.10). The

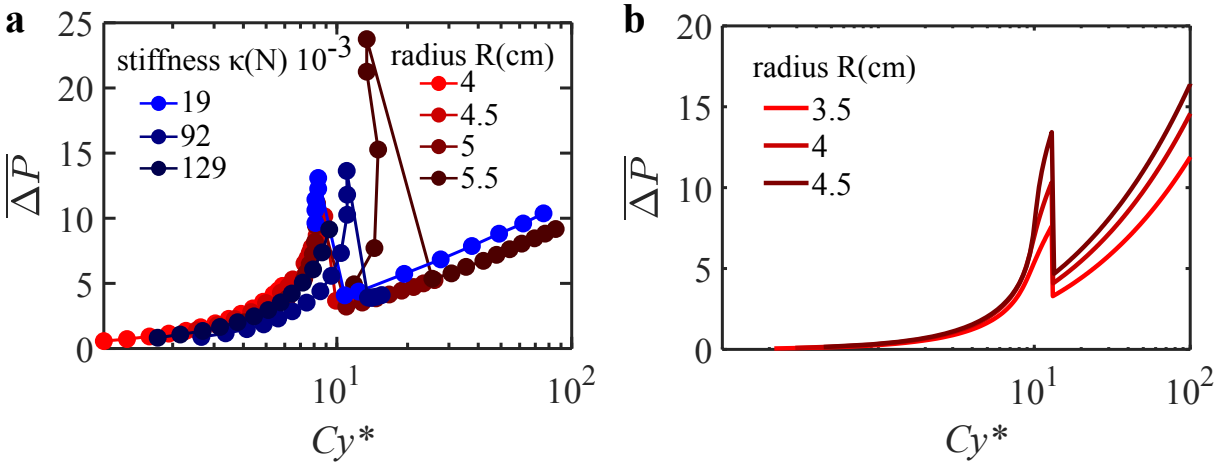

Figure 3.10: (**a**) Experimental non dimensional curve adapted from Fig.3.9. (**b**) Theoretical curves using non-dimensional numbers for different radius and fold stiffness. Both the parameters are calculated using the local flow speed seen by the Origami unit calculated via conservation of mass. The curve for different stiffness lies on the curve for different radii.

blockage may have introduced another length scale in the problem that needs to be accounted for in non-dimensional pressure. We need to investigate this further to reach a conclusion or make any claims on the general behaviour. The discrepancy between the flow profile and the non-uniform front can be a source of error in the flow.

3.5 Two units: More is different?

The obvious question after investigating an individual unit is what happens when we have two units. The experiment for two units mounted along the same axis in the closed wind tunnel suggests that the pressure drop due to two units in series can be approximated as the sum of the individual pressure drops (see figure3.11). Two units of different stiffness but other parameters being the same are tested and the individual curve is plotted in red and green for soft and stiffer units and the black curve is obtained when two units are mounted together and separated horizontally by 20cm. The curves suggest that there is no interaction between the units and they do not influence each other significantly. Following this observation and

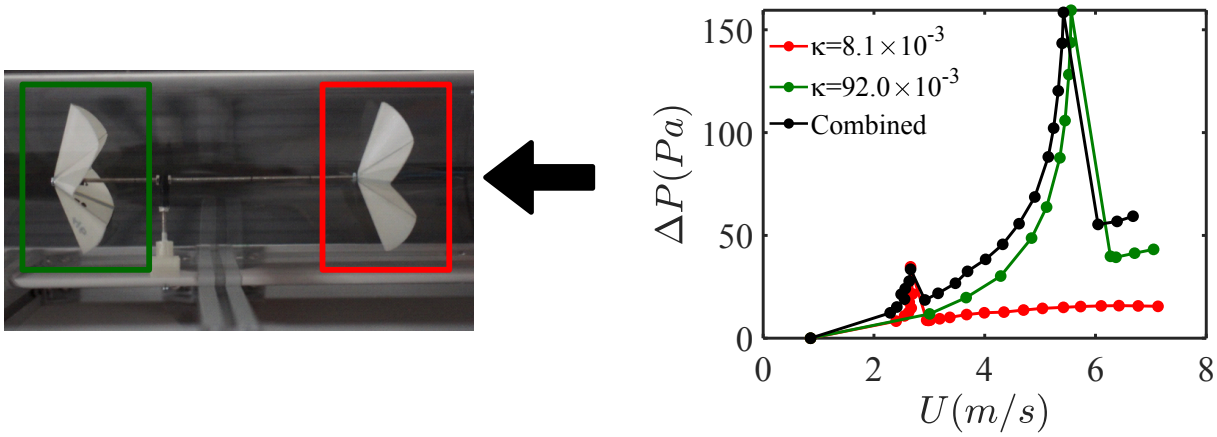

Figure 3.11: Two Waterbomb units placed in series in the confined flow separated by 20cm. The pressure drop across the system is depicted in the black curve. Green and red curves are the pressure drops across the units tested individually.

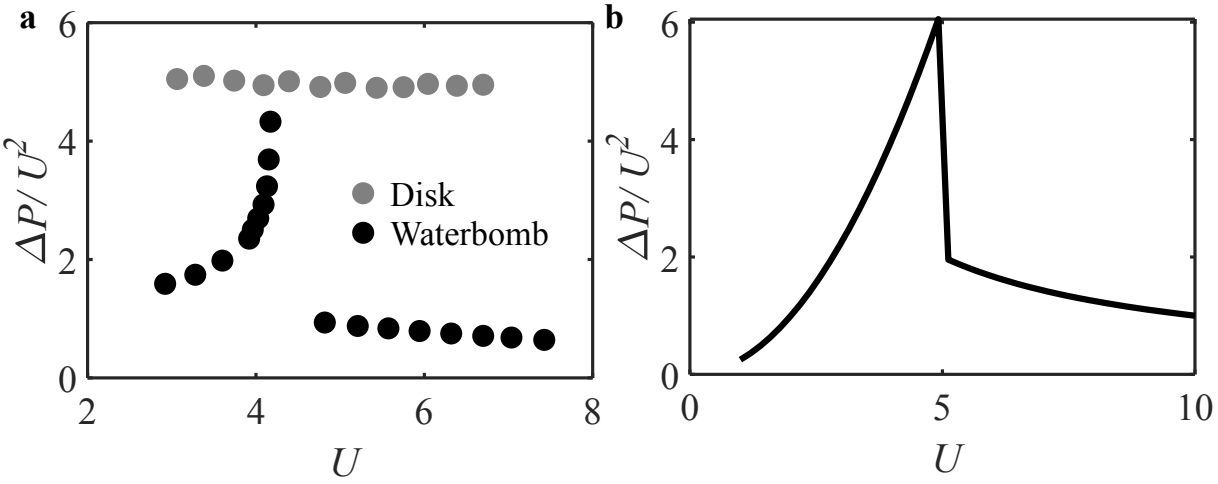

Figure 3.12: (**a**) Plot to find the resistance of the disk to the flow and the resistance of the origami unit to the flow as a function of flow speed U (black). (**b**) The resistance to the flow given by the toy model with initial quadratic growth and later inverse decay.

to explore other combinations (more than two units, or units in parallel) which are difficult to implement experimentally, we made a toy model which assumes no interaction between the units and assumes specific pressure vs flow characteristics for different units. We will exploit the analogy between electronics and fluid mechanics, where the pressure difference in our case will be equivalent to the voltage in an electronic circuit. The current will be equivalent to the flow speed, though remember in pipe flow the relation between the flow speed and pressure is not linear. The Waterbomb unit will be modelled as a non-linear resistance that depends on U which will be $R(U) = CDeltaP/U^2$, where C is a constant which depends on the geometry. For a rigid obstruction, the pressure drop is given by $\Delta P = CU^2$, where C is a constant which depends on the geometry of the obstruction. Thus for rigid object $\Delta P/U^2$ will be a straight line (see grey curve in Fig.3.12a). When the same curve is plotted for the Origami unit, we see that the initial opening part can be curve fitted to a second-order polynomial (though higher order polynomial will be required for better fit), for simplicity we will only assume it to be a quadratic function (i.e, $R(U) = C_1U^2$, with some constant C_1) and the later part post-snapping to the inverse of U (i.e, $R(U) = C_2/U$) (black curve). Based on this our toy model will have an initial opening part which leads to pressure drop as $\Delta P = C_1U^4$ and post snapping as $\Delta P = C_2U$. We have incorporated ρ and $1/2$ in the constants for simplicity. This provides us with two parameters to dictate the shape of our curve C_1 and C_2, the third parameter is the flipping flow speed which can also be incorporated into the model. Thus, taking this all into account the pressure vs flow curve for a single unit in our toy model looks like Fig.3.12b. We will now incorporate the model on the configuration in series and then apply it to more complicated parallel flow. This implication even though have three tuning parameters, it doesn't allow us to directly set the maximum pressure and the pressure jump. The model can be modified further to incorporate those.

3.5.1 Units in series

For the obstruction in series, the flow speed across both the obstructions remains the same whereas the pressure drop across individual units adds up to give the effective pressure drop across the whole system. In other words for units in series we can say :

$$\Delta P_{net} = P_1 + P_2 = R(U_1)U_1^2 + R(U_2)U_2^2 = [R(U_1) + R(U_2)]U_{net}^2 \tag{3.7}$$

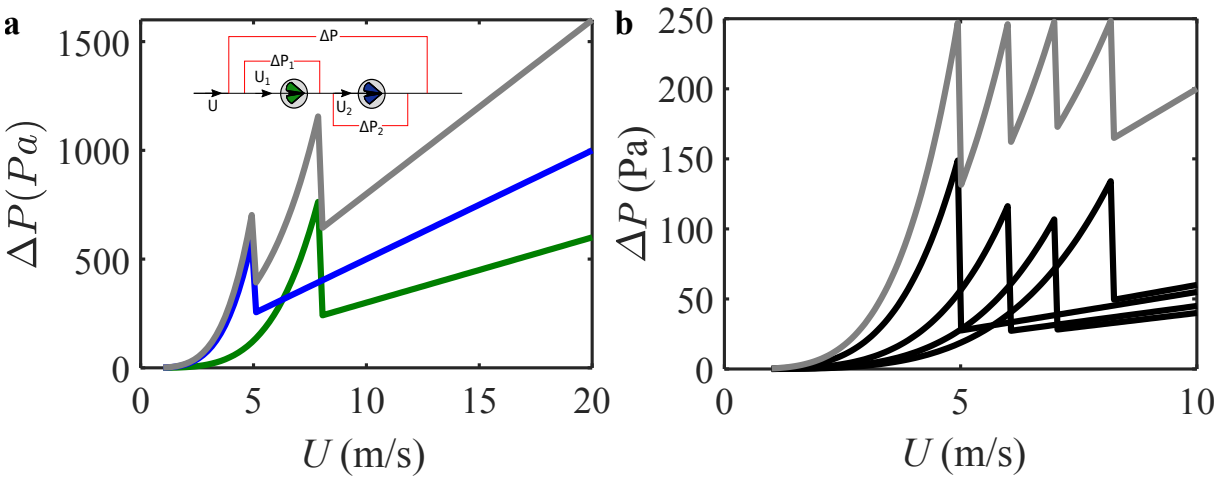

Figure 3.13: (**a**) Model depicting Pressure vs flow rate characteristics of the units placed in series. The green curve is the values across the first unit and the blue is for the second unit. Grey is the values across the whole system. See the inset for a schematic and for the points where the values are being measured. (**b**) By using multiple units in series we can limit the maximum pressure drop in the system for a given region of flow speed.

As $U_1 = U_2 = U_{net}$ in series. The results from the model for two such units are depicted in Fig.3.13a. This indicates that the combined pressure drop across the pipe can be the sum of the pressure drop across individual units. By using multiple units in series we can even limit the maximum pressure drop across the system in a given flow regime (Fig.3.13b grey curve).

3.5.2 Units in parallel

For the units in parallel, the pressure drop across the two units remains the same as the pressure drop across the system whereas the flow gets divided into two sections depending on the blockage. So for the units in parallel, we have :

$$\Delta U_{net} = U_1 + U_2 = \sqrt{P_1/R(U_1)} + \sqrt{P_2/R(U_2)} \tag{3.8}$$

With $P_1 = P_2 = P_{net}$. For the units in parallel, an anticipated but interesting behaviour can be seen. From Fig.3.14, we have two units let's assume green has a bigger radius and higher stiffness, this means that the drag on it will increase faster than the blue unit and it will flip at a higher pressure value as well (Fig.3.9). Remember as they are in parallel the pressure drop across both the units will be the same all the time and will equal the pressure drop of the system. When we increase the flow rate of the system, first the blue unit reaches its critical flow rate and flips to the second state leading to a discontinuity as seen in the blue and grey curve. Because of this the pressure in the green curve also drops(the region from where higher point density starts). After that, if we further increase the flow rate the pressure drop keeps on increasing and most of the flow passes through the blue unit side (see Fig.3.14b where most of the flow is through the blue curve). Once the critical pressure for the green unit is reached it flips to the second state as well, and most of the flow passes through the green side now, which leads to a large discontinuity in U_1 and U_2 (Fig.3.14b). Also, there is a large discontinuity in the pressure. Thus, when the units are placed in parallel, we obtain a sudden flow change on each side accompanied by a pressure drop in the system.

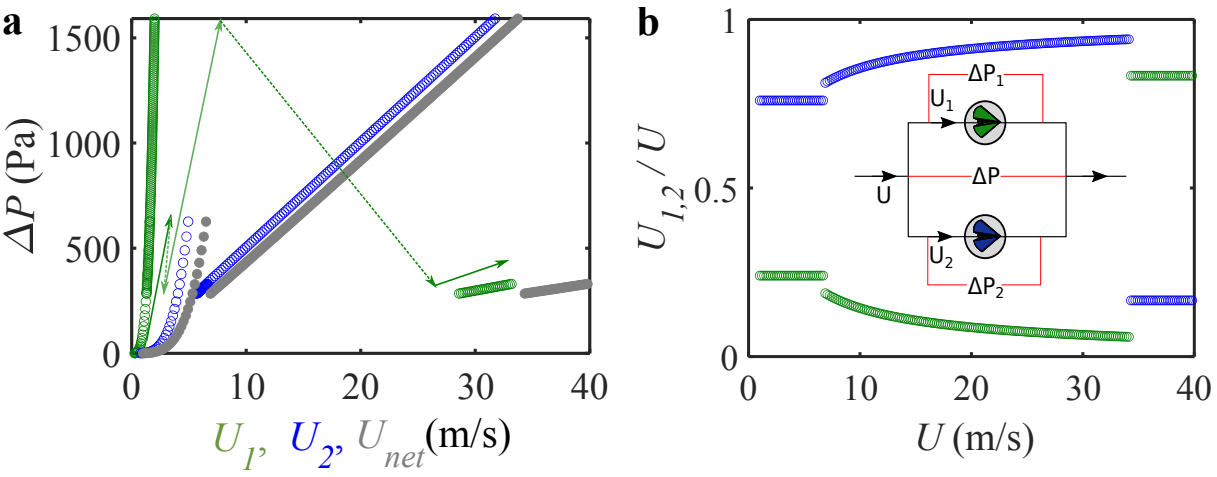

Figure 3.14: Model depicting Pressure vs flow rate characteristics of the units placed in parallel. (**a**) The green curve is the values across the first unit and the blue is for the second unit. Grey is the values across the whole system. (**b**) The ratio of flow speed to the speed imposed across two pipes in parallel is compared to indicate that initially most of the flow goes through the pipe with the second unit (blue) but after the snapping of the first unit, there is a sudden jump and further majority of the flow goes through the first unit side. See the inset for a schematic and for the points where the values are being measured.

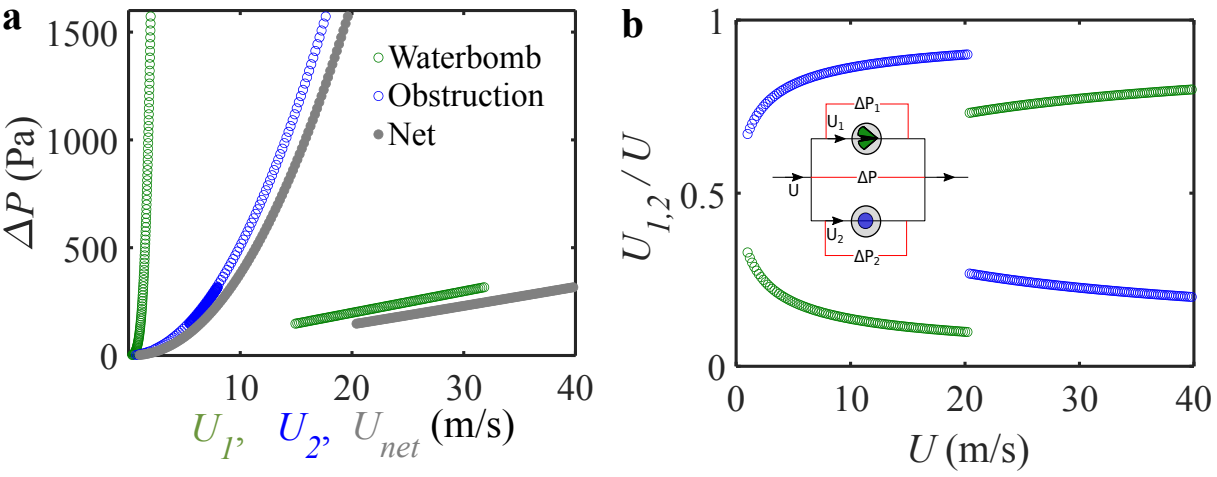

Figure 3.15: A prospective application of the Waterbomb unit as a passive pressure relief valve when placed in parallel to the main pipeline. The blue curve depicts the pressure across the pipe with a blockage, by adding the Waterbomb unit in parallel we can set the maximum pressure threshold, if the pressure in the pipe crosses that limit the Waterbomb unit will snap to release the pressure in the system. This sudden release is depicted by (**a**) the sudden drop in pressure and (**b**) the sudden drop in flow speed across the obstruction.

3.6 Conclusion

In this project, we studied an application of the Waterbomb unit's passive actuation in confined flow. The pressure drop curves across the unit look similar to the one obtained for the drag force. The differences in the pressure curve in contrast to drag curves appear to be a consequence of confinement, which was taken into account by the effective velocity. By varying various physical and geometrical parameters we were able to tune the flipping point and the pressure drop across the unit. By modifying the Cauchy number and defining non-dimensional pressure the plot rescale except for the cases where the blockage is too high (units with bigger R). Modifying the model for the Waterbomb unit to incorporate the local flow speed experienced by the flow allows us to be able to obtain the model for pressure drop across the unit. We further studied two units in series and achieved multiple peaks in the pressure curve. Using the resistance of the experimental unit we developed a toy model with similar behaviour and showed its ability to capture the behaviour of two units, further, it indicates that by having multiple units in series we can limit the maximum pressure in the system for a given flow range. The toy model in parallel predicted a sudden pressure drop across the system leading to a sudden increase in flow speed in one of the sections. This shows the ability of the Waterbomb unit as a passive pressure relief valve. When placed in parallel to a pipe flow or an obstruction, the unit will be able to flip at the critical pressure to release the pressure in the system as shown in Fig.3.15. By modifying the unit's parameters it is possible to fine tune the pressure threshold. In a pulsative flow, at low flow rates pre-snapping, as the resistance in one direction will be much higher than the other direction, the unit can act as a semipermeable membrane or can lead to directed flow as shown by Brandenbourger et al.[104, 120]. The future implications can be to reverse engineer the units to have the desired pressure curve or add multiple units to have interesting pressure vs flow characteristics as shown in Park et al.[108]. In the study, it was shown that by combining multiple non-linear resistances in series and parallel combinations, it is possible to get rectangular, triangular and other interesting flow profiles.

Chapter 4

Flow induced transition via hidden degree of freedom

Fun fact:**"Bull" by Emre Ayaroglu.** Akira Yoshizawa invented the art of "wet-folding". Wet folding involves dampening paper to shape and mould it easily. This is an extreme example of facet bending, where adding water makes the folded structure have smooth edges and they look similar to sculptures. A small change leads to large implications.

In this chapter, we utilized the hidden degree of freedom of the Miura ori origami structure to transition from one rigid configuration to the second rigid configuration using fluid loading. In the previous chapter, the snap-through transition occurred by moving along the folding trajectory and passing through the flat unstable state, whereas in this chapter it occurs through facet bending. The facet bending allows the folding which was not possible for the structure with rigid facets. Tuning the stiffness of the hidden degree of freedom tunes the load-bearing capacity of the structure and the compliance of the structure under fluid loading. This will allow the structure to undergo large shape changes while maintaining resistance to aerodynamic load with minimal deformation in the deployed state. Experiments were conducted to study the influence of geometrical and mounting parameters which act as control parameters to fine-tune the flipping. The structure can further be adapted to have multiple rigid configurations by combining more vertices which shows different aerodynamic performance under different flow conditions.

Contents

4.1 Introduction

In the previous chapters, we saw that transitioning between equilibrium states for the Waterbomb base requires passing through a flat state, which leads to a sudden reduction in drag forces. In the opening phase as the crossectional area grows with the increasing flow speed, we observe drag increase faster than the rigid case. This can be advantageous for various applications as we discussed in previous chapters. Another way to achieve drag discontinuity without the initial increase in drag force can be the use of other bistable mechanisms, which do not require passing through the flat state. An example is the degree-four vertex (where four folds converge at a central vertex). The general four-vertex unit features two folding pathways that intersect at the flat state (see Fig.4.1a lower panel). By choosing specific values of rest angles and crease stiffness for the folds (Fig.4.1a), it is possible to attain a unit with two bistable states, both lying on the same side of the flat state[66]. This configuration might result in an initial increase in drag at a slower rate than the rigid mechanism before snap-through, depending on the evolution of the frontal area and the shape's streamlining. Such mechanisms are more challenging to implement with our fabrication method, as they require individually prescribing the rest angle of each fold through annealing before assembling the unit. Another interesting option is snap-through allowed by facet bending (rather than motion along the folding branch as we saw in the Waterbomb unit), which provides a 'hidden' degree of freedom [81]. In our study, we focus on a specific type of four-vertex unit known as the Miura-ori. This unit has two collinear spinal creases and two peripheral creases that are mirror images of each other[66, 81]. The Miura-ori unit has two symmetric folding pathways: in one, the spinal creases are collinear (with the angle from the flat state of lower and upper right facets being identical ($\theta_1 = \theta_2$)) and the peripheral creases are flat; in the other, the spinal creases are offset by some angle (which leads to the lower and upper facets to have angles as ($\theta_1 = -\theta_2$)) and the peripheral creases have the same non-zero angles (see Fig.4.1b). An individual structure made up of rigid facets, with deformation localized to the creases, is kinetically constrained to follow one of the folding pathways and can transition from one to the other only via the flat state. Introducing facet bending in the structure allows it to transition between states that were not possible under the rigid foldable assumption[75]. A previous study on the square twist unit, which has zero degrees of freedom but can still transition between two stable states via facet bending[58], highlights the importance of this hidden degree of freedom[73]. The twisting and out-of-plane bending mode of the Miura-ori sheet is also a consequence of facet bending. This bending allows it to exhibit bistable states[121, 122], which can be fine-tuned by modifying the crease and facet stiffness[123]. This can also be used to create pop-through defects to adjust the compressive stiffness of the tessellated sheet[74, 124]. Another way to introduce multiple stable states is by making stretchable creases or non-linear crease stiffness[71, 123, 125]. This changes the potential energy curve for the rigid foldable unit and introduces multiple stable states which are easily accessible.

Recent studies have shown another kind of bistable transition in this unit via dynamic actuation. Dynamic actuation of the Miura unit, with its base held at a certain angle, has been gaining traction for applications in soft robotics, enabling fast, reproducible actuation[81]. This can be achieved by holding the lower facet and moving the whole system[126], by rotating the lower facets[81], or by coupling the system to another bistable unit[82].

In our study, we use the same unit and employ fluid forces as the actuation mechanism, exploring the transition between rigid states (Fig.4.1b) under the influence of airflow. This transition can be easily tuned by tuning the stiffness coming from the hidden degree of freedom via changing the geometrical parameters as we will discuss. This approach allows the unit to undergo significant shape changes while maintaining resistance to aerodynamic loads with minimal deformation in the initial state, thus ensuring a relatively constant drag coefficient.

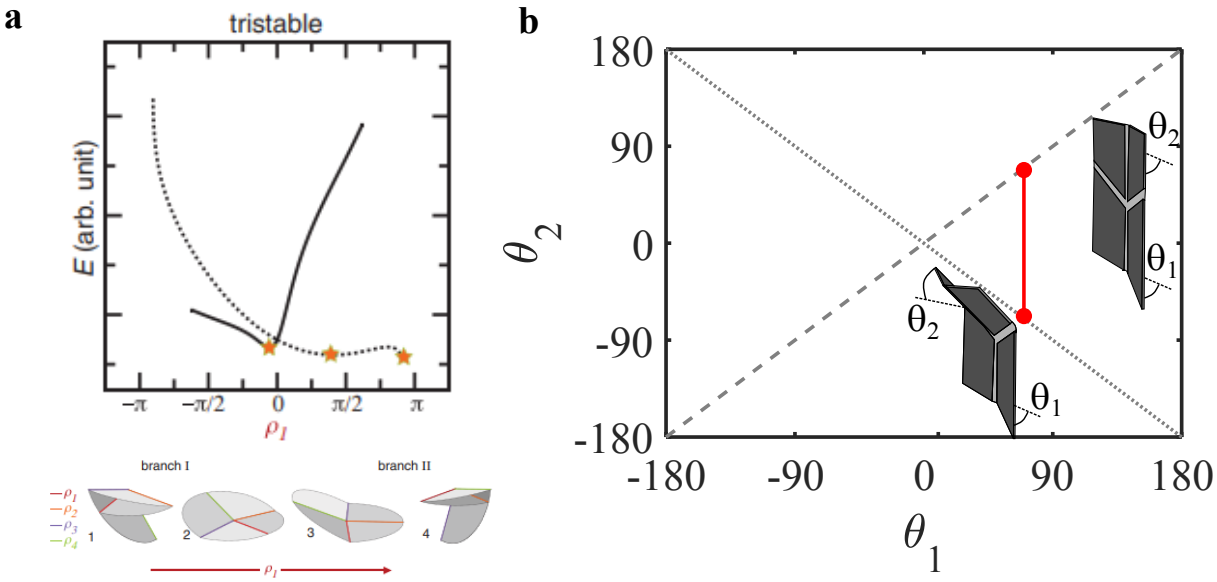

Figure 4.1: (**a**) The two folding pathways for non-generic four vertices unit depicted by two lines on the energy plot as a function of one of the crease angles which guides the folding. The two folding pathways intersect at the flat state and the unit shows three stable states. (**b**) The folding pathways for Miura ori unit under rigid foldability assumption and the transition between two states via the hidden degree of freedom from facet bending marked by red branch.

4.2 Miura ori unit

4.2.1 Folding kinematics

An origami structure is considered rigidly foldable if all the sector angles remain fixed and all motion occurs at the creases. The Miura-ori is a rigid foldable unit, meaning it can be completely folded via the motion of its creases. As we discussed before it can fold into parallel configuration ($\theta_1 = \theta_2$) and antiparallel configuration($\theta_1 = -\theta_2$) as shown in Fig.4.1b. For the parallel configuration, the angle between the two lower facets and two upper facets are identical and the peripheral crease remains flat. Whereas for the antiparallel configuration, the angle between the lower facets and upper facets around the spinal creases are inverted (see Fig.4.1$\theta_1 = -\theta_2$). The angle between the upper and lower spinal creases can be derived using geometry and trigonometry[58, 72, 127, 128]. We will not give the whole derivation in this chapter but for completeness, we will quickly give the method to be followed to derive the equations and provide the final results which will be used in the later part of the chapter. The derivation is adapted from the work of Kamrava et al.[127].

The unit can be described by a single degree of freedom; in this case, we use the angle β between the mountain and valley folds as the parameter (Fig.4.2). By taking the dot product between the vectors $\vec{AB}$ and $\vec{AC}$, we obtain the relation:

$$\cos\phi\cos\gamma = \cos\alpha \tag{4.1}$$

Considering the isosceles triangles, ABF and AED and using trigonometry, another relation can be derived:

$$\sin\alpha\sin\theta/2 = \sin\phi \tag{4.2}$$

By combining these two equations and eliminating ϕ, we can express γ in terms of the other parameters. Given that $\beta = \pi - 2\gamma$, we derive:

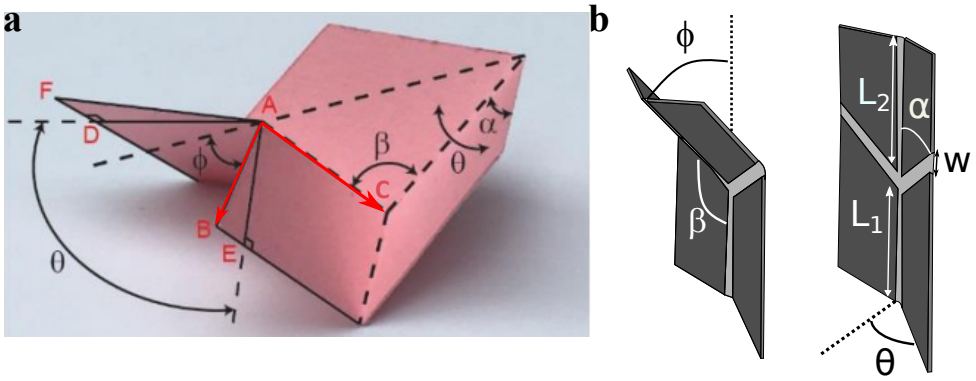

Figure 4.2: (**a**) The geometry of the Miura ori unit used to derive the kinematic equation for the unit, adapted from Kamrava et al.[127]. The facet on the right is equivalent to the lower facets in our case (the figure on the right) and the ones on the left to the upper facets. (**b**) The various geometrical features of the rectangular Miura ori unit were used for our study. The mounting angle θ, vertex angle α, length of upper facet L_2, length of lower facet L_1 and the angle characterizing the deformation of the unit measured from the vertical parallel state ϕ.

$$\beta = \pi - 2\arccos\left(\frac{\cos\alpha}{\sqrt{1-(\sin\alpha\sin\theta/2)^2}}\right) \tag{4.3}$$

Note that using this equation we can derive the value of ϕ shown in Fig.4.2b as $\phi = \pi - \beta$, which is the angle we will use in our geometry. Now, that we know how the Miura ori folds, let's look at the fabrication of the unit.

4.2.2 Fabrication process

For the study, we use a rectangular Miura ori unit. As discussed in the first chapter we use the layer superposition technique to fabricate the Miura ori unit. The rigid facets(mylar sheet of thickness $350\mu m$) were laser cut and superposed on the thinner sheet with stiffness $\kappa = 19\times10^{-3}$ N using a double-sided tape. The crease width was taken to be $w = 2$mm and the width of each of the facets was taken to be $W = 3$cm. In this study we do not impose any rest angle to the unit so we skip the annealing process where we keep the unit in the oven thus the rest angle for all the creases is $0°$. The fabrication allows us to vary the length of the upper facet L_2 and the vertex angle α (Fig.4.2b). To rigidify the upper facets of the unit and avoid upper facet bending for the structure to snap we add a 3D printed frame to the upper facet which increases the bending stiffness without affecting the potential energy curve of the unit (see discussion in what sets the stiffness section). The length of the lower facet (measured along the central edge) is always kept constant $L_1 = 4$cm. While varying the vertex angle α, L_2 is kept constant such that the area of the flat sheet remains constant. If we increase the vertex angle that implies that the area of the upper facet increases and the lower one decreases. As the units fabricated using the layer superposition method are allowed to have facet bending and the crease thickness is not negligible (2mm), it is better to test the two stable states of the units with respect to the theoretical prediction. For this, we mounted the unit in parallel configuration on a 3D printed piece to fix the lower facet angles to θ and pushed the upper facets by hand to snap to the anti-parallel state. The green dots depict the opening angle ϕ^* measured from a picture of the mounted unit as a function of increasing vertex angles. The parallel configuration for all the parameters is close to $\phi = 0$ whereas the anti-parallel configuration for the bistable units is close to the theoretical curve (dashed green line)(Fig.4.3). Similarly, the red curve for different θ and the blue curve for different L_2 also seems to follow the theoretical trend. The theoretical curve is calculated from the eq.(4.3), where $\phi = \pi - \beta$. The units follow the theoretical trend with

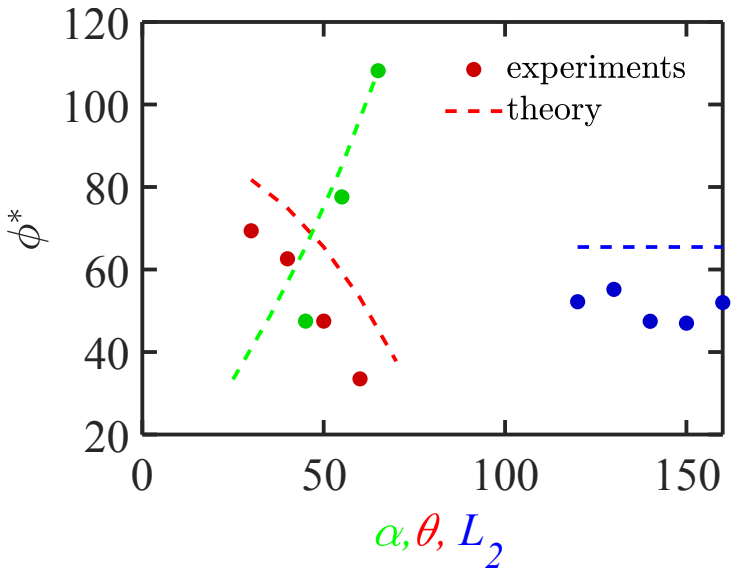

Figure 4.3: Comparison of the rest angle in the antiparallel flipped state measured experimentally (dots) with the theoretical value in the flipped state (dashed line) for different geometrical parameters of the unit depicted in different colours.

slight discrepancies between the theoretical and experimental values coming from the fabrication process. We believe better fabrication techniques will allow better correspondence between the experiments and theory, but it is not the main objective of the thesis. To characterize the fabricated unit we did a mechanical test.

4.2.3 Mechanical test: Stiffness of the unit

For the mechanical testing of the unit we followed the work of Liu et al.[81]. By fixing the lower facets to a given mounting angle they applied a point force at the top of the upper crease. When the torque is applied, the upper facet will deflect changing θ_2 and ϕ (Fig.4.2). These deflections are lumped into a single pseudojoint at the vertex (Fig.4.4b inset). This pseudo joint allows the upper two facets to move independently of the lower two facets. To model the stiffness of this pseudo joint, the upper edge of the upper spinal crease was attached to the Instron machine via a thread and pulley system with negligible friction and slowly displaced (at a rate of 30mm/min acquiring 2 data points for force and displacement each second) while keeping the lower facet angle fixed to θ (Fig.4.4a). We mount the lower facet of the unit at a given angle θ with the help of a 3D-printed part. The part is such that it shadows 2 cm of the lower facet and the facet is attached to it with the help of a paper clip(we tried with screws first and the results were not different so we decided to use a paper clip for ease of its use). As the units were soft and the contribution of the mass of the unit to the potential energy was not easy to separate from the potential energy coming from purely the elastic energy of the material, we decided to experimentally calculate both of them together as they will contribute to the actual experiments in the airflow. For this, the unit is mounted with the spinal crease facing vertically, similar to the experiments done in the wind tunnel as we will discuss later. The force sensor on the Instron machine measures the force as a function of displacement till the unit snaps. A video(Nikon DSLR camera used at 60 fps) taken from the side to measure the angle by which the upper facet has deflected with respect to the lower facet as well as the angle between the pulling direction and the top facet is used to extract the angle for calculating the torque. As the Instron machine moves vertically the unit connected to it by the thread and pulley system displaces as a consequence it starts to deform changing θ_2 and ϕ. In our case, we only measure

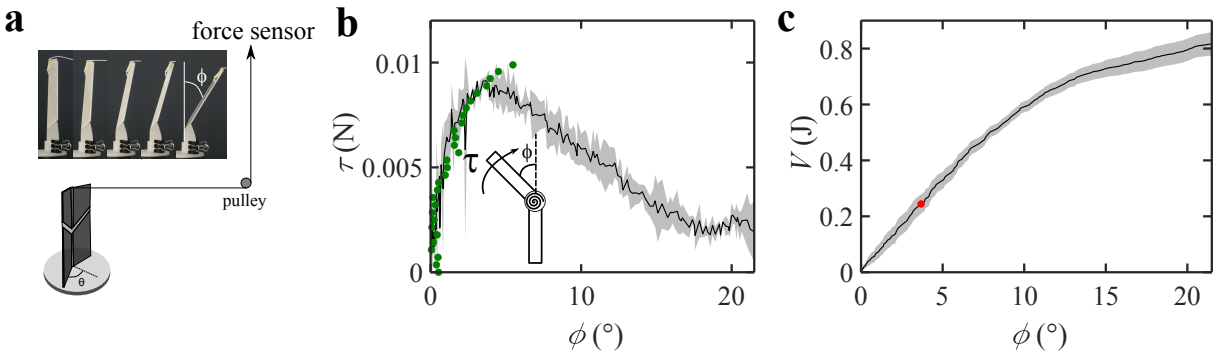

Figure 4.4: (**a**) Experimental setup for obtaining the torque-angle curve using the Instron machine for unit mounted at angle θ. Different intermediate states during the bending process of the unit are shown above the setup. (**b**) The torque-angle curve from the mechanical test using the Instron machine depicts the mean value (black curve) with standard deviation over three measurements as an error bar in the grey curve. The unit starts from the parallel state and flips to the antiparallel state when ϕ is 21.5°. The unit when loaded with incremental masses flips when the torque reaches the maximum torque (green points). The prototype of the pseudo joint is presented in the inset. (**c**) Integration of the torque over the angle (ϕ) gives the potential energy curve. The red dot depicts the location of the maximum torque or the inflection point on the potential energy curve. The data is is depicted for the specimen with $\theta_0 = 50°$, $\alpha = 45°$ and $L_2 = 14$ cm.

ϕ and using a Matlab code the force is converted to the torque applied to the unit as a function of ϕ (Fig.4.4b). We see that as the unit is deformed it has an initial phase where the torque on it increases with the angle ϕ, indicating a positive stiffness. After that, we reach a maximum torque followed by a decrease in the torque with increasing angle. This decrease in torque with the angle indicates a negative stiffness. On further increasing the deformation, the torque decreases till the unit snaps (end of the curve in Fig.4.4b) to the antiparallel configuration. We repeated the measurements three times for all the units to calculate the average and standard deviation on them. We did another test in which in spite of using an Instron machine to displace the endpoint of the unit (displacement test) we added a small mass to the endpoint (tension test), the test indicates that whenever the (Fig.4.4b green)torque imparted by the mass exceeds the maximum torque from Instron test, the unit flips to antiparallel configuration. Using the Instron test, the potential energy of the unit can be calculated by integrating the torque along the displacement. The maximum point on the torque curve corresponds to an inflection point on the potential energy curve, it is indicated by a red dot on Fig.4.4c. This point marks the transition between the positive and negative stiffness of the unit. We have developed the tools for the test, let us now look at the origin of the mechanical property of the unit, and which part of the fabricated unit plays the dominant role in tuning the mechanical property of the unit.

4.2.4 What sets the stiffness of the unit

In order to better understand the origin of the stiffness of the unit, i.e. does the hidden degree of freedom result from bending modes of the facets if so which facets or it arises from bending or twisting of creases, we tested units with different facets and crease thickness. For the first test, we increased the thickness of the two lower facets making them twice and thrice thick while maintaining the upper facet to a single sheet and crease of stiffness per unit length as 19×10^{-3} N. The torque curve indicates that the lower facet thickness influences the maximum torque of the unit significantly making it almost twice and thrice the value for a single facet value indicating that the maximum torque grows proportionally to the lower facet thickness (Fig.4.5a). Secondly,

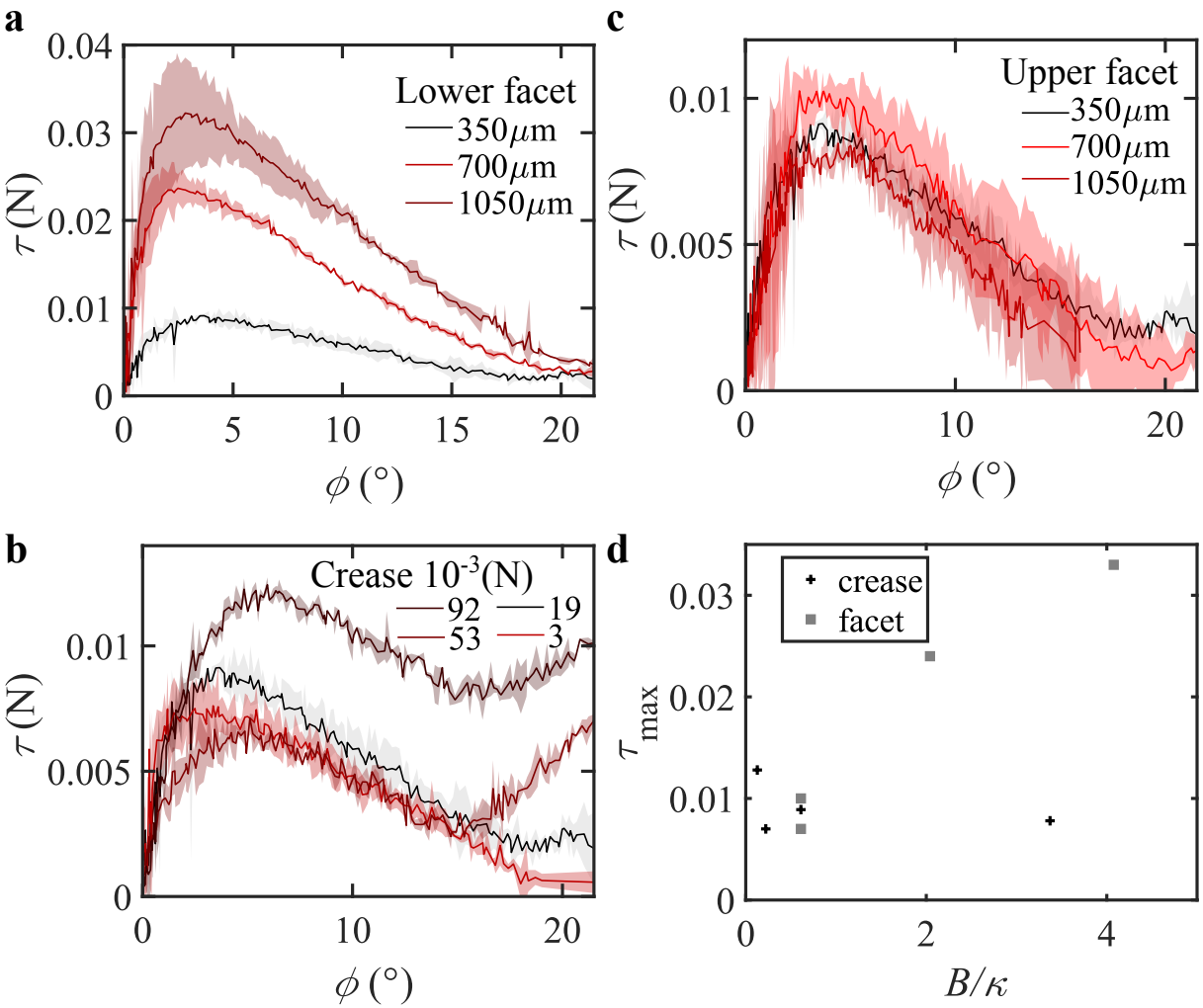

Figure 4.5: (**a**) Influence of lower facet thickness, (**b**) upper facet thickness and (**c**) crease stiffness on the torque of the unit. The lighter colours are for thinner sheets and the darker are for thicker sheets. (**d**) All parameters' influence is combined by plotting maximum torque as a function of effective length set by bending modulus of the lower facet and crease stiffness. The unit with parameters $\theta_0 = 50°$,$\alpha = 45°$ and $L_2 = 14$ cm made with single facet thickness and crease stiffness of 19×10^{-3}N is common among all the graphs in black.

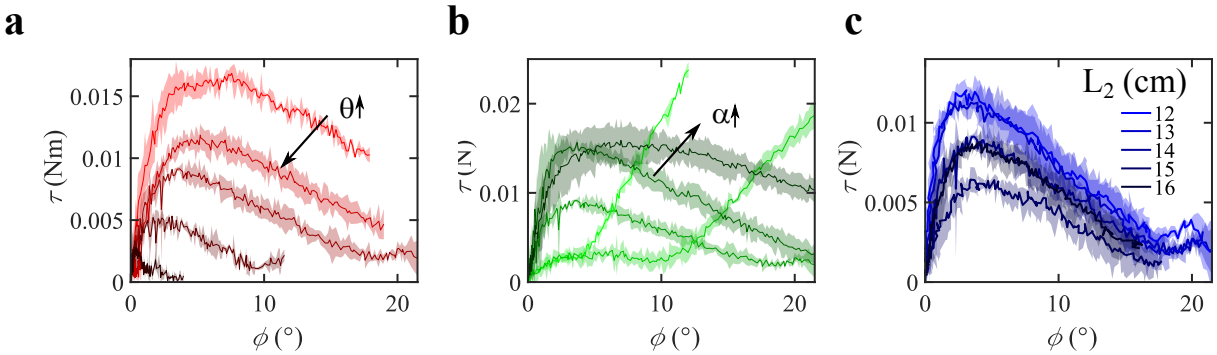

Figure 4.6: Torque-angle curve for units with different (**a**) mounting angle (θ), (**b**) vertex angle ϕ and (**c**) the upper facet length L_2. The units with $\theta = 50°$, $\alpha = 45°$ and $L_2 = 14$ are common in all the graphs.

we vary the thickness of the upper two facets while maintaining the other parameters constant to the lower facet of a single sheet and crease of stiffness per unit length as 19×10^{-3} N. Increasing the facet thickness to twice increases the maximum torque of the unit slightly which is reduced below the single sheet on adding the third layer of the sheet (Fig.4.5b). The observed change lies within the standard deviations indicating that the upper facet thickness does not contribute significantly to the stiffness of the unit or we do not have the experimental precision to see the difference. Next, we vary the crease stiffness as $\kappa = [3, 19, 53, 92] \times 10^{-3} N$. Similar to the upper facet, the crease stiffness does not modify the maximum torque significantly. Even though the maximum torque does not increase monotonically and the change is not significant, the units with crease stiffness 53 and $92 \times 10^{-3} N$ return back to the initial position when the loading is removed indicating that the unit is monostable(Fig.4.5c). To compare the effect of all the parameters together we plotted maximum torque as a function of the ratio of bending stiffness of the lower facet and the torsional stiffness of the crease. The bending stiffness of the facets was measured on a 14 cm long and 3 cm wide rectangular sheet while fixing one end and adding increasing load to the other end. The plot indicates that for the whole range of the parameter, the crease stiffness does not have a significant effect on the maximum torque whereas facet thickness shows a linear increase in maximum torque (Fig.4.5d)[122]. In conclusion, the bending stiffness of the lower facet has the maximum contribution to the stiffness and the maximum torque of the unit, whereas the upper facet thickness and the crease stiffness do not contribute significantly. Once we have identified which facets play the dominant role in the mechanical properties of the unit, let's test units with different geometries.

4.2.5 Parametric study

Let us discuss the influence of various geometrical parameters on the mechanical test of the unit. For different measurements we varied $\alpha = [25°, 35°, 45°, 55°, 65°]$, mounting angle or the opening angle of lower facet $\theta = [30°, 40°, 50°, 60°, 70°]$ and the length of the top facets $L_2 = [12, 13, 14, 15, 16]$ cm. The first parameter was the mounting angle of the unit θ, we varied it while keeping the other parameters fixed to $\alpha = 45°$ and $L_2 = 14$ cm. As shown in the previous studies[81] on decreasing the lower spinal angle from 70° to 30° (going from dark red to light red curve) we observe an increase in the maximum torque of the unit (Fig.4.6a). As we discussed previously, the stiffness comes dominantly from the bending of the lower facet. If the unit is more closed (smaller angle) the lower facets need to bend more for the upper facets to come to the flat state and flip, thus the unit with a lower angle has higher stiffness. Termination of the torque curve indicates that the unit has snapped to the second stable state leading to zero force afterwards which has not been plotted. Note we use different notations to define the

angle between the lower facets compared to the previous studies[81]. The difference comes from the fact that we use the half angle between the two facets and not the angle of one facet from its unfolded state as done in previous studies.

Secondly, we vary the vertex angle of the unit while keeping the mounting angle as $\theta = 45°$ and upper facet length $L_2 = 14$cm. On increasing the vertex angle from 25° to 65° we observe that the maximum torque of the unit increases (Fig.4.6b, the angle is increasing from light green curve to dark green curve). The reason for such a behaviour is not clear yet, but a plausible reason can be, on increasing the vertex angle the effective length of the facet that bends for the unit to flip increases. This can be validated by measuring the deformation or the stress concentration of the lower facets during the bending process. We also observe that the unit with lower vertex angles $\alpha = 25°$and 35° are monostable and can return to the initial position when the load is removed. Thus for these units, as we increase the angle ϕ beyond their flipped anti-parallel state, the torque on these units increases.

The third parameter we vary is the length of the upper facet while keeping the other two parameters fixed as $\theta = 45°$ and $\alpha = 45°$. On increasing the length of the upper facet the length of the upper spinal crease increases so that we anticipate an increase in stiffness or maximum torque of the unit but no such trend is observed in our measurements (Fig.4.6b). We see that the maximum torque of the smallest unit ($L_2 = 12$ cm) is highest and it decreases with increasing L_2(from 13 cm till 15 cm) and suddenly increases again for $L_2 = 16$ cm. We currently don't have an understanding of this behaviour, the potential reason for this non-monotonic behaviour can be that the torque is not only set by the stiffness of the unit but also by the weight of the unit. Decoupling these two influences can provide a further understanding of this parameter.

In this section we observed the influence of three variables the vertex angle, the mounting angle and the length of the upper facets on the maximum torque and the stiffness of the unit. It is not easy to reason for some of our observations and thus a mechanical model will be necessary to better understand the influence of various parameters on the stiffness of the unit. In our experiments, we were not able to decouple the influence of the weight and stiffness of the unit. Using the model the effect of both these parameters would be studied independently. Also, it will be possible to see the actual bending of the facet and to be able to identify the virtual crease on the facet along which most of the bending is focused.

Even though most of the units tested were bistable, for some of the parameters the unit is monostable i.e., after the force is removed the unit comes back to its initial parallel state for example for the pair (θ, α) as $(50°, 25°)$ and $(50°, 35°)$, some of the units can be made monostable by increasing the crease stiffness to $\kappa = 53 \times 10^{-3}$N and $\kappa = 92 \times 10^{-3}$N. Thus by choosing different parameters, it is possible to make the unit mono-stable. The monostable units are useful for their reversible nature, in the presence of flow the unit will deform to change shape and come back to the initial state when the load is removed. Now, that we have characterized the unit let's see the behaviour of the units in the flow.

4.3 Snapping in flow via hidden degree of freedom

In the mechanical test, we saw that the unit can snap to the antiparallel configuration starting from a parallel configuration when the torque on the unit increases beyond the maximum torque (Fig.4.4b green curve). This external torque on the unit can be applied by the fluid forces leading to snap through transition. Let us contrast this transition with the transition of the Waterbomb unit.

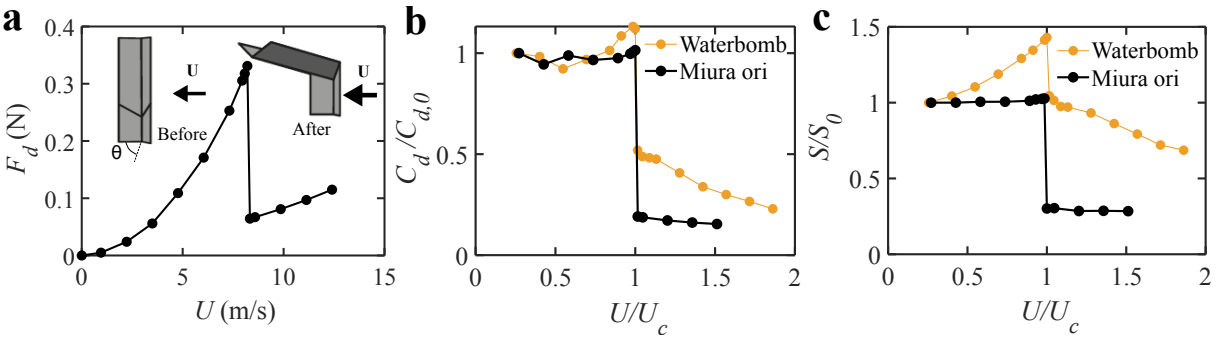

Figure 4.7: (**a**) The variation of drag force experienced by the Miura ori unit with increasing flow speed with inset depicting the experimental process. The unit has parameters $\theta_0 = 50°$,$\alpha = 55°$ and $L_2 = 14$ cm. (**b**) Comparison between the folding dynamics of the Waterbomb and Miura ori unit using the drag coefficient and (**c**) the normalized projected area as a function of non-dimensional flow speed. The parameters for the Waterbomb unit used is $R = 5$cm, $\theta_0 = 41°$, $N = 8$ and $\kappa = 19 \times 10^{-3}$N.

4.3.1 Drag on Miura ori unit and comparison with the Waterbomb unit

To measure the drag force on the fabricated Miura ori unit we mount the lower facet of the unit at a given angle θ in the flow with the help of a 3D printed part and paper clip. This whole structure was mounted on a six-component force sensor with the unit's convex side facing the flow and drag force was measured over 30 seconds(see inset of Fig.4.7a). The drag curve indicates an initial region where the drag forces increase with increasing flow speed. Then when the torque applied by the fluid forces exceeds the critical torque the unit snaps to the antiparallel state. Further increase in the flow rate leads to an increase in the drag forces (Fig.4.7a). To see the effect of the geometry on the drag forces and how close the behaviour of the unit is to the rigid object we plotted the drag coefficient scaled with the drag coefficient of the initial state $C_d/C_{d,0}$ with the non-dimensional speed (U/U_c), which indicates that the coefficient remains almost constant in the two regions for the Miura unit in contrast to the Waterbomb unit where the coefficient increases in the opening state and decreases in the closing state (Fig.4.7b). The drag coefficient for the units is defined as $C_d = 2F_d/\rho U^2 S$, where S is the normal frontal area of the unit to the flow defined in the initial state and $C_{d,0}$ is the first element of the C_d, which is calculated at low flow speed around 1 m/s. A picture using the camera placed two meters downstream was also taken to measure the frontal area to see if the unit maintains its shape at different flow speeds. The projected area divided by the initial area indicates that the unit remains rigid before and after snapping when compared to the Waterbomb unit, where the area increased in the opening phase and decreased in the closing stage (Fig.4.7c). Thus we have a unit which behaves like a rigid object before and after snapping whose snapping can be controlled by the fluid load.

4.3.2 Monostable and bistable units

As discussed in the section on the mechanical study of the unit, some of the fabrication parameters may lead to the monostability of the unit. The bistable unit once flipped cannot come back to the initial position unless a flow in the inverse direction is applied to it. This limitation of the unit is overcome in the monostable unit, which can return to its initial state in the absence of load. The study of the bistable unit with $L_2 = 14$ cm, $\theta = 50°$ and $\alpha = 55°$ in the airflow leads to the drag force on the unit similar to Fig.4.7 while the flow speed is increased. When the flow rate is decreased after the unit has snapped, we observe lower drag forces on the unit as the unit retains its second stable state which has a lower normal area (4.8a). Also, from the

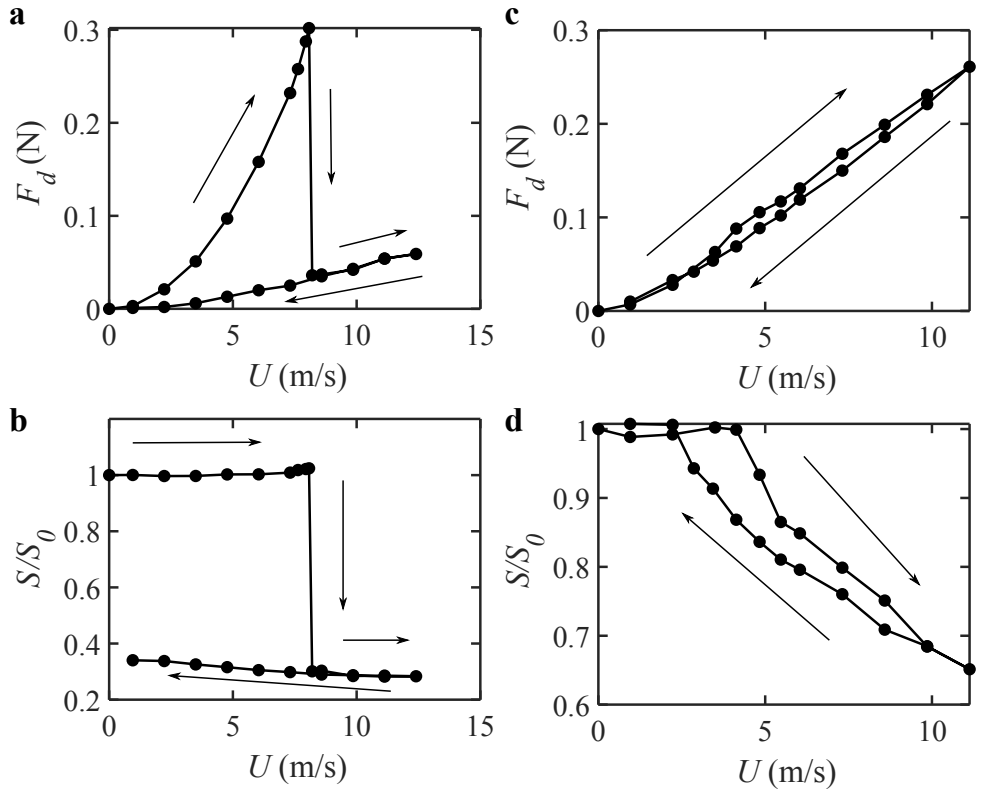

Figure 4.8: Evolution of the drag force and the normalized projected area with the flow speed for the bistable (**a,b**) and monostable (**c,d**) units. The flow is first increased to 12 m/s and then reduced back to 0 m/s.

projected area we can see that the unit post-snapping is bending a bit with increasing flow as seen in the decreasing area in the lower part of the curve (Fig.4.8b). In contrast, the monostable unit (4.8c) with $L_2 = 14$ cm, $\theta = 50°$, $\alpha = 45°$ and crease stiffness of $\kappa = 53 \times 10^{-3}$N depicts continuous deformation with increasing flow rate. The unit comes back continuously to the initial state when the flow rate is reduced from the maximum flow rate. The drag force increases and decreases continuously with a hysteresis which is also seen in the normalized area (4.8d). We contrasted the dynamics of the Miura ori unit with the Waterbomb unit and highlighted the possibility of making a monostable unit with it. Let us investigate the influence of various parameters on the drag features attained by the unit.

4.3.3 Parametric study

For the parametric study of fabrication parameters on the drag features we used 12 units with vertex angles ranging between $\alpha = 35° - 65°$, mounting angle or opening angle of lower facet $\theta = 30° - 70°$ and the length of the top facets $L_2 = 12 - 16$ cm. Firstly, we vary the mounting angle of the lower facet while keeping other parameters constant to $\alpha = 45°$ and $L_2 = 14$ cm. Fig.4.9a shows the drag force experienced by units with increasing flow speed for different mounting angles. The drag features are similar to what we discussed in the previous section. Initially drag force increases similar to the case of rigid object, followed by transition which leads to discontinuity and afterwards drag increases further. Before the snapping, the units with lower mounting angles have lower frontal area and are more streamlined as a consequence the drag on units with low mounting angles increases at a slower rate compared to the units with higher mounting angles. As we can see in the potential energy curve (Fig.4.6a) the more closed the initial shape of the unit is the stiffer it is and the higher its maximum torque. As a consequence

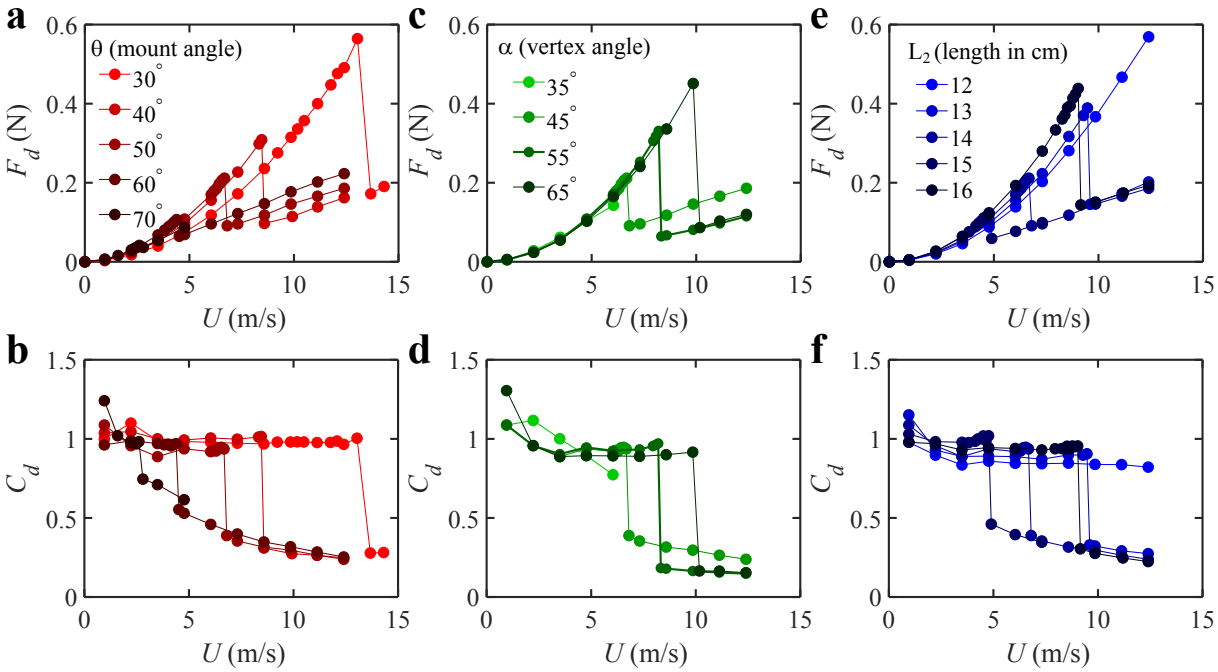

Figure 4.9: Evolution of the drag force and the drag coefficient with the flow speed for the unit with different (**a,b**) mounting angle θ, (**c,d**) vertex angle ϕ and (**e,f**) length of the upper facet L_2. The units with $\theta = 50°$, $\alpha = 45°$ and $L_2 = 14$ are common in all the graphs.

of this and the low initial normal area, the unit with a lower mounting angle flips at a much higher flow speed. The jump is higher in the unit mounted at a low angle because the unit flips to a much closed antiparallel state (Fig.4.3). As the drag coefficient post snapping (Fig.4.9b) is lower for the closed unit, the drag forces on it increase at a slower rate post snapping. The drag coefficient is defined as ($Cd = 2F_d/\rho U^2 S_0$), where S_0 is the projected area of the unit in the mounted state given by $S = 2W(L_1 + L_2)\sin(\theta)$, where W is the width of the facet. The drag coefficient indicates that the unit behaves rigidly before snapping and deforms slightly because of facet bending in flow post-snapping leading to a reduction in the drag coefficient(4.9b). Thus, by decreasing the mounting angle we can increase the maximum drag force experienced by the unit as well as the drag jump.

Next, we vary the vertex angle while keeping the mounting angle $\theta = 50°$ and $L_2 = 14$ cm. As the initial frontal area for all the units is the same, the drag curve initially overlaps for all the units. The unit with a lower vertex angle as it has lower τ_{max} flips the first, followed by units with higher vertex angles as seen in Fig.4.9c. From Fig.4.3, we see that ϕ^* is higher for higher α values, which indicates that the unit with a high vertex angle has an antiparallel shape which has a compact shape or lower frontal area. Thus, post-snapping the unit with the highest vertex angle has the least drag force on it. Also, we see that the drag coefficient for all the units before snapping is identical and almost remains constant (Fig.4.9d). The coefficient for the unit with $\alpha = 65°$ post snapping remains almost constant, this can be attributed to the fact that its antiparallel state has $\phi > 90°$, thus the upper facets of the unit are shadowed by the lower facets. Whereas in the other units, a part of the upper facets still sees the flow. The unit with angle 35° is monostable and the snapping in this unit does not lead to any significant drag change as we do not see discontinuity in this drag curve.

Lastly, we vary L_2 while keeping the other parameters to $\theta = 50°$ and $\alpha = 45°$. As increasing L_2 increases the normal area to the flow thus in the pre-snapping phase the unit with maximum L_2 has a faster increase in drag forces as depicted in Fig.4.9e (darker blue curve has higher drag force). As observed in the potential energy curve (Fig.4.6c) the maximum torque of the unit

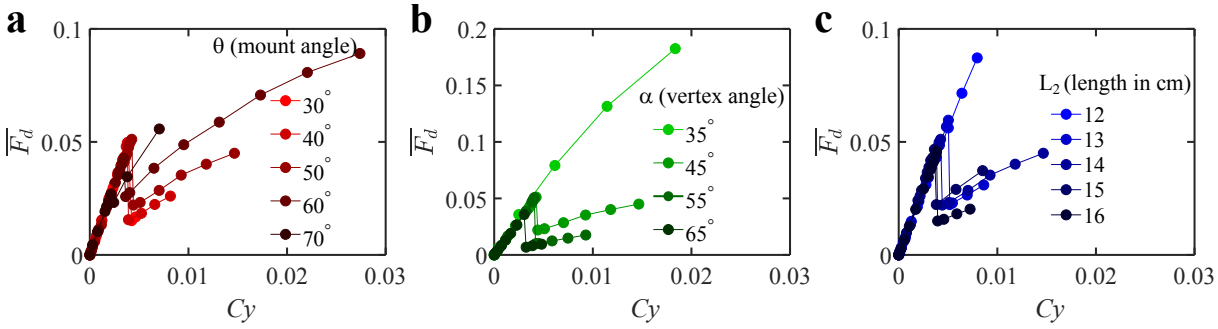

Figure 4.10: Non-dimensional plot using the non-dimensional drag force and the Cauchy number for the unit with different (**a**) mounting angle θ, (**b**) vertex angle ϕ and (**c**) length of the upper facet L_2. The units with $\theta = 50°$, $\alpha = 45°$ and $L_2 = 14$ are common in all the graphs.

decreases till $L_2 = 15$ cm and increases again. A similar flipping trend for the units is also observed in the drag forces curve (Fig.4.9). Post snapping only the lower facet of the units are exposed to the flow, with a part of the upper facet seen by the flow as the unit doesn't snap beyond 90°. Interestingly, the drag coefficient for the units is similar post snapping (Fig.4.9f), this indicates that the balance between the weight and the elastic forces leads to a similar normal area in all the units to have similar drag forces. The drag curve also indicates that by changing the length of the upper facet, we can tune the flipping point and the drag jump while following the same drag force curve post-snapping.

We demonstrate how three parameters of the unit modify the features of the drag curve. As the dynamics of the unit are governed by the balance of the fluid and elastic forces we can define the Cauchy number $C_y = \rho U^2 w^2 L_2 \sin^2(\theta)/\kappa$ similar to the previous chapters. Similarly, we define a nondimensional drag force $\bar{F_d} = F_d w \sin(\theta)/\kappa$, where κ is the effective stiffness of the pseudo joint found using the linear region of the torque displacement curve (see Fig.4.11b). The curve for different mounting angle θ and vertex angle α shows a good rescaling pre-snapping and at the snapping point (Fig.4.10a,b), indicative of the fact that the Cauchy number defined can capture the influence of these two parameters. The length of the upper facet is well rescaled in the opening part, but the flipping point did not rescale, thus we need to modify the Cauchy number to account for the change in L_2. This is also related to our lack of understanding of the influence of L_2 on the torque and effective stiffness of the unit.

4.4 Theoretical Model

We see that the unit when mounted at an angle θ in parallel configuration acts as a rigid object before snapping to the anti-parallel shape as can be seen in the normalized projected area (Fig.4.7c). The maximum torque experienced by the unit is within $\phi = 5°$ for most of the cases as seen in mechanical test sections (Fig.4.6). This is indicative of the fact that the unit can be treated as a rigid object before snapping. The energy approach will not be applicable in this case as the unit needs to deform for us to calculate the work done by the fluid forces. Thus we will apply moment balance by assuming that as the torque applied by the fluid force overcomes the maximum torque from the mechanical test, the unit will snap to the anti-parallel configuration.

Based on these observations we developed a simplified theoretical model by balancing the torque on the unit due to fluid loading with the maximum torque observed in the mechanical test, which allows us to obtain the critical flow speed for snapping. Let us calculate the torque applied by the fluid forces on the upper facet made up of length L_2 and L_c, the length of the crease, which can be expressed as $L_c = W/\sin\alpha$. We assume the unit to be mounted at angle

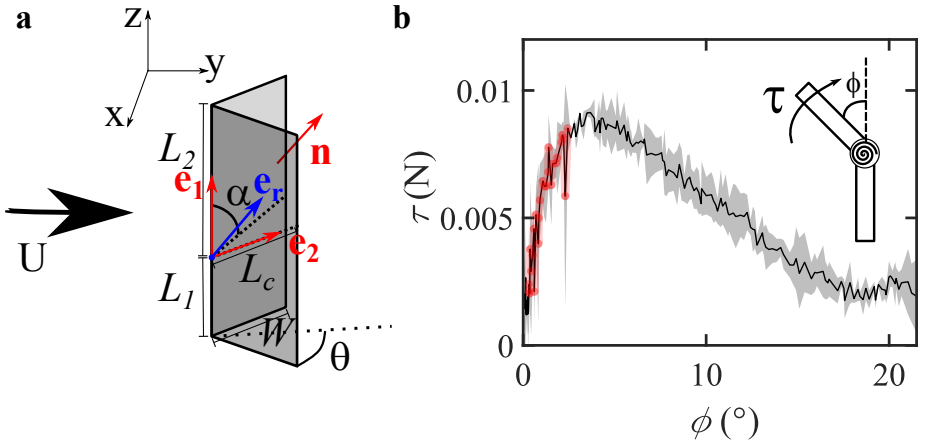

Figure 4.11: (**a**) Geometry of the mounted Miura ori unit in the flow with the convex side facing the flow with various unit vectors and geometrical parameters of the unit used for calculation. The flow is in the positive y direction. (**b**) The torque-angle curve for one of the units depicting the initial linear growth region coloured red was used to calculate the stiffness of the unit for the non-dimensional plot.

θ (Fig.4.11a). This leads to the unit vectors along the spinal crease and the peripheral crease being given by $\vec{e_1}$ and $\vec{e_2}$ respectively. A general vector on the upper facet is then given as a linear combination of these two unit vectors i.e. $\vec{r} = l_1\vec{e_1} + l_2\vec{e_2}$. And a unit normal vector to the surface is defined as $\hat{n} = \frac{\vec{e_1}\times\vec{e_2}}{||\vec{e_1}\times\vec{e_2}||}$. The flow is assumed to be in the positive x direction. A small area element in the form of a parallelogram is considered at a point whose position vector is $\vec{r}$. The torque applied by the fluid forces on this element assuming fluid pressure of the form $P = \rho(\vec{U}.\vec{n})^2$ is given by:

$$d\tau = \vec{r} \times d\vec{F} = \vec{r} \times \hat{n}\rho U^2(\hat{n}.\vec{e_y})^2 dl_1 dl_2 \sin\alpha \tag{4.4}$$

The cross-product is given by:

$$\vec{r} \times \hat{n} = (l_1\vec{e_1} + l_2\vec{e_2}) \times \frac{\vec{e_1}\times\vec{e_2}}{||\vec{e_1}\times\vec{e_2}||} \tag{4.5}$$

Using the vector identity: $\vec{a}\times(\vec{b}\times\vec{c}) = (\vec{a}.\vec{c})\vec{b} - (\vec{a}.\vec{b})\vec{c}$ and the angle between the two vectors α the cross product reduces to:

$$\vec{r} \times \hat{n} = \frac{l_1(\cos\alpha\vec{e_1} - \vec{e_2}) + l_2(\vec{e_1} - \cos\alpha\vec{e_2})}{\sin\alpha} \tag{4.6}$$

The net torque on the upper facet can be calculated by integrating the torque on this area element over the whole surface:

$$\tau_{Facet1} = \int_0^{L_1}\int_0^{L_2} \rho U^2 \frac{\sin^2\theta}{\sin\alpha}(l_1(\cos\alpha\vec{e_1} - \vec{e_2}) + l_2(\vec{e_1} - \cos\alpha\vec{e_2}))\sin(\alpha) dl_1 dl_2 \tag{4.7}$$

As a result, we obtain:

$$\tau_{Facet1} = \rho U^2 \frac{\sin^2\theta}{2} L_2 L_c[(L_2\cos\alpha + L_c)\vec{e_1} - (L_2 + L_c\cos\alpha)\vec{e_2}) \tag{4.8}$$

Similar to this we can define a third unit vector ($\vec{e_3}$) along the other peripheral crease and by following the same method we obtain the torque experienced by the other upper facet as:

$$\tau_{Facet2} = \rho U^2 \frac{\sin^2\theta}{2} L_c L_c[(L_2 + L_c\cos\alpha)\vec{e_3} - (L_2\cos\alpha + L_c)\vec{e_1}]$$

Which gives the total torque on the upper facets as:

$$\tau_{total} = \rho U^2 \frac{\sin^2\theta}{2} L_2 L_c[(L_2 + L_c\cos\alpha)(\vec{e_3} - \vec{e_2})] \tag{4.9}$$

From the geometry of the unit and the axis as described in the figure, the vectors are given by: $\vec{e_2} = (\sin\alpha\sin\theta, \sin\alpha\cos\theta, \cos\alpha)$ and $\vec{e_3} = (\sin\alpha\sin\theta, -\sin\alpha\cos\theta, \cos\alpha)$ Thus the net torque can be re-written as:

$$\tau_{total} = -\rho U^2 \sin^2\theta L_2 L_c[(L_2 + L_c\cos\alpha)]\sin\alpha\sin\theta\vec{e_x} \tag{4.10}$$

Where $\vec{e_x}, \vec{e_y}$ and $\vec{e_z}$ are unit vectors in the corresponding directions.

Thus the final equation to obtain the critical flow velocity of flipping becomes:

$$\tau_{max} = \sin\alpha\sin\theta\rho U^2 \sin^2\theta L_2 L_c[(L_2 + L_c\cos\alpha)]\vec{e_x} \tag{4.11}$$

Solving this non-linear equation for U, for the given values of θ and α using corresponding τ_{max} from the mechanical test gives us the critical flow speed. The experimental values are plotted against the predicted values from the model for critical snapping velocity U_c in Fig.4.12b. The points lie on a linear curve indicating that the trend is clearly reproduced for different values of mount angle and the vertex angles. Thus we can say that the simplified model which assumes the balance between the fluid torque and the maximum elastic torque works well and the assumption of the unit being rigid pre-snapping is valid. To see what affects the drag jump in all our measurements, we can plot the ratio of the drag coefficients $C_d/C_{d,0}$ with the non-dimensional speed U/U_c (Fig.4.12). The graph indicates that increasing the post-snapping angle (ϕ^*) between the spinal creases is proportional to the ratio of the drag coefficients.

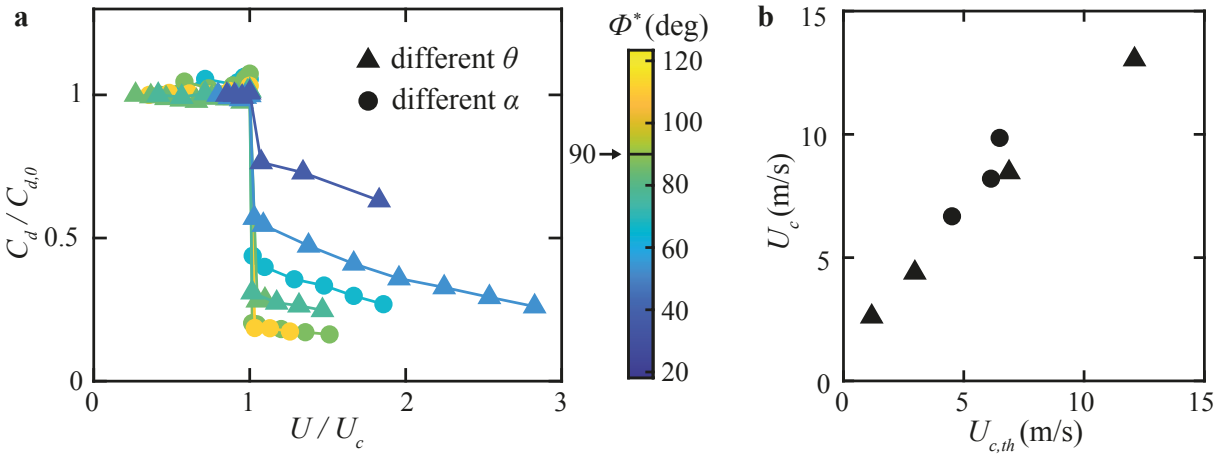

Figure 4.12: (**a**) Evolution of drag coefficient ratio ($C_d/C_{d,0}$) for the units with different opening angles (θ) and vertex angles (α) indicating the decrease in the value with increasing post snapping angles ϕ^*. (**b**) Comparison of the critical speed for snapping with the values obtained by the model for the units with different α and θ.

4.5 Conclusion

In this chapter, we demonstrated that the four-vertex origami unit transitions from one rigid configuration to another through a hidden degree of freedom, which arises from facet bending. This facet bending leads to a drag discontinuity. This behaviour contrasts with the previous chapter, where the folding pathway was governed by the system's degree of freedom, allowing for continuous deformation before and after the snap-through event. Mechanical characterization of

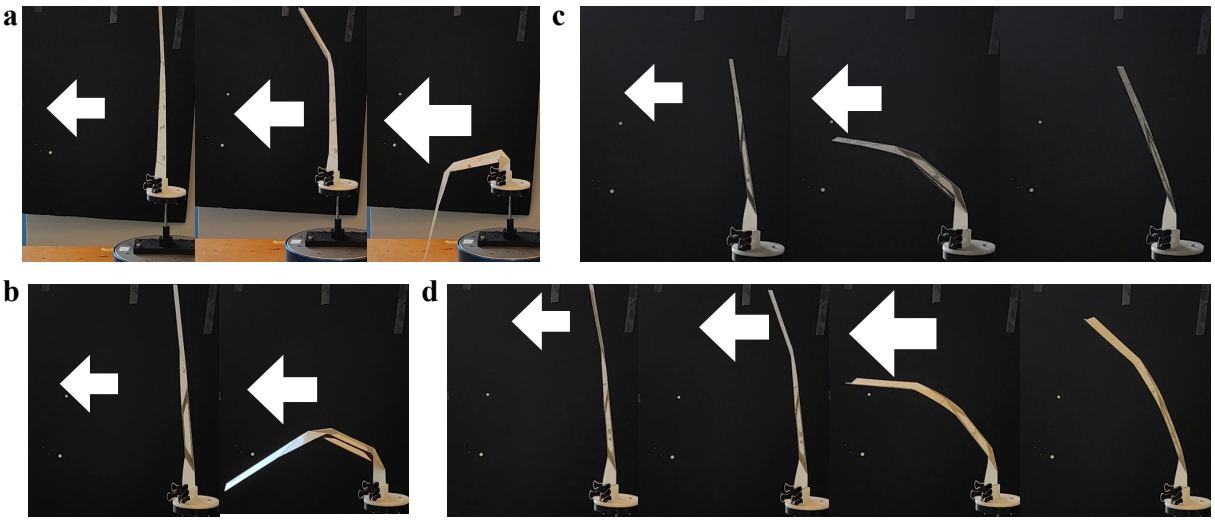

Figure 4.13: Different possible configurations for a string made with three vertices. (**a**) The upper part of the string flips first followed by the lower part with increasing flow speed. The lower vertex angle is 65° and the upper 45°. (**b**) The lower part of the unit flips first leading to flipping of the whole string. Both the vertex angles are 45°. All the creases had stiffness of $\kappa = 19 \times 10^{-3}$N. (**c**) The string with all the monostable creases of stiffness $\kappa = 93 \times 10^{-3}$N and vertex angles 45° depicting the folding pattern and reverting back of the unit after the flow is turned off. (**d**) The string with the upper creases of $\kappa = 19 \times 10^{-3}$N and lower creases of stiffness $\kappa = 93 \times 10^{-3}$N and vertex angles 45° showing the flipping of the top part followed by the folding of the lower part and the unit returning to the intermediate position when the flow is turned off. The mount angle in all the cases is $\theta = 50°$.

the unit reveals that its effective stiffness is primarily due to the bending of the lower facet. By varying the unit's geometrical parameters (θ, ϕ, and L_2), we can fine-tune the maximum torque required for the transition. The mounting angle and vertex angle have a monotonic influence on the maximum torque, which increases with a decreasing mounting angle and an increasing vertex angle. In contrast, the length of the upper facet shows non-monotonic behaviour, with the minimum torque occurring at $L_2 = 15$ cm. Changing the geometry and mounting angle of the unit allows us to control the mechanical properties, which influences the drag experienced by the system. Experiments conducted in an air flow while varying these parameters elucidate the influence of geometrical changes on the unit's drag characteristics. Introducing the Cauchy number, which balances fluid and elastic forces, indicates a need to rescale for mounting angle and vertex angle, though modifications are necessary to account for the upper facet length. A simple model, based on the observed rigid behaviour before snapping and the balance between torque from fluid loading and the maximum torque required for the unit to flip, qualitatively agrees with experimental data for the critical velocity for snapping in flow conditions. The future direction to develop a solid mechanics simulation [68] and a refined shell model will improve upon our current understanding of the observed dynamics.

The study can be extended to multiple units, also referred to as strings, allowing for larger shape changes and more configuration possibilities[129]. By tuning the parameters and flow speed, we can observe various configurations as depicted in Fig.4.13. If we use only the bistable unit, then there are two possibilities, the upper part of the string flips first followed by the lower part (Fig.4.13a) or the lower part flips first (Fig.4.13b). Introducing a monostable unit by changing the crease stiffness can give rise to similar possibilities with the possibility for the unit to invert back to one of the intermediate states in the absence of the flow (Fig.4.13c and d).

This study highlights the potential of origami structures to achieve multiple rigid shapes

under different flow conditions. This shape change can be used to have different functionalities for instance the two shapes can be used as an antenna which operates at different resonance frequencies [130]. It can also serve as a memory unit, which will store the information about the past flow conditions[99]. Similar to the previous chapter, these transitions can serve as protective mechanisms, with the added benefit of returning to the initial position when the load is removed. This research opens up possibilities for developing tunable, load-bearing, and resilient structures that can self-actuate in omnipresent airflow[131].

Chapter 5

Conclusion and future prospects

Contents

5.1 Conclusion

In this thesis, we studied the non-conventional fluid-structure interaction problem. The technique of origami gives interesting folding kinematics and mechanical properties, which were leveraged to influence drag vs speed behaviour. Specifically, we use bistability which arises from the geometry of the structure and via facet bending to have drag discontinuity with different pre and post-snapping behaviour.

In the **first chapter**, we explore how the bistability of the Waterbomb base can be leveraged to significantly reduce drag force as flow velocity increases. When subjected to uniform airflow, the origami unit unfolds, and upon reaching a flat configuration, it undergoes a snap-through to a more streamlined shape, leading to a sudden drop in drag. This approach uniquely achieves drag reduction through abrupt and substantial shape changes in response to a small increase in fluid input load. Notably, this snap-through behaviour can be tuned by adjusting the cell radius, fold stiffness, and rest angle, allowing for precise control over drag characteristics. Our analysis shows that the cell's behaviour results from a quasi-static mechanical equilibrium between the fluid-induced load and the restoring elastic forces, which is characterized by a Cauchy number. The snap-through occurs at a critical Cauchy number specific to a given cell rest angle, which also serves as an additional control factor, influencing both the onset of snap-through and the resulting changes in drag. A theoretical fluid-elastic model captures these experimental observations, representing the cell as rigid facets with elastic hinges at the folds and using an empirical formulation for fluid pressure forces. The modelling framework establishes the system equations needed for inverse design, enabling the identification of structural parameter combinations that result in a desired drag reduction. Our implementation demonstrates advanced control capabilities, allowing for selective adjustment of key drag features, including the peak drag before snapping, the magnitude of the drag reduction, and the critical flow speed at which it occurs.

In the **second chapter**, we explored the application of the Waterbomb unit in confined flow as a valve. A wind tunnel with a circular cross-section was developed and characterized, followed by the mounting of the unit at the centre of the pipe. The passive adaption of the unit with the flow gives rise to a non-linear pressure drop across the unit as the flow speed is increased. Similar to the drag the pressure drop across the unit initially rises at a faster rate with increasing blockage, followed by snap-through to give pressure discontinuity and further increase in speed leads to a slow increase in pressure as the blockage is reduced. By altering various physical and geometrical parameters, we were able to adjust the flipping point and pressure drop. Additionally, the effect of confinement is taken into account by introducing an effective flow velocity which takes into account the blockage effect. By modifying the Cauchy number using effective flow velocity and defining non-dimensional pressure, we observed a rescaling of the plot, except in cases where the blockage was too high (units with larger R). Adapting the model used in the first chapter to include local flow speed allowed us to accurately predict the pressure drop across the unit. We also examined experimentally two units in series, achieving multiple peaks in the pressure curve. Drawing on the analogy between the fluidic and electronic systems, we developed a toy model to explore combinations of units. Firstly we studied two units in series, followed by multiple units. The toy model was able to capture the behaviour of two units and demonstrated that placing multiple units in series can maintain constant pressure across the system for a specific flow range. The toy model was then applied to a more experimentally challenging scenario with two units in parallel. With the model, we observe that a pipe with an obstruction equipped with an origami unit in parallel can work as a flow rate limiter. When the pressure drop because of obstruction increases beyond a critical value or when the flow across it reaches a critical value, the unit in parallel can snap to short circuit the branch with a sudden jump in velocity. By adjusting the unit's parameters, it is possible to fine-tune the pressure threshold. The switch-like response of the Waterbomb base could enable fluidic control in channels, acting as a relief valve to limit pressure buildup by discharging fluid beyond a predetermined pressure level. The unit may function as a semipermeable membrane to promote directed flow, as shown by Brandenbourger et al[104, 120]. Flexible membranes were used to get semipermiability, by blocking the channel in one direction and opening it in another direction. The future potential lies in reverse engineering the units to achieve specific pressure curves or combining multiple units to create unique pressure versus flow characteristics, as demonstrated by Park et al.[108]. Combining multiple valves with non-monotonic pressure vs flow behaviour in series and parallel allowed them to obtain triangular, square or other interesting pressure vs flow curves. Furthermore, the sudden flow change in one chamber during parallel flow could trigger rapid actuation of an attached component, as suggested by Qiao et al [132].

In the **third chapter**, we demonstrated that the Miura ori unit transitions between rigid configurations through a hidden degree of freedom caused by facet bending, resulting in a drag discontinuity. This behaviour contrasts with the previous chapter, where the folding pathway allowed for continuous deformation before and after the snap-through event. Mechanical characterization reveals that the unit's effective stiffness mainly stems from the bending of the lower facet. By adjusting the unit's geometrical parameters—such as the mounting angle θ, the vertex angle α, and the length of the upper facet l_2—we can fine-tune both the stiffness and the maximum torque required for the transition. These adjustments control the mechanical properties as well as the drag experienced by the system. Airflow experiments varying these parameters clarify how geometrical changes affect the unit's drag characteristics. Introducing the Cauchy number, which balances fluid and elastic forces, rescales the drag data for mounting angle and vertex angles, though modifications are required to incorporate the effect of the upper facet length. A simple model based on the rigid behaviour before snapping and the balance between torque from fluid loading and the maximum torque needed for the unit to flip aligns qualitatively with experimental data shown by comparing the critical velocity for snapping. The study

also explored multiple units, or strings, enabling larger shape changes and more configuration possibilities. The use of mono-stability and bi-stability, along with various connection methods, offers numerous possibilities.

This thesis presents a promising proof of concept, demonstrating the potential of origami structures for programming drag versus speed behaviour. This capability is valuable for self-protection strategies, such as mitigating excessive aerodynamic loads beyond a set threshold or serving as a velocity threshold detector. The snap-through behaviour of the Waterbomb base, which involves passing through an unstable flat state, results in an initial drag increase, beneficial for stabilization or speed reduction in applications like sea anchors, drogues, or aerial refuelling stabilizers [16, 18]. This shape-adaptive drag offers better control and stabilization in varying fluid environments. In spite of having a structure which deforms continuously to pass through the flat state resulting in an initial increase in drag, we can also have a structure which has two rigid states like a mounted Miura ori unit. This can be done via hidden degrees of freedom, such as facet bending [81], which could enable significant shape changes while maintaining minimal deformation and a relatively constant drag coefficient before snap-through.

Morphing driven by aeroelastic forces allows components to autonomously respond to the local environment, eliminating the need for additional sensing and control systems and enabling more streamlined aerodynamic control surfaces. However, the main limitation of these bistable systems is the requirement of an external intervention or counter-flow to revert to their original state. This limitation can be useful as well for example as a memory units that store information about past fluid conditions[99]. Alternatively, monostable systems that snap through under load but return to their original state when the load is removed could address this limitation [41, 47, 48]. Another advantage of origami is the ease of combining multiple bistable elements to create multistable structures [74, 97–99]. For instance, a chain of two Waterbomb cells or Miura ori string can produce successive sharp transitions in drag force, with each unit having its independent flow velocity threshold for snap-through. Other configurations might lead to interactions between cells through external flow, resulting in more complex collective responses, as seen in fluidic cellular origami [97]. Shared facets between cells could enable communication of mechanical states between units, forming logic elements [100], and generating more complex snapping sequences and drag evolution with flow speed for advanced adaptive functionalities.

Some of the other possibilities that we have explored but not in very much detail are presented below. These are some of the ideas that we have tested and can be the future direction for studies of origami structures in an airflow.

5.2 Future Prospects

Flow visualization

In our model, we used a very simplified representation of fluid mechanics. It does not take into account the retroaction of the object on the flow, we assume that the flow velocity seen by the origami is that of undisturbed flow. We also did not include the effect of the wake region. These limitations in our model may be the primary cause of the differences observed in the experimental and theoretical models. A better understanding of the flow pattern around and behind the origami unit will help in improving the model to incorporate these effects. This will provide a better agreement between the experimental and theoretical curves, which will help in better inverse design. These flow patterns can be observed with the help of flow visualization or numerical simulation.

Fig.5.1, depicts the flow pattern around and behind the Waterbomb unit mounted in a water channel of cross-section 20×20cm operated at a maximum flow speed of 3cm/s. These are some of the preliminary results and do not correspond to the actual flow regime i.e., they are at a

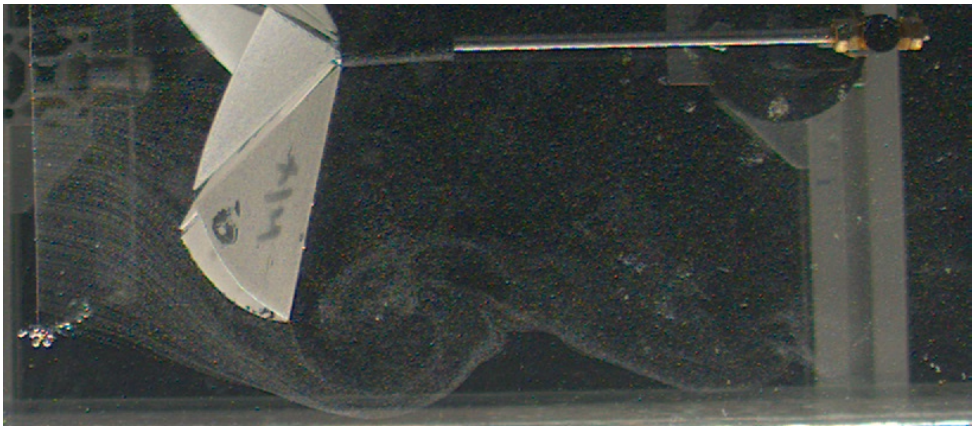

Figure 5.1: Flow visualization for the unit mounted in a water channel with the concave side facing the flow using hydrogen bubbles.

lower Re, though they still give information on the flow patterns. For the visualisation, we use a wire to generate hydrogen bubbles. The picture taken with the high-speed camera while illuminating the region with LED lights clearly shows the vortex shed at the edges (Fig.5.1). A more detailed experimental investigation is required to get further insight into the flow around the unit. This investigation will be very useful in the case of several units combined in series, or units downstream or upstream of an obstacle, where the flow perturbations generated by one would influence the behaviour of the other. We observe that the snapping velocity for the unit placed downstream of an obstacle can be changed by changing the distance between the two. We also observe that the drag force on the two units placed in series (similar to the pipe flow example) is not the sum of individual units and changes with the distance between them. These observations are likely the influence of the interactions between the objects through flow. Thus, a better understanding of the flow pattern will help in investigating these observations to a deeper level.

5.2.1 Multiple jumps

In the conclusion section of the first chapter, we saw the combination of two Waterbomb units can lead to multiple jumps. Those units were combined with the help of a rigid panel. To have units with functionality or to have the desired folding pathway, the units need to be combined in such a way that their kinematics are compatible which is not easy to achieve. An alternative to this is to use facet bending. We show a method to achieve multiple jumps by adding a Miura ori unit with a Waterbomb unit at its centre (Fig.5.2a). Starting from the concave side facing the flow, the Miura facets start flipping one by one at different flow rates, which leads to asymmetric folding of the unit. As a consequence of this, we saw three drag discontinuities in the same unit. These jumps can be tuned by changing the unit's parameters and the preliminary test shows one such possibility.

Another method that leads to multiple jumps is making inverted origami or a shell structure, where facet bending is easier than crease bending (Fig.5.2b). This unit is fabricated using a thinner sheet of mylar with a thicker sheet at its creases and a large mounting angle. So, the unit can deform only via facet bending and the creases are assumed to be very stiff. In the airflow when mounted with a concave side facing the flow, a small asymmetry in the fabrication leads to the upper half bending (similar to buckling of the beam) before the lower half as a consequence we see a sudden reduction in drag force. On further increasing the flow the lower part of the unit also bends leading to another drag drop. Though the examples presented here are not

experimentally very robust they highlight interesting consequences of including facet bending in the system. Further investigation is required to make these methods robust to achieve multiple drag jumps in the flow.

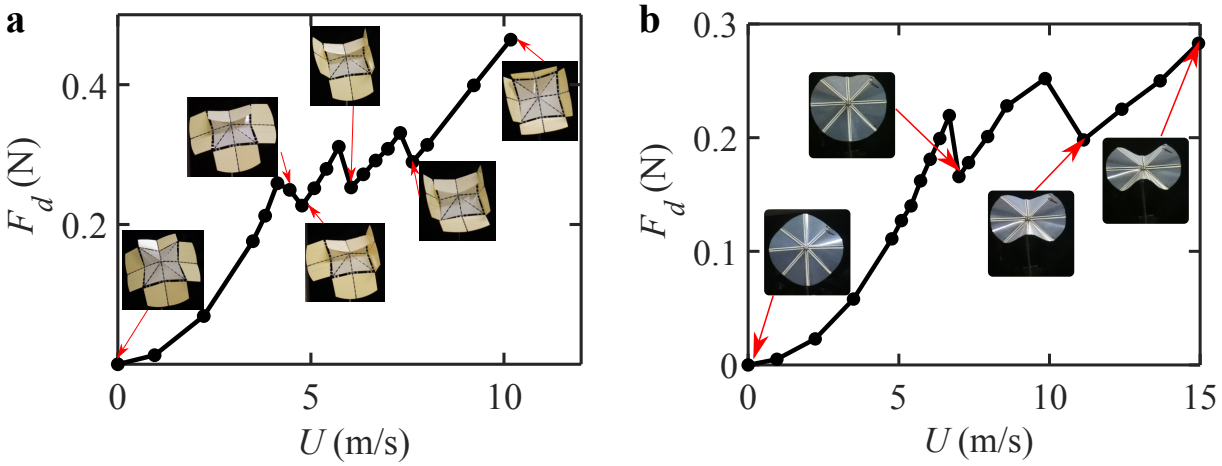

Figure 5.2: Multiple drag discontinuity achieved by (**a**) combining Waterbomb unit with Miura ori unit and by (**b**) Waterbomb unit with rigid creases and flexible facets.

5.2.2 Different crease stiffness

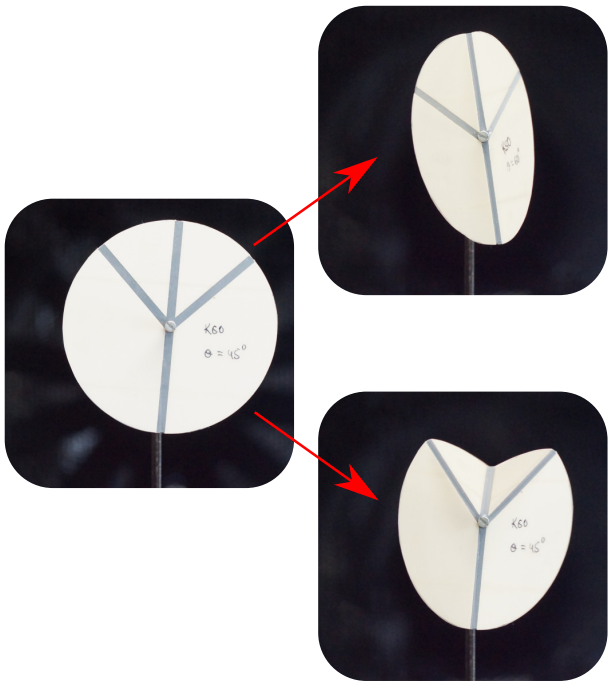

Figure 5.3: Different folding pathways a flat Miura ori unit made with disk can take. The parallel configuration (O1), where the spinal creases fold in the same directions (both mountains) and the antiparallel configuration (O2) with spinal creases folding in opposite directions (mountain and valley).

In Chapter 3 we talked about the Miura ori unit in great detail and looked at the two possible folding pathways that the unit can take (parallel and anti-parallel). In this exploration,

we looked at the influence of the crease stiffness on the folding behaviour of the unit. Starting from a flat state, the unit with all creases of the same stiffness can spontaneously go to either parallel configuration (O1) or antiparallel configuration(O2) (shown in Fig.5.3) for all the sector angles. We observe that the unit can go to O1 in the first test and then O2 in the second test, the choice of the orientation is random. If we increase the stiffness of the lower spinal crease, we observe that the unit always chooses the O2 pathway. Thus modifying crease stiffness can be a good strategy to choose a folding pathway. Another possibility to decide the folding pathway is to give an initial angle to the unit and start by mounting it with the concave side facing the flow. It was observed that this unit when exposed to an airflow always goes to the O1 folding pathway. Thus imposing an initial angle can also act as a strategy to select the folding pathway. This unit can be made to go to another folding pathway if in spite of using the steady flow with increased speed, we use a gust of air. The unit when suddenly exposed to the high-velocity gust goes to O2. This indicates the possibility of studying origami units in unsteady flow to achieve other interesting behaviours.

5.2.3 Non-flat foldable unit

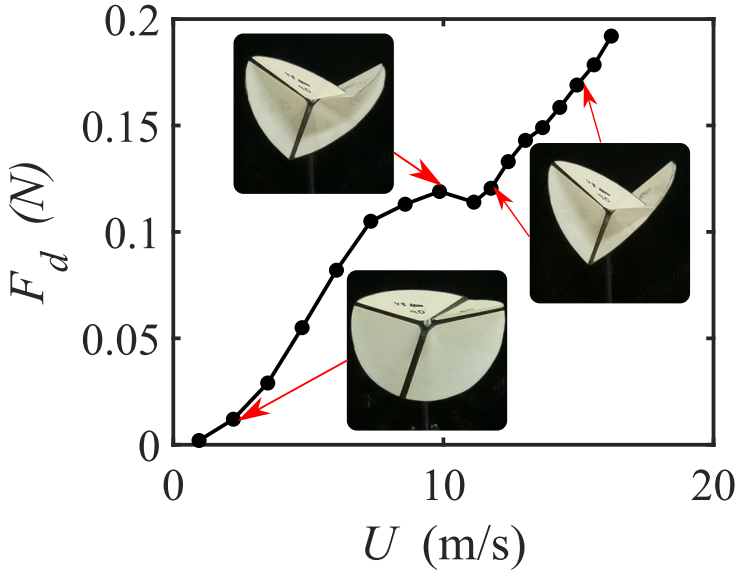

Figure 5.4: Drag force curve for non-flat foldable vertex four-unit with sector angles $(90°, 90°, 120°, 60°)$. The drag increases at a slow rate during the closing process and increases faster post-locking. Figures are added to demonstrate the shapes at different data points.

All the structures we studied so far were flat foldable i.e., they are the structures that can be folded into a plane or they become 2 dimensional when fully folded. The structures that are not flat foldable usually end up with facets getting stuck with each other as a consequence they show a sudden rise in stiffness also their final folded shape is a 3D structure. Fig.5.4 shows one of the simplest non-flat foldable structures called non-generic degree four vertex unit. It is made up of sectors angles $(90°, 90°, 120°, 60°)$. The drag curve for the unit starting from a convex shape indicates that in the initial part when the unit deforms, leads to a lower increase in drag similar to reconfigurable slender/origami structures, as the facets come into contact, the unit gets stuck in that shape and becomes rigid. Increasing the flow speed post-blocking leads to a faster increase in drag. Changing the last two angles while keeping the first two fixed can be used to tune the drag curve, by changing the shape of the blocked unit. This shows another interesting drag feature enabled by origami other than the drag jump, which is a discontinuity in the rate of increase of drag with the flow due to the sudden stiffening of the unit.

5.2.4 Flow induced expansion of Miura ori tube

One of the following questions that comes to mind after studying a single unit is what happens when we have multiple units. This is investigated by a Miura ori tube. A single Miura ori unit fabricated with some rest angle other than 180° in the antiparallel configuration when mounted with a concave side facing the flow tends to open up towards a flat state(similar to the Water-bomb unit). Whereas when the same unit is mounted with a convex side facing the flow tends to close. In both cases, the unit is pinned at the centre. Now what will happen when we merge multiple such units? If the first vertex is pointing against the flow(convex shape), then the next one will be pointing towards the flow and similarly, the following vertex will alternatively follow the same pattern. This gives us a sheet in which alternating vertices tend to open and close respectively. So, will the sheet open in flow or close? As a sheet will be able to bend in the flow as well, we decided to make a tube which reduces the amount of bending[61] and reduces the motion to only the expansion and contraction (1 degree of freedom). The aim was to study how fluid forces at the individual level(units here), can affect the global deployment of a bigger structure. The novelty of this exploration is the expansion normal to the flow as we will discuss. All the experiments and modelling discussed below were done by Abhyuday Pandey, whom I co-supervised during his third-year bachelor thesis.

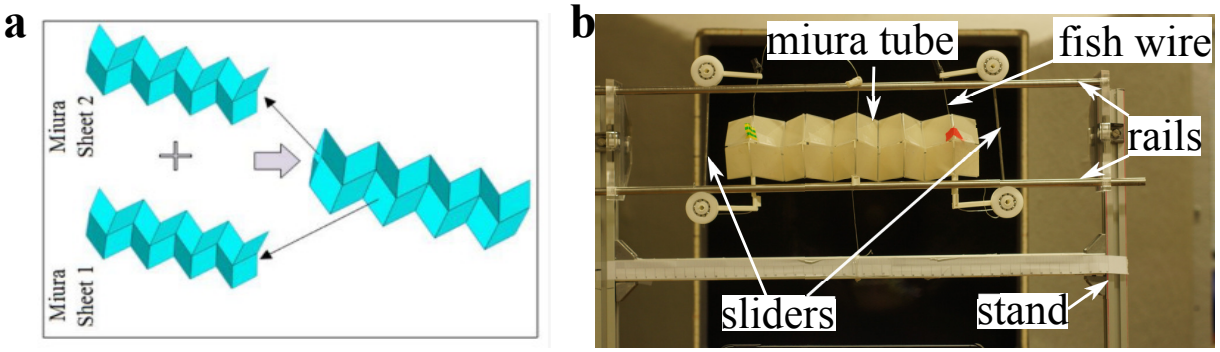

Figure 5.5: (**a**) Fabrication process of the Miura ori tube. Individual units were combined via creases to form a string or sheet (a string with 4 units is shown in the left), which were then stacked in inverted configurations to make a tube. (**b**) Experimental setup with Miura ori tube mounted with the help of sliders on the rail to be able to expand in response to flow coming out of a plane with the least amount of friction.

The tube is fabricated using the same fabrication technique used before with the Miura strings merged with scotch tape and a small hole is made through each vertex to avoid stress concentration and to help with the mounting. The final unit and merging process is depicted in Fig.5.5a. A mount that allows the unit to expand and contract freely while avoiding out-of-plane motion was fabricated (Fig.5.5b).

The tube was mounted using rails in its rest length in the wind tunnel and flow was increased from $0 - 13$ m/s. The ends of the tube were free whereas the center was pinned. The length of the tube is extracted with the help of pictures taken by a camera downstream. Fig.5.6a, shows the expansion of the tube in response to the increasing flow with the flow direction out of the plane. The extracted length of the tube is depicted in Fig.5.6b. Tests were conducted on tubes with different crease stiffness and vertex angles. By changing these parameters we could control the amount and rate of expansion with increasing flow rates.

A fluid-structure model following the energy approach used in Chapter 1 was developed for the Miura tube. The facets were assumed to be perfectly rigid, and all folds act as torsion springs (with identical stiffness per unit length) with a linear response. Another vital assumption is that

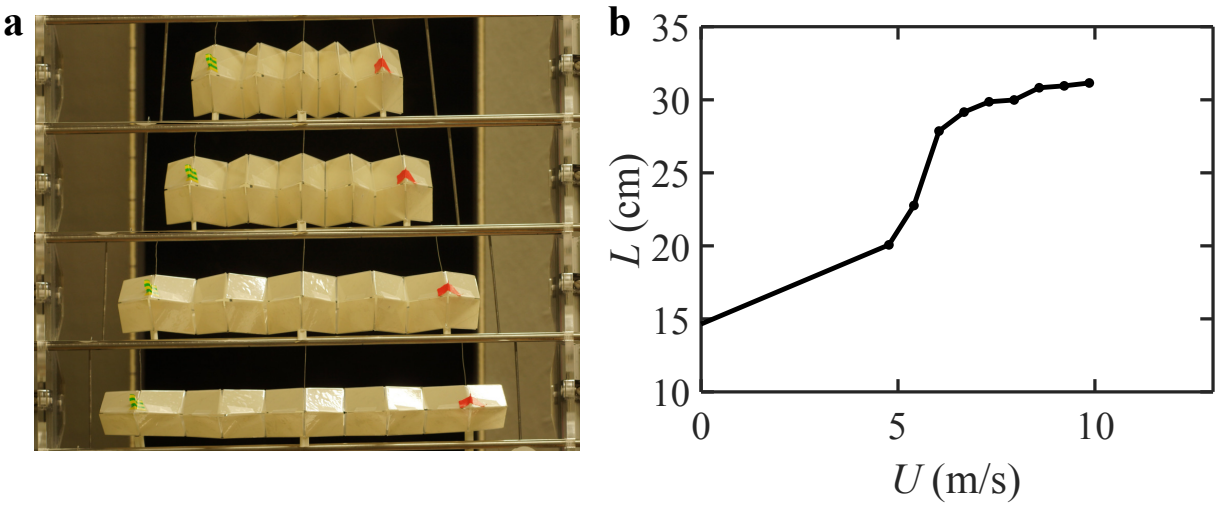

Figure 5.6: (**a**) Expansion of Miura ori tube in a flow with increasing flow speed using the pictures taken from a camera downstream and the (**b**) expansion measured as a function of speed. The unit has a vertex angle of 55° and crease stiffness 2.5×10^{-3}N.

the presence of adjacent units does not affect how the flow interacts with and moves around the tube and the tube extends uniformly, such that the work done on the whole tube can be extrapolated from the work done on a single unit.

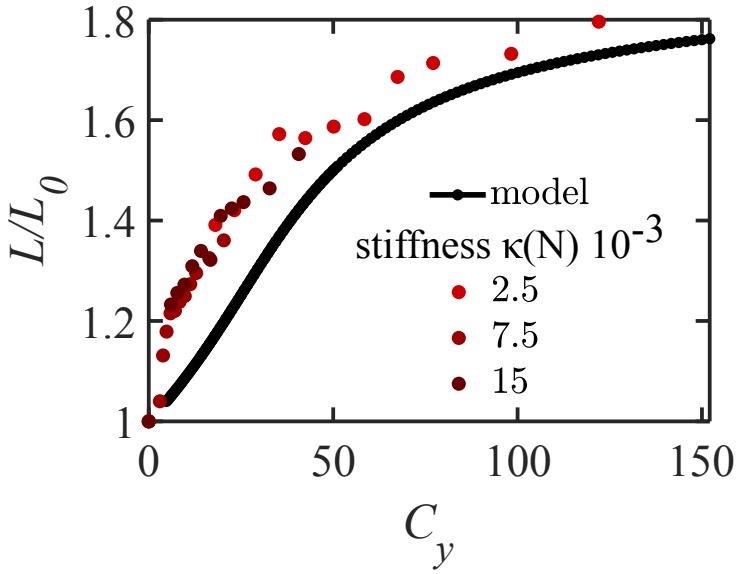

Figure 5.7: Non-dimensional length L/L_0 as a function of non-dimensional Cauchy number for units with different crease stiffness. Experimental curves are depicted in red and the theoretical curve is in black.

The balance between the potential energy and the work done by the fluid forces gives rise to the following equation:

$$\frac{n\rho u^2 L_1 L_2}{\kappa|\sin^3\alpha|}\cos^2\psi\sin^2\beta\left(L_1^2\frac{d\psi}{d\beta}\sin\beta+L_2^2\cos\psi\right)=(4n-2)L_1(\theta-\theta_0)\frac{d\theta}{d\beta}+2nL_2(\phi-\phi_0)\frac{d\phi}{d\beta}, \tag{5.1}$$

Where L_1 and L_2 are the length of the spinal and peripheral creases, θ and ϕ are angle of mountain and valley folds, n is number of units, is stiffness per unit length of the creases, α is the vertex angle of the unit, ψ is the angle between the peripheral facet and β is the angle used

to define the motion of the unit. The equation is solved numerically to get the expansion of the tube at increasing flow rates.

Similar to the previous studies we define the Cauchy number as $C_y = \frac{C_d \rho u^2 L_1^2}{\kappa}$ to account for the effect of the creases stiffness. The collapse of the data (Fig.5.7 red dots) on a curve indicates that the Cauchy number can take into account the balance between the fluid and elastic forces for the system. The model can predict a similar expansion of the tube with a slight underestimation.

The preliminary results of this study provide good support for the intuitive understanding of the behaviour of the tube. The model developed does not perfectly predict the extension of a tube with given physical parameters at a given wind speed, but it is close enough to be useful. The tubes did not return to their initial position when the flow was removed, indicating that the friction forces on the rails were not negligible. This can be improved by making stiffer tubes and we can incorporate the friction in the model. This study can be extended to other versions of the Muira-Ori like the zipper tube, the aligned tube, and the internally coupled tubes [61].

In the thesis and the investigations presented here, we looked at the various origami units and the usefulness of their mechanical properties to achieve different drag features. Which were shown to be tunable using the various geometrical and mechanical properties of the units. We hope that the study was able to illuminate the benefits and interesting behaviour of origami structures in a flow and will ignite curiosity in the field of origami-based fluid-structure interactions.

Thank you for reading this manuscript. This is all from my side. I bid you farewell. Au revoir!

Bibliography

1. Mohsen, J. *Aircraft drag reduction: an overview* tech. rep. (Research report 2011: 02, ISSN 1652-8549, Division of Dynamics Department of ..., 2013).
2. Blocken, B., Toparlar, Y., van Druenen, T. & Andrianne, T. Aerodynamic drag in cycling team time trials. *Journal of Wind Engineering and Industrial Aerodynamics* **182,** 128–145 (2018).
3. Li, L., Wu, J., Liang, Y. & Tian, Z. Numerical Investigations of Outer-Layer Turbulent Boundary Layer Control for Drag Reduction Through Micro Fluidic-Jet Actuators. *Aerospace Research Communications* **2,** 12506 (2024).
4. Jiang, Y. *et al.* Aerodynamic drag analysis and reduction strategy for satellites in Very Low Earth Orbit. *Aerospace Science and Technology* **132,** 108077 (2023).
5. Nath, D. S., Pujari, P. C., Jain, A. & Rastogi, V. Drag reduction by application of aerodynamic devices in a race car. *Advances in Aerodynamics* **3,** 1–20 (2021).
6. Kumar, S., Verma, K. A., Pandey, K. M. & Sharma, K. K. A review on methods used to reduce drag of the ship hulls to improve hydrodynamic characteristics. *International Journal of Hydromechatronics* **3,** 297–312 (2020).
7. Sairam, E. L. & Kumar, A. *Hydrodynamic Analysis of Submarine Profiles for Drag Reduction* in *Recent Advances in Applied Mathematics and Applications to the Dynamics of Fluid Flows: 5th International Conference on Applications of Fluid Dynamics (ICAFD) 2020* (2022), 381–388.
8. Crouch, T. N., Burton, D., LaBry, Z. A. & Blair, K. B. Riding against the wind: a review of competition cycling aerodynamics. *Sports Engineering* **20,** 81–110 (2017).
9. Mehta, R. C. Aerodynamics of sport balls, badminton shuttlecock and javelin. *Scholars Journal of Engineering and Technology* **11,** 4–10 (2023).
10. Choi, J., Jeon, W.-P. & Choi, H. Mechanism of drag reduction by dimples on a sphere. *Physics of Fluids* **18** (2006).
11. Huang, B., Sun, Y. & Zeng, Q. Real-time drogue detection and template tracking strategy for autonomous aerial refueling. *Journal of Real-Time Image Processing* **17,** 437–446 (2020).
12. Greathouse, J. & Schwing, A. *Study of geometric porosity on static stability and drag using computational fluid dynamics for rigid parachute shapes* in *23rd AIAA Aerodynamic Decelerator Systems Technology Conference* (2015), 2131.
13. Cortesi, M., Di Michele, R. & Gatta, G. Effects of intracyclic velocity variations on the drag exerted by different swimming parachutes. *The Journal of Strength & Conditioning Research* **33,** 531–537 (2019).
14. Kurec, K., Remer, M. & Piechna, J. The influence of different aerodynamic setups on enhancing a sports car's braking. *International Journal of Mechanical Sciences* **164,** 105140 (2019).

15. McLachlan, B. G. *An Experimental Study of Airfoil-Spoiler Aerodynamics* PhD thesis (Stanford University, 1983).
16. Wei, Z.-B., Dai, X., Quan, Q. & Cai, K.-Y. Drogue dynamic model under bow wave in probe-and-drogue refueling. *IEEE Transactions on Aerospace and Electronic Systems* **52,** 1728–1742 (2016).
17. Raj, C. A. S. *et al.* Aerodynamics of ducted re-entry vehicles. *Chinese Journal of Aeronautics* **33,** 1837–1849 (2020).
18. Holler, R. *Hydrodynamic drag of drogues and sea anchors for drift control of freefloating buoys* in *OCEANS'85-Ocean Engineering and the Environment* (1985), 1330–1335.
19. Piechna, J. A review of active aerodynamic systems for road vehicles. *Energies* **14,** 7887 (2021).
20. Jenett, B. *et al.* Digital morphing wing: active wing shaping concept using composite lattice-based cellular structures. *Soft robotics* **4,** 33–48 (2017).
21. Norman, A., Kerrigan, E. & McKeon, B. The effect of small-amplitude time-dependent changes to the surface morphology of a sphere. *Journal of fluid mechanics* **675,** 268–296 (2011).
22. Guttag, M., Yan, D. & Reis, P. M. Programmable Aerodynamic Drag on Active Dimpled Cylinders. *Advanced Engineering Materials* **21,** 1801315 (2019).
23. Cramer, N. B. *et al.* Elastic shape morphing of ultralight structures by programmable assembly. *Smart Materials and Structures* **28,** 055006 (2019).
24. Shao, C.-P., Chen, Y.-J. & Lin, J.-Z. Wind induced deformation and vibration of a Platanus acerifolia leaf. *Acta Mechanica Sinica* **28,** 583–594 (2012).
25. Vollsinger, S., Mitchell, S. J., Byrne, K. E., Novak, M. D. & Rudnicki, M. Wind tunnel measurements of crown streamlining and drag relationships for several hardwood species. *Canadian Journal of Forest Research* **35,** 1238–1249 (2005).
26. Vogel, S. Drag and flexibility in sessile organisms. *Am. Zool.* **24,** 37–44 (1984).
27. Vogel, S. Drag and reconfiguration of broad leaves in high winds. *Journal of Experimental Botany* **40,** 941–948 (1989).
28. Vogel, S. When leaves save the tree. *Natural History* **102,** 58–63 (1993).
29. Harder, D. L., Speck, O., Hurd, C. L. & Speck, T. Reconfiguration as a prerequisite for survival in highly unstable flow-dominated habitats. *Journal of Plant Growth Regulation* **23,** 98–107 (2004).
30. Gosselin, F., de Langre, E. & Machado-Almeida, B. A. Drag reduction of flexible plates by reconfiguration. *J. Fluid Mech.* **650,** 319 (2010).
31. Schouveiler, L. & Boudaoud, A. The rolling up of sheets in a steady flow. *J. Fluid Mech.* **563,** 71 (2006).
32. Schouveiler, L. & Eloy, C. Flow-induced draping. *Phys. Rev. Lett.* **111,** 064301 (2013).
33. Alben, S., Shelley, M. & Zhang, J. Drag reduction through self-similar bending of a flexible body. *Nature* **420,** 479–481 (2002).
34. Alben, S., Shelley, M. & Zhang, J. How flexibility induces streamlining in a two-dimensional flow. *Physics of Fluids* **16,** 1694–1713 (2004).
35. Gosselin, F. *Mécanismes d'interactions fluide-structure entre écoulements et végétation* PhD thesis (Ecole Polytechnique (Palaiseau, France), 2009).
36. Morel, T. Aerodynamic drag of bluff body shapes characteristic of hatch-back cars. *SAE Transactions,* 1270–1279 (1978).

37. Lopez, D., Michelin, S. & De Langre, E. Flow-induced pruning of branched systems and brittle reconfiguration. *Journal of Theoretical Biology* **284,** 117–124 (2011).

38. Wieselsberger, C. v. Neuere Feststellungen under die Gesetze des Flussigkeits und Luftwiderstandes. *Phys. Z.* **22,** 321–328 (1921).

39. Achenbach, E. Experiments on the flow past spheres at very high Reynolds numbers. *J. Fluid Mech.* **54,** 565–575 (1972).

40. Lopez, D., Eloy, C., Michelin, S. & De Langre, E. Drag reduction, from bending to pruning. *Europhys. Lett.* **108,** 48002 (2014).

41. Gomez, M., Moulton, D. E. & Vella, D. Passive control of viscous flow via elastic snap-through. *Phys. Rev. Lett.* **119,** 144502 (2017).

42. Cavens, W. D. K., Chopra, A. & Arrieta, A. F. Passive load alleviation on wind turbine blades from aeroelastically driven selectively compliant morphing. *Wind Energy* **24,** 24–38 (2021).

43. Han, J. S., Ko, J. S. & Korvink, J. G. Structural optimization of a large-displacement electromagnetic Lorentz force microactuator for optical switching applications. *J. Micromech. Microeng.* **14,** 1585 (2004).

44. Tavakol, B. *et al.* Buckling of dielectric elastomeric plates for soft, electrically active microfluidic pumps. *Soft matter* **10,** 4789–4794 (2014).

45. Overvelde, J. T. B., Kloek, T., D'haen, J. J. A. & Bertoldi, K. Amplifying the response of soft actuators by harnessing snap-through instabilities. *Proc. Natl. Acad. Sci. U.S.A* **112,** 10863–10868 (2015).

46. Shan, S. *et al.* Multistable architected materials for trapping elastic strain energy. *Adv. Mater.* **27,** 4296–4301 (2015).

47. Arena, G. *et al.* Adaptive compliant structures for flow regulation. *Proc. R. Soc. A* **473,** 20170334 (2017).

48. Arena, G., Groh, R. M. J., Theunissen, R., Weaver, P. M. & Pirrera, A. Design and testing of a passively adaptive inlet. *Smart Mater. Struct.* **27,** 085019 (2018).

49. Peretz, O., Mishra, A. K., Shepherd, R. F. & Gat, A. D. Underactuated fluidic control of a continuous multistable membrane. *Proc. Natl. Acad. Sci.* **117,** 5217–5221 (2020).

50. Kim, H., Zhou, Q., Kim, D. & Oh, I.-K. Flow-induced snap-through triboelectric nanogenerator. *Nano Energy* **68,** 104379 (2020).

51. Kim, H., Lahooti, M., Kim, J. & Kim, D. Flow-induced periodic snap-through dynamics. *J. Fluid Mech.* **913,** A52 (2021).

52. Arrieta, A. F., Bilgen, O., Friswell, M. I. & Hagedorn, P. Passive load alleviation bi-stable morphing concept. *AIP Adv.* **2** (2012).

53. Lang, R. J. *Origami design secrets: mathematical methods for an ancient art* (CRC Press, 2012).

54. Dudte, L. H., Vouga, E., Tachi, T. & Mahadevan, L. Programming curvature using origami tessellations. *Nature materials* **15,** 583–588 (2016).

55. Mitani, J. A design method for 3D origami based on rotational sweep. *Computer-Aided Design and Applications* **6,** 69–79 (2009).

56. Demaine, E. D., Demaine, M. L., Hart, V., Price, G. N. & Tachi, T. (Non) existence of pleated folds: how paper folds between creases. *Graphs and Combinatorics* **27,** 377–397 (2011).

57. Callens, S. J. & Zadpoor, A. A. From flat sheets to curved geometries: Origami and kirigami approaches. *Materials Today* **21,** 241–264 (2018).

58. Schenk, M. & Guest, S. D. Geometry of Miura-folded metamaterials. *Proceedings of the National Academy of Sciences* **110,** 3276–3281 (2013).

59. Seffen, K. A. Compliant shell mechanisms. *Philosophical Transactions of the Royal Society A: Mathematical, Physical and Engineering Sciences* **370,** 2010–2026 (2012).

60. Schenk, M., Guest, S. D., *et al.* Origami folding: A structural engineering approach. *Origami* **5,** 291–304 (2011).

61. Filipov, E. T., Tachi, T. & Paulino, G. H. Origami tubes assembled into stiff, yet reconfigurable structures and metamaterials. *Proceedings of the National Academy of Sciences* **112,** 12321–12326 (2015).

62. Zirbel, S. A. *et al.* Accommodating thickness in origami-based deployable arrays. *Journal of mechanical design* **135,** 111005 (2013).

63. Kuribayashi, K. *et al.* Self-deployable origami stent grafts as a biomedical application of Ni-rich TiNi shape memory alloy foil. *Materials Science and Engineering: A* **419,** 131–137 (2006).

64. Li, S., Fang, H., Sadeghi, S., Bhovad, P. & Wang, K.-W. Architected origami materials: How folding creates sophisticated mechanical properties. *Adv. Mater.* **31,** 1805282 (2019).

65. Li, S., Fang, H. & Wang, K. Recoverable and programmable collapse from folding pressurized origami cellular solids. *Physical review letters* **117,** 114301 (2016).

66. Waitukaitis, S., Menaut, R., Chen, B. G. & Van Hecke, M. Origami multistability: From single vertices to metasheets. *Phys. Rev. Lett.* **114,** 055503 (2015).

67. Meloni, M. *et al.* Engineering origami: A comprehensive review of recent applications, design methods, and tools. *Advanced Science* **8,** 2000636 (2021).

68. Zhu, Y., Schenk, M. & Filipov, E. T. A review on origami simulations: From kinematics, to mechanics, toward multiphysics. *Applied Mechanics Reviews* **74,** 030801 (2022).

69. Fang, H., Chu, S.-C. A., Xia, Y. & Wang, K.-W. Programmable self-locking origami mechanical metamaterials. *Advanced Materials* **30,** 1706311 (2018).

70. Melancon, D., Gorissen, B., Garcıa-Mora, C. J., Hoberman, C. & Bertoldi, K. Multistable inflatable origami structures at the metre scale. *Nature* **592,** 545–550 (2021).

71. Addis, C. C., Rojas, S. & Arrieta, A. F. Connecting the branches of multistable non-Euclidean origami by crease stretching. *Physical Review E* **108,** 055001 (2023).

72. Wei, Z. Y., Guo, Z. V., Dudte, L., Liang, H. Y. & Mahadevan, L. Geometric mechanics of periodic pleated origami. *Physical review letters* **110,** 215501 (2013).

73. Silverberg, J. L. *et al.* Origami structures with a critical transition to bistability arising from hidden degrees of freedom. *Nature materials* **14,** 389–393 (2015).

74. Silverberg, J. L. *et al.* Using origami design principles to fold reprogrammable mechanical metamaterials. *science* **345,** 647–650 (2014).

75. Liu, B. *et al.* Topological kinematics of origami metamaterials. *Nature Physics* **14,** 811–815 (2018).

76. Sun, Y. *et al.* Origami-inspired folding assembly of dielectric elastomers for programmable soft robots. *Microsystems & Nanoengineering* **8,** 37 (2022).

77. Novelino, L. S., Ze, Q., Wu, S., Paulino, G. H. & Zhao, R. Untethered control of functional origami microrobots with distributed actuation. *Proceedings of the National Academy of Sciences* **117,** 24096–24101 (2020).

78. Yoon, C. *et al.* Functional stimuli responsive hydrogel devices by self-folding. *Smart Materials and Structures* **23,** 094008 (2014).

79. Kotikian, A. *et al.* Untethered soft robotic matter with passive control of shape morphing and propulsion. *Science robotics* **4,** eaax7044 (2019).

80. Chen, B. *et al.* Soft origami gripper with variable effective length. *Advanced Intelligent Systems* **3,** 2000251 (2021).

81. Liu, C. & Felton, S. M. Transformation dynamics in origami. *Physical review letters* **121,** 254101 (2018).

82. Liu, C., Aung, Z. M. H. & Felton, S. M. *Dynamic transformation of an origami string using a stacked-Miura cell* in *International Design Engineering Technical Conferences and Computers and Information in Engineering Conference* **59247** (2019), V05BT07A031.

83. Zhang, J., Li, T., Wang, C. & Yan, X. Aerodynamic drag characteristics of miura-ori composite structure. *Journal of Aerospace Engineering* **34,** 06021004 (2021).

84. Cozmei, M. *et al.* Aerogami: Composite origami structures as active aerodynamic control. *Composites Part B: Engineering* **184,** 107719 (2020).

85. Tolman, K., Crampton, E. B., Stucki, C., Maynes, R. & Howell, L. L. *Design of an origami-inspired deployable aerodynamic locomotive fairing* in *Proceedings of the 7th International Meeting on Origami in Science, Mathematics and Education* (2018).

86. Yang, Z., Chen, D., Levine, D. J. & Sung, C. Origami-inspired robot that swims via jet propulsion. *IEEE Robotics and Automation Letters* **6,** 7145–7152 (2021).

87. Chen, G., Chen, D., Weakly, J. & Sung, C. *Drag Coefficient Characterization of the Origami Magic Ball* in *International Design Engineering Technical Conferences and Computers and Information in Engineering Conference* **87363** (2023), V008T08A055.

88. Marzin, T., de Langre, E. & Ramananarivo, S. Shape reconfiguration through origami folding sets an upper limit on drag. *Proc. R. Soc. A* **478,** 20220592 (2022).

89. Hanna, B. H., Lund, J. M., Lang, R. J., Magleby, S. P. & Howell, L. L. Waterbomb base: a symmetric single-vertex bistable origami mechanism. *Smart Mater. Struct.* **23,** 094009 (2014).

90. Lechenault, F., Thiria, B. & Adda-Bedia, M. Mechanical response of a creased sheet. *Phys. Rev. Lett.* **112,** 244301 (2014).

91. Zhang, J., Changguo, W. & Zhang, L. Deployment of SMP Miura-ori sheet and its application: Aerodynamic drag and RCS reduction. *Chinese J. Aeronaut.* **35,** 121–131 (2022).

92. Hanna, B. H., Magleby, S. P., Lang, R. J. & Howell, L. L. Force–deflection modeling for generalized origami waterbomb-base mechanisms. *J. Appl. Mech.* **82** (2015).

93. Brunck, V., Lechenault, F., Reid, A. & Adda-Bedia, M. Elastic theory of origami-based metamaterials. *Phys. Rev. E* **93,** 033005 (2016).

94. Overvelde, J. T. B. *et al.* A three-dimensional actuated origami-inspired transformable metamaterial with multiple degrees of freedom. *Nat. Commun.* **7,** 1–8 (2016).

95. Zuliani, F., Liu, C., Paik, J. & Felton, S. M. Minimally actuated transformation of origami machines. *IEEE Robot. Autom. Lett.* **3,** 1426–1433 (2018).

96. De Langre, E., Gutierrez, A. & Cossé, J. On the scaling of drag reduction by reconfiguration in plants. *C.R. Mécanique* **340,** 35–40 (2012).

97. Li, S. & Wang, K. W. Fluidic origami with embedded pressure dependent multi-stability: a plant inspired innovation. *J. R. Soc. Interface* **12,** 20150639 (2015).

98. Sengupta, S. & Li, S. Harnessing the anisotropic multistability of stacked-origami mechanical metamaterials for effective modulus programming. *J. Intell. Mater. Syst. Struct.* **29,** 2933–2945 (2018).

99. Jules, T., Reid, A., Daniels, K. E., Mungan, M. & Lechenault, F. Delicate memory structure of origami switches. *Phys. Rev. Res.* **4,** 013128 (2022).

100. Treml, B., Gillman, A., Buskohl, P. & Vaia, R. Origami mechanologic. *Proc. Natl. Acad. Sci. U.S.A.* **115,** 6916–6921 (2018).

101. Oh, K. W. & Ahn, C. H. A review of microvalves. *Journal of micromechanics and microengineering* **16,** R13 (2006).

102. Van Laake, L. C., de Vries, J., Kani, S. M. & Overvelde, J. T. A fluidic relaxation oscillator for reprogrammable sequential actuation in soft robots. *Matter* **5,** 2898–2917 (2022).

103. Pontin, M. & Damian, D. D. Multimodal soft valve enables physical responsiveness for preemptive resilience of soft robots. *Science Robotics* **9,** eadk9978 (2024).

104. Brandenbourger, M., Dangremont, A., Sprik, R. & Coulais, C. Tunable flow asymmetry and flow rectification with bio-inspired soft leaflets. *Physical Review Fluids* **5,** 084102 (2020).

105. Park, K. *et al.* Viscous flow in a soft valve. *Journal of Fluid Mechanics* **836,** R3 (2018).

106. Christensen, A. H. & Jensen, K. H. Viscous flow in a slit between two elastic plates. *Physical Review Fluids* **5,** 044101 (2020).

107. Louf, J.-F., Knoblauch, J. & Jensen, K. H. Bending and stretching of soft pores enable passive control of fluid flows. *Physical review letters* **125,** 098101 (2020).

108. Park, K. *et al.* Fluid-structure interactions enable passive flow control in real and biomimetic plants. *Physical Review Fluids* **6,** 123102 (2021).

109. Preston, D. J. *et al.* A soft ring oscillator. *Science Robotics* **4,** eaaw5496 (2019).

110. Decker, C. J. *et al.* Programmable soft valves for digital and analog control. *Proceedings of the National Academy of Sciences* **119,** e2205922119 (2022).

111. Napp, N., Araki, B., Tolley, M. T., Nagpal, R. & Wood, R. J. *Simple passive valves for addressable pneumatic actuation* in *2014 IEEE International Conference on Robotics and Automation (ICRA)* (2014), 1440–1445.

112. Wehner, M. *et al.* An integrated design and fabrication strategy for entirely soft, autonomous robots. *nature* **536,** 451–455 (2016).

113. Di Lallo, A. *et al. A novel approach to under-actuated control of fluidic systems* in *2018 IEEE International Conference on Robotics and Automation (ICRA)* (2018), 193–199.

114. Xu, S., Chen, Y., Hyun, N.-s. P., Becker, K. P. & Wood, R. J. A dynamic electrically driven soft valve for control of soft hydraulic actuators. *Proceedings of the National Academy of Sciences* **118,** e2103198118 (2021).

115. De Chant, L. J. The venerable 1/7th power law turbulent velocity profile: a classical nonlinear boundary value problem solution and its relationship to stochastic processes. *Applied Mathematics and Computation* **161,** 463–474 (2005).

116. Idelchik, I. E., Steinberg, M. & Martynenko, O. G. *Handbook of hydraulic resistance* (Hemisphere publishing corporation New York, 1986).

117. Benedict, R. Loss coefficients for fluid meters (1977).

118. Gulsacan, B., Tokgoz, N., Karakas, E. S., Aureli, M. & Evrensel, C. A. Effect of orifice thickness-to-diameter ratio on turbulent orifice flow: An experimental and numerical investigation. *International Communications in Heat and Mass Transfer* **151,** 107213 (2024).

119. Liu, Y., Liu, J. & Gao, F.-P. Strouhal number for boundary shear flow past a circular cylinder in the subcritical flow regime. *Ocean Engineering* **269,** 113574 (2023).

120. Ledesma-Alonso, R., Guzmán, J. & Zenit, R. Experimental study of a model valve with flexible leaflets in a pulsatile flow. *Journal of Fluid Mechanics* **739,** 338–362 (2014).

121. Walker, M. Mechanics of generically creased disks. *Physical Review E* **101,** 043001 (2020).

122. Lechenault, F. & Adda-Bedia, M. Generic bistability in creased conical surfaces. *Physical review letters* **115,** 235501 (2015).

123. Iniguez-Rabago, A. & Overvelde, J. T. From rigid to amorphous folding behavior in origami-inspired metamaterials with bistable hinges. *Extreme Mechanics Letters* **56,** 101881 (2022).

124. Sareh, P. & Guest, S. D. Design of isomorphic symmetric descendants of the Miura-ori. *Smart Materials and Structures* **24,** 085001 (2015).

125. Faber, J. A., Arrieta, A. F. & Studart, A. R. Bioinspired spring origami. *Science* **359,** 1386–1391 (2018).

126. Liu, C., Wohlever, S. J., Ou, M. B., Padir, T. & Felton, S. M. Shake and take: Fast transformation of an origami gripper. *IEEE Transactions on Robotics* **38,** 491–506 (2021).

127. Kamrava, S., Mousanezhad, D., Ebrahimi, H., Ghosh, R. & Vaziri, A. Origami-based cellular metamaterial with auxetic, bistable, and self-locking properties. *Scientific reports* **7,** 46046 (2017).

128. Foschi, R., Hull, T. C. & Ku, J. S. Explicit kinematic equations for degree-4 rigid origami vertices, Euclidean and non-Euclidean. *Physical Review E* **106,** 055001 (2022).

129. Kamrava, S., Mousanezhad, D., Felton, S. M. & Vaziri, A. Programmable origami strings. *Advanced Materials Technologies* **3,** 1700276 (2018).

130. Molaei, A., Liu, C., Felton, S. M. & Martinez-Lorenzo, J. Origami inspired reconfigurable antenna for wireless communication systems. *arXiv preprint arXiv:1805.10370* (2018).

131. Rivas-Padilla, J. R., Boston, D. M., Boddapati, K. & Arrieta, A. F. Aero-structural optimization and actuation analysis of a morphing wing section with embedded selectively stiff bistable elements. *Journal of Composite Materials* **57,** 737–757 (2023).

132. Qiao, C., Liu, L. & Pasini, D. Bi-shell valve for fast actuation of soft pneumatic actuators via shell snapping interaction. *Advanced Science* **8,** 2100445 (2021).

ECOLE DOCTORALE

Titre : L'origami comme plateforme pour ajuster la force de traînée

Mots clés : Elasticité, Interaction fluide/structure, Origami/Kirigami

Résumé : La force de traînée augmente généralement avec la vitesse de l'écoulement, sauf dans certains cas spécifiques comme la crise de traînée ou des changements brusques de forme, comme lorsqu'un vent violent brise les branches d'un arbre. Dans ce cas, la traînée exercée sur l'arbre chute instantanément, lui permettant de maintenir son intégrité structurelle malgré l'irréversibilité du phénomène. Une alternative intéressante pour créer des changements brusques de forme est le phénomène de "snap-through" dans les structures flexibles. La technique de l'origami offre un cadre prometteur pour concevoir de telles structures, capables de passer d'un état d'équilibre à un autre. En intégrant des plis spécifiques, il est possible de contrôler la cinématique et les propriétés mécaniques des structures, notamment leur multistabilité. Dans cette thèse, nous avons étudié des cellules d'origami bistables capables de passer à un second état stable, soit en suivant leur trajectoire cinématique, soit par un degré de liberté « caché » résultant de la flexion des faces. Ces cellules peuvent se déformer continuellement dans un écoulement avant de passer à leur nouvel état, ou maintenir leur forme avant et après la transition. Ces deux comportements entraînent une variation discontinue de la traînée avec l'augmentation de la vitesse d'écoulement. En ajustant les propriétés géométriques et mécaniques, il est possible de modifier la vitesse critique de retournement et la force de traînée subie par l'élément. Les résultats expérimentaux ont été validées par un modèle théorique aéroélastique basé sur l'équilibre les forces fluides et élastiques. Ce travail met en avant l'origami comme une méthode prometteuse pour créer des structures passives déployables capables de contrôler la traînée dans des environnements fluides. Par exemple, nous avons démontré expérimentalement qu'une structure en origami peut fonctionner comme une valve passive pour réguler le débit.

Title : Origami as a platform for tuning drag force

Keywords : Elasticity, Fluid/structure interaction, Origami/Kirigami

Abstract : The drag force typically rises with flow speed, except in cases like drag crisis or abrupt shape changes, such as wind-induced tree pruning. While pruning reduces drag sharply and maintains structural integrity, it is irreversible. An attractive alternative for abrupt shape change is snap-through events in flexible structures. Origami provides a promising framework for crafting such shape-morphing structures. By prescribing specific folds, one can achieve the desired kinematic pathway and mechanical properties, particularly multistability. In this thesis, we studied bistable origami units capable of transitioning to a second stable state either by following the kinematic path or by utilizing a hidden degree of freedom arising from facet bending. These units can either deform continuously in flow with a snap-through event or maintain their shape before and after snapping to the second state. Both behaviours show a discontinuous evolution of drag with increasing flow speed. By adjusting geometrical and mechanical properties, we can modify and fine-tune the snapping event and the drag force experienced by the unit. Experiments were corroborated by a theoretical aero-elastic model that balances fluid forces with elastic forces. This work presents an origami design strategy for creating efficient passive deployable structures capable of controlling drag in fluid environments. For instance, we demonstrated an origami structure functioning as a passive valve to regulate flow.

Institut Polytechnique de Paris
91120 Palaiseau, France